Dark Matter Halos: Assembly, Clustering and Sub-halo Accretion

DARK MATTER HALOS: ASSEMBLY, CLUSTERING AND SUB-HALO ACCRETION

A Dissertation Presented

by

YUN LI

Submitted to the Graduate School of the
University of Massachusetts Amherst in partial fulfillment
of the requirements for the degree of

DOCTOR OF PHILOSOPHY

February 2010

Astronomy

DARK MATTER HALOS: ASSEMBLY, CLUSTERING AND SUB-HALO ACCRETION

A Dissertation Presented

by

YUN LI

Approved as to style and content by:

Houjun Mo, Chair

Martin D. Weinberg, Member

Todd M. Tripp, Member

John F. Donoghue, Member

Stephen Schneider, Department Chair
Astronomy

To my beloved family.

ACKNOWLEDGMENTS

I would like to express my sincere gratitude to my advisor, Professor Houjun Mo. Without his support and encouragement I could never have finished this work. Professor Mo has supervised me since 2004 and given me numerous advices to help me clarify my ideas to develop this dissertation. I have benefited tremendously from his wide range of knowledge and creative thinking.

I am also indebted to my family, my father Zong-Long Zhou and mother Yao-Li Li, who have constantly lent me their whole-hearted support since the day I entered the Astronomy Department of UMass. Their warm words have been a major motivation for me to finish this program.

My wife, Bo-Ning, has been accompanying me during the past four years here at UMass. Her unwavering patience, love and encouragement have upheld me, particularly during the days when I was struggling with my research. Her support is in the end what made this dissertation possible.

I enjoyed and learned a lot from the vivid discussions with Professors Martin Weinberg, Neal Katz in this department, Professors Frank van den Bosch, Liang Gao and Postdoctoral fellow Zheng Zheng from outside this department. Professors John Kwan and William Irvine, as the former and current graduate program directors, have generously spent time helping me make a smooth and steady progress in my graduate studies. Yu Lu, Hui Dong, Zhiyuan Li, Yuxi Chen, Guilin Liu, Shuikui Tang and Limin Song, all have provided me with helpful arguments and suggestions in astrophysical theory and I would like to thank them too. I really enjoyed sharing a cheerful time with all my fellow students during the past several years in this department.

I also would like to thank the whole department and its generous financial support. Miss Terri Grzybowski and Miss Denise Parent have always been working hard to help students, including myself, maintain a good graduate standing.

ABSTRACT

DARK MATTER HALOS: ASSEMBLY, CLUSTERING AND SUB-HALO ACCRETION

FEBRUARY 2010

YUN LI

B.Sc., NANJING UNIVERSITY

M.Sc., NATIONAL ASTRONOMICAL OBSERVATORY, CHINESE ACADEMY OF SCIENCES

Ph.D., UNIVERSITY OF MASSACHUSETTS AMHERST

Directed by: Professor Houjun Mo

I carried out systematic studies on the assembly history of dark matter halos, using numerical simulations and semi-analytical methods.

First, I look into dark halo mass assembly history. I confirmed that the halo mass assembly is divided into a fast accretion phase and a slow accretion phase. These two phases are found to be separated by the epoch when the dark halo potential reaches its maximum. The fast accretion phase is dominated by mergers, especially major mergers; the slow accretion phase is dominated by slow mass accretion. Each halo experiences about 3 ± 2 major mergers since its main progenitor had a mass equal to 1 percent of halo mass. However, the average redshift at which these major mergers occur is strongly mass dependent.

Secondly, I investigate the formation times and the assembly bias of dark halos. I use eight different definitions of halo formation times to characterize the different

aspects of the halo assembly history. I find that these formation times have different dependence on halo mass. While some formation times characterize well the hierarchical nature of halo formation, the trend is reversed for other definitions of the formation time. In addition, the formation-time dependence of halo bias is quite strong for some definitions of formation time but weak or absent for others.

Thirdly, I study sub-halo mass function in the halo assembly history, with the generally known *unevolved* sub-halo mass functions (USMFs). I find that for sub-halos that merge into the main progenitor of a present-day halo, their USMF can be well described by a universal functional form; the same conclusion can also be reached for the USMF of all sub-halos that have merged during the entire halo merging history. In these two cases, the USMFs do not seem to depend on the redshift of the host halo either. However, due to the mass loss caused by dynamical effects, only small part of the accreted halos survived and became sub-structures in the present-day dark halos. In the cluster-sized halos, 30% survived sub-halos are sub-subhalos. The sub-halo mass function at given accretion time (redshift) is also investigated to find the origin of the statistics mentioned above.

TABLE OF CONTENTS

LIST OF TABLES

Table **Page**

LIST OF FIGURES

Figure **Page**

CHAPTER 1

A BRIEF REVIEW OF THE PROPERTIES OF DARK MATTER HALOS

1.1 Cosmological background

In the current cosmological models, the mass in the universe is believed to be made up of collisionless dark matter, which only interacts through gravitational force. The formation of the large-scale structure is therefore a consequence of the growth of the gravitational instability in the initial cosmic density field. The well-relaxed compact objects developed from the initial density field are known as the dark matter halos. A large part of modern cosmology concentrates on the studies of these objects, because of their dominant role in the gravitational field in the universe where luminous objects such as galaxies form and evolve. At the current stage, Cold Dark Matter (CDM) scheme has been widely adopted and serves successfully as the framework for modeling the galaxy formation.

1.1.1 The cosmological model

Modern cosmology is based on the Cosmological Principle and the General Relativity. Cosmological principle is a hypothesis that says on large scales the universe is homogeneous and isotropic. General relativity is the theoretical ground that describes the evolution of the large-scale spacetime.

Based on the Cosmological Principle, the 4-metric, also known as the Robertson-Walker metric, of a homogeneous and isotropic spacetime can be written in polar-coordinates as

$$\begin{aligned} \mathrm{d}s^2 &= \mathrm{d}t^2 - \mathrm{d}l^2 \\ &= \mathrm{d}t^2 - a^2(t)\left[\frac{\mathrm{d}r^2}{1-kr^2} + r^2\mathrm{d}\theta^2 + r^2\sin^2\theta\mathrm{d}\varphi^2\right], \end{aligned} \tag{1.1}$$

where k is a constant representing the curvature of the space, and $a(t)$ is the scale factor which describes the size of the space. Subsequently, the proper distance between two observers at $r = 0$ and (r_0, θ, φ) can be written as

$$l = a(t)\int_0^{r_0} \frac{\mathrm{d}r}{\sqrt{1-kr^2}} = a(t)\chi(r_0), \tag{1.2}$$

where $\chi(r_0)$ is the co-moving distance between the two observers.

Without involving General Relativity, some important concepts in cosmology can already be introduced, such as the following:

- The Hubble parameter, which indicates the change rate of the proper distance between two observers, is then defined through the change rate of the scale factor, as follows
$$H(t) = \frac{\dot{a}(t)}{a(t)}. \tag{1.3}$$

- Redshift is an important concept in modern cosmology as all astronomical observations are made through the light signal. For photons, they travel along the null geodesics, i.e, $\mathrm{d}s = 0$, in other words, $\mathrm{d}\tau = \mathrm{d}\chi$, where τ is the conformal time which can be represented as $\tau = \int \mathrm{d}t/a(t)$. By definition, the redshift of a photon is written as
$$z \equiv \frac{\lambda_0}{\lambda_\mathrm{e}} - 1 \tag{1.4}$$
where λ_0 and λ_e are the wavelengths at the emitter and the receiver, respectively. Under Robertson-Walker metric, it is easy to write z in terms of the scale factor,
$$z = \frac{a(t_0)}{a(t_\mathrm{e})} - 1. \tag{1.5}$$

As we have mentioned before, the dynamics of the spacetime is determined by its mass content. Since the matter distribution is homogeneous and isotropic on large-scales, the evolution of the spacetime, specifically the scale factor $a(t)$ and k, can be obtained by applying the General Relativity. The Einstein's field equation goes,

$$R_{\mu\nu} = 8\pi G \left(T_{\mu\nu} - \frac{1}{2} g_{\mu\nu} T^{\lambda}_{\lambda} \right), \tag{1.6}$$

where $R_{\mu\nu}$ is the Ricci tensor describing the local curvature, and is determined by the metric tensor $g_{\mu\nu}$ as well as the energy momentum tensor of the mass content, $T_{\mu\nu}$. Assuming the matter content in the universe is a uniform ideal fluid with density ρ and pressure P and without peculiar motion, we then have

$$\begin{aligned} \ddot{a} &= -\frac{4\pi G}{3}(\rho + 3P)a \\ \left(\frac{\dot{a}}{a}\right)^2 &= \frac{8\pi G\rho}{3} - \frac{k}{a^2}. \end{aligned} \tag{1.7}$$

The second equation is the Friedman equation. Note there are several mass contents that contribute to the density ρ in the Friedman equation, including a nonrelativistic matter component ($\rho_{\rm m}$, which scales with a^{-3}), a relativistic radiation component ($\rho_{\rm r}$, which scales with a^{-4} and dominates the universe before $z > 3600$) and a possible constant vacuum energy component (ρ_Λ). Let us use subscript "0" to denote the present time to define the critical density $\rho_{\rm c,0} = 3H_0^2/8\pi G$, as well as the cosmological parameters, $\Omega_{\rm m,0} = \rho_{\rm m,0}/\rho_{\rm c,0}$, $\Omega_{\rm r,0} = \rho_{\rm r,0}/\rho_{\rm c,0}$, $\Omega_{\Lambda,0} = \rho_\Lambda/\rho_{\rm c,0}$, and note that $k = H_0^2 a_0^2(\Omega_{\rm m,0} + \Omega_{\rm r,0} + \Omega_{\Lambda,0} - 1) = H_0^2 a_0^2(\Omega_0 - 1)$. By substituting these components into equation (1.7), we have

$$\frac{H^2(z)}{H_0^2} = \Omega_{\Lambda,0} + (1 - \Omega_0)(1+z)^2 + \Omega_{\rm m,0}(1+z)^3 + \Omega_{\rm r,0}(1+z)^4. \tag{1.8}$$

This is the equation that relates the matter content and the scale factor of the universe. Combination of recent studies, such as high-redshift supernovae survey (e.g.,

Perlmutter et al., 1999), and WMAP (Wilkinson Microwave Anisotropy Probe, e.g. Spergel et al., 2007) suggest a flat universe with $\Omega_{\rm m,0} \sim 0.3$, $\Omega_{\Lambda,0} \sim 0.7$ and $H_0 \sim$ 70km/s/ Mpc, which is commonly used in the simulations.

1.1.2 Gravitational clustering

A cosmological density field is unstable. Gravitational force drives the initially overdense regions to grow more overdense with the passage of time. The time evolution of a fluid is specified by the equation of continuity, Euler's equation and the Poisson equation. Based on these three equations, for pressureless and adiabatic fluid, a small density perturbation δ on scale larger than the Jeans Length satisfies (in Fourier space),

$$\frac{{\rm d}^2\delta_{\mathbf{k}}}{{\rm d}t^2} + \frac{2\dot{a}}{a}\frac{{\rm d}\delta_{\mathbf{k}}}{{\rm d}t} = 4\pi G\rho_{\rm m}\delta_{\mathbf{k}}, \tag{1.9}$$

where $\delta_{\mathbf{k}}$ is the Fourier transform of δ and a is the scale factor. Usually, solving the equation of the perturbation into the non-linear regime is always hard. However, given a cosmological model, a good approximation of the growing mode of the perturbation, δ_+, in the linear regime can be written as,

$$\begin{cases} \delta_+ & \propto & D(z) \propto g(z)/(1+z) \\ g(z) & \approx & \frac{5/2\Omega_{\rm m}(z)}{\Omega_{\rm m}^{4/7}(z) - \Omega_\Lambda(z) + [1+\Omega_{\rm m}(z)/2][1+\Omega_\Lambda(z)/70]} \end{cases} \tag{1.10}$$

where $D(z)$ is the so-called linear growth factor and $g(z)$ was found by Carroll, Press & Turner (1992).

The linear theory of small perturbation is widely used in semi-analytical models of large-scale structure formation. However, it is not sufficient, because the virialized objects, such as dark matter halos, form in highly non-linear process. A simple model to describe the non-linear growth of massive objects is the top-hat model. In

the most commonly studied flat universe with a cosmological constant Λ, the motion of a spherical mass shell with radius R is given by

$$\frac{\mathrm{d}^2 R}{\mathrm{d}t^2} = -\frac{GM}{R^2} + \frac{\Lambda}{3} R. \tag{1.11}$$

Let us assume the small density perturbation of the initial sphere to the background density is $\delta_{\rm i}$, and the sphere becomes virialized when its potential energy U and kinetic energy K satisfy the Virial Theorem, i.e., $U + 2K = 0$ (which most workers prefer to assume to be achieved at the time of collapse, $t_{\rm col}$). Then solving equation (1.11) to the first-order, we have, for the linear perturbation at the time of collapse,

$$\delta_{\rm l}(t_{\rm col}) = \frac{3}{5}\left(\frac{3\pi}{2}\right)^{\frac{2}{3}} \left[\Omega_{\rm m}(t_{\rm col})\right]^{0.0055} \approx 1.69, \tag{1.12}$$

where $\delta_{\rm c} \equiv \delta_{\rm l}(t_{\rm col}) = 1.69$ is called the linear critical overdensity for collapse; at the mean time, the true density of the sphere is about 180 times the background density. These two quantities are often used in semi-analytical and N-body simulations to indicate the criteria of a virialized dark matter halo.

In the reality, though, dark halo formation is a much more complicated process than the simple model described above. First, at initial stage, for the power spectrum of the density field, $P_{\rm i}(k)$, there are several physical processes that can change the initial growth of the density perturbation at early time. These effects include some damping processes such as Silk-damping and free-streaming. In the CDM scheme, these effects are included in the CDM linear transfer function T (Bardeen et al., 1986)

$$T(q) = \frac{\ln(1+2.34q)}{2.34q}\left[1 + 3.89q + (16.1q)^2 + (5.46q)^3 + (6.71q)^4\right]^{-\frac{1}{4}} \tag{1.13}$$

$$q = \frac{1}{\Gamma}\left[\frac{k(\mathrm{Mpc}^{-1})}{h}\right] \tag{1.14}$$

where Γ is the shape parameter, so that the real power spectrum $P(k) = P_{\rm i}T^2(k)$. Secondly, the collapse of a dark matter halo is not spherical. As one can see from the simulations, the densest structures, dark matter halos, are often seen at the nodes of the filamentary networks. The shape of these virialized objects are mostly ellipsoidal. Therefore, study of the non-linear clustering of the dark matter heavily relies on the cosmological N-body simulations.

1.2 Overview of the properties of dark matter halos

As mentioned, dark matter is the major mass component in the universe and dominates the evolution of the cosmic density field. In the CDM scenario, most mass in the universe ends up in virialized objects, called dark matter halos (dark halos). Dark halos form through frequent mergers, in the sense that small halos interact and merge together to form larger halos. Accordingly, this scenario is known as hierarchical structure formation. Luminous objects, such as galaxies, are supposed to form and evolve in such halos (White & Rees, 1978). The understanding of dark matter halo formation is therefore critical because of its direct link to the formation process of the large-scale structure and luminous galaxies.

Fig. 1.1 shows a projection of the present-day mass distribution through a $10h^{-1}$Mpc thick slice in an N-body simulation, carried out in a cube with $300\,h^{-1}$Mpc on a side. This simulation will be used to study the dark halo mass accretion history in Chapter 1. Clearly, the density field has heavily evolved from the nearly homogeneous distribution at very early time. Most mass in the simulation has aggregated into highly non-linear regions, such as the filamentary or sheet-like structures, called the "cosmic web". In the nodes of the cosmic web, numerous mass clumps, the dark matter halos, are often seen and contain most of the mass in the universe. Techniques such as the spherical over-density algorithm and Friends-Of-Friends algorithm are often used to identify these halos.

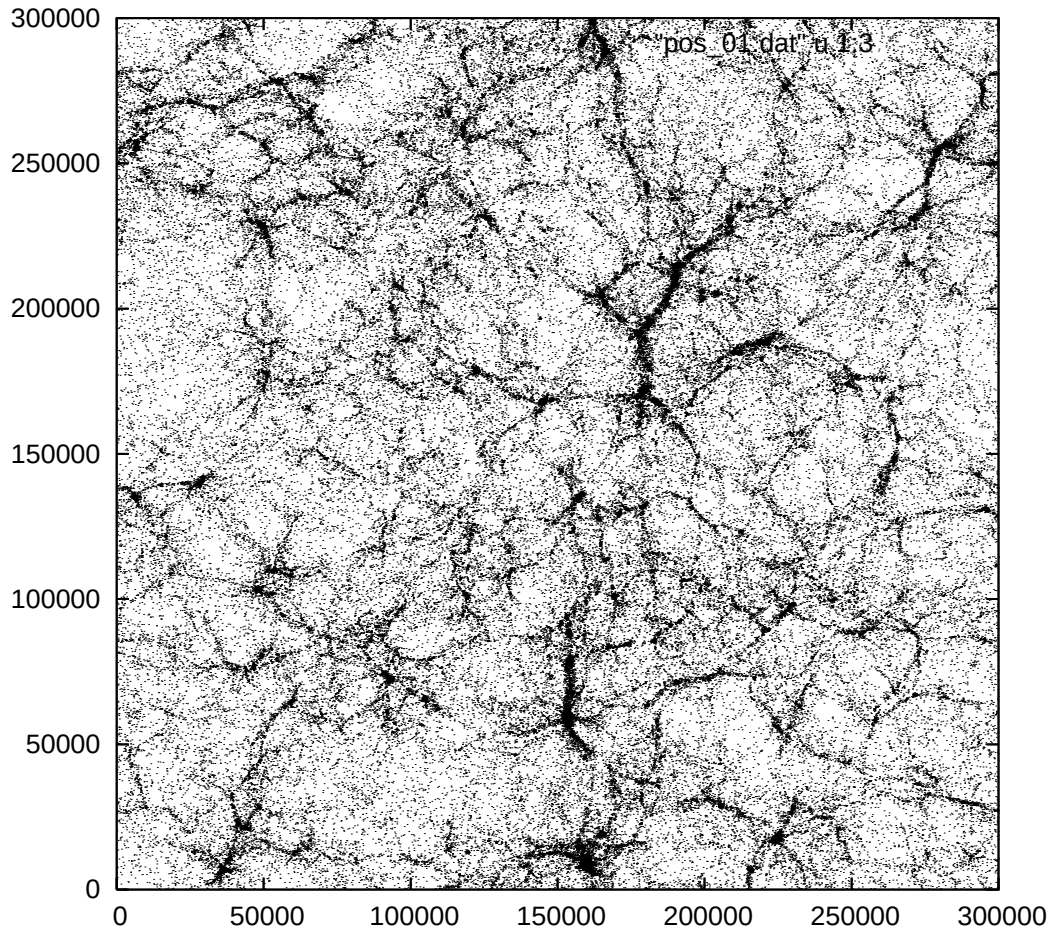

Figure 1.1. A projection of the mass distribution at $z = 0$ in an N-body simulation in a cube with 300 h^{-1}Mpc on a side. Each dot represents a dark matter particle, and both axes are in the units of h^{-1}kpc. This figure represents a 10 h^{-1}Mpc slice through the simulation.

Generally speaking, there are three key properties of dark halos that dominate the formation of galaxies: the internal structural property which populates galaxies, the formation history which determines the assembly of galaxies, the clustering property which sets up the environment of galaxies. In the past two decades, with the development of both N-body simulations and semi-analytical methods, many important results have been obtained regarding the properties of dark matter halos in the current CDM paradigm of structure formation. Specifically, these studies include halo mass function (e.g., Bond et al., 1991; Lacey & Cole, 1993; Sheth & Torman, 1999;

Sheth, Mo & Torman, 2001; Warren et al., 2006), density and sub-halo profile (e.g., Navarro, Frenk & White, 1997; Bullock et al., 2001b; Eke, Navarro & Steinmetz, 2001; Gao et al., 2004a; Lu et al., 2006), angular momentum property (e.g., Barnes & Efstathiou, 1987; Cole & Lacey, 1996; Bullock et al., 2001a; Chen & Jing, 2002), clustering property (e.g., Mo & White, 1996; Jing, 1998; Lemson & Kauffmann, 1999; Sheth & Torman, 1999; Sheth, Mo & Torman, 2001; Gao et al., 2005), and merging history (e.g., Kauffmann et al., 1993; Syer & While, 1998; Li et al., 2007; Stewart et al., 2008; Giocoli et al., 2008a). The formation of dark halos is apparently quite complex. Besides the importance of individual halo property, it has been shown that multiple halo properties can be actually intertwined. For example, halo concentration depends strongly on the detailed mass accretion history of a halo (e.g., Wechsler et al., 2002; Zhao et al., 2003a,b); the halo clustering property also tightly correlates with the age of dark halos (e.g., Sheth & Torman, 2004; Gao et al., 2005; Wechsler et al., 2006; Li et al., 2008).

Above results have been playing an important role in our understanding of galaxy formation. In the rest of this Chapter, I will give a brief review of some properties mentioned above.

1.2.1 Dark halo density profile and concentration

The dark matter halos are assumed to form hierarchically bottom-up via gravitational amplification of initial density fluctuations. A commonly used method to study the dark halo internal structure is the cosmological N-body simulation. In the N-body simulations, dark matter is modeled as collisionless fluid represented by N particles under the influence of gravitational forces of their own, and fulfills the collisionless Boltzmann equation. The gravitational forces are then integrated numerically following the evolution of the density field. The aggregation of the self-gravitating dark matter in the simulated universe subsequently collapses into the

non-linear structures identified as dark matter halos. Numerous N-body simulations carried out by different authors have confirmed that the dark halo internal mass distribution follows a "universal density profile", first found by Navarro, Frenk & White (1996, 1997, hereafter NFW), and known as the NFW density profile afterwards. It has been demonstrated repeatedly that the NFW profile reasonably well describes the intrinsic density of dark halos with a wide range of mass (from sub-galaxy-sized to cluster-sized), and in various cosmological models (e.g., Moore et al., 1999a; Jing & Suto, 2000; Eke, Navarro & Steinmetz, 2001; Bullock et al., 2001b).

According to Navarro, Frenk & White (1997), the dark halo density profile is described by the following functional form,

$$\rho(r) = \rho_{\rm c} \frac{\delta_0}{(r/r_{\rm s})(1 + r/r_{\rm s})^2}, \tag{1.15}$$

where $\rho_{\rm c}$ is the critical density for a closed universe, δ_0 is a free parameter, and $r_{\rm s}$ is a characteristic radius at which the logarithmic slope of the density distribution $\mathrm{d}\ln\rho/\mathrm{d}\ln r = -2$, and $\rho(r_{\rm s}) = \rho_{\rm c}\delta_0/4$. In addition, $r_{\rm s}$ is associated with $R_{\rm v}$, the "virial radius" of a halo, through the *concentration parameter*, c, defined by $c = R_{\rm v}/r_{\rm s}$. Fig. 1.2 shows the NFW density profile from N-body simulations of various cosmological model (Navarro, Frenk & White, 1997). According to equation (1.15), in the inner region where $r \ll r_{\rm s}$, dark halo density profile follows a power-law with power index -1, while at the outer region where $r \gg r_{\rm s}$ the power index becomes -3. Define the density contrast between the halo mean density and $\rho_{\rm c}$ as $\Delta_{\rm vir}$, for which we adopt the fitting formula proposed by Bryan & Norman (1998),

$$\Delta_{\rm vir}(z) = 18\pi^2 + 82[\Omega_{\rm m}(z) - 1] - 39[\Omega_{\rm m}(z) - 1]^2, \tag{1.16}$$

where $\Omega_{\rm m}(z)$ is the cosmological parameter of the mass fraction at redshift z. Subsequently we have

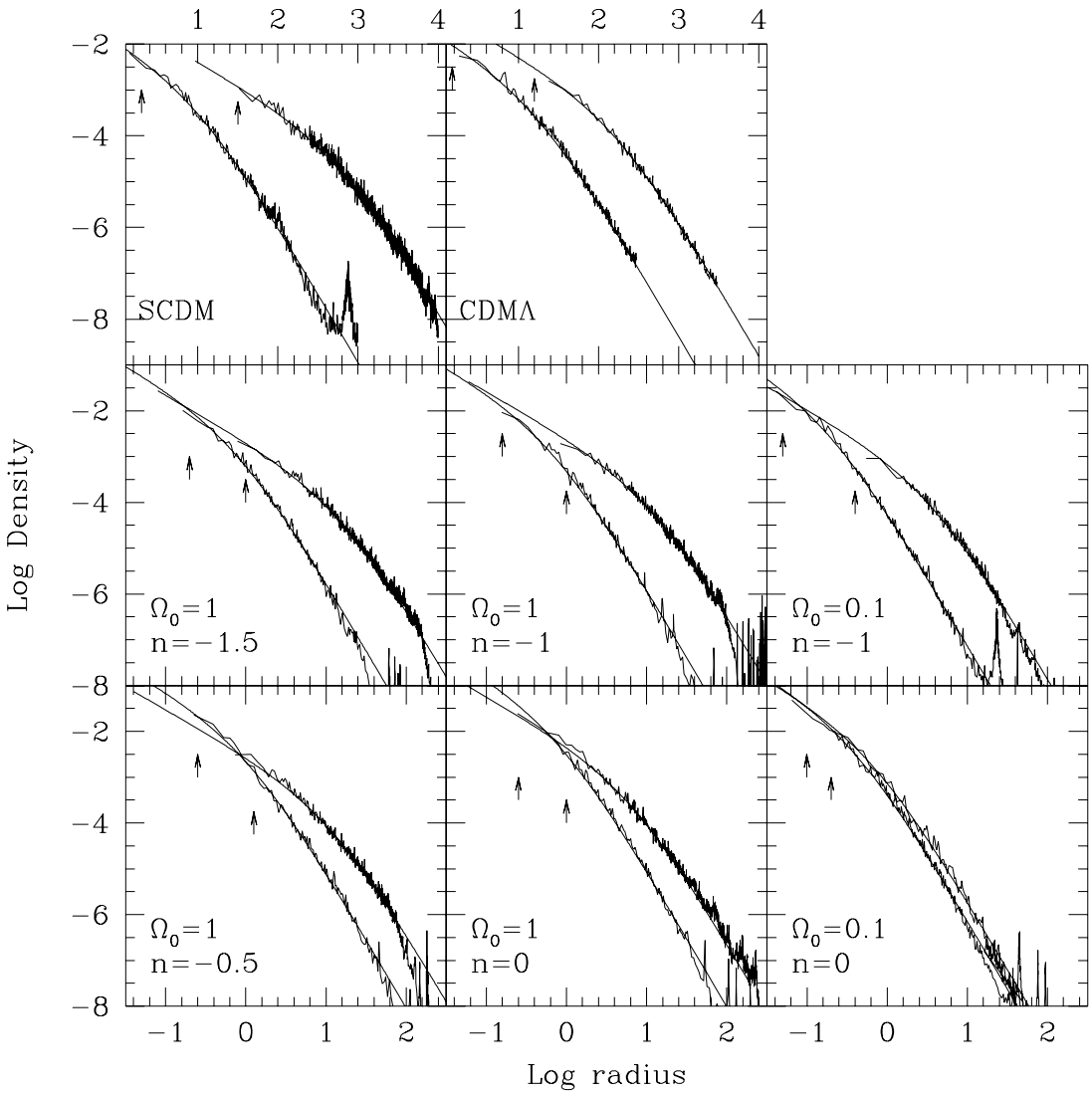

Figure 1.2. Density profile of dark halos identified in simulated cosmogonies, as indicated in the panels. In each panel leftmost curve represents the small system. Solid lines are best fit according to equation (1.15). In the SCDM and CDMΛ models radii are given in the units of kpc and densities are in the units of $10^{10}h^{-1}M_{\odot}/\mathrm{kpc}^3$. Ω_0 and n indicates the cosmological density parameter and the power-index of the power spectrum. Arrows indicate the scale of gravitational softening. Plot is provided by Navarro, Frenk & White (1997).

$$\delta_0 = \frac{\Delta}{3}\frac{c^3}{\ln(c+1) - c/(c+1)}. \tag{1.17}$$

Given cosmological model, equation (1.17) indicates that the density profile of a dark halo is solely a function of c, which determines the compactness of a halo, in the sense that a larger value of c means a halo being more compact.

On average, small halos have larger concentration, because they assemble their central regions relatively earlier than massive halos. For halos with fixed mass, the concentration parameter c is a monotonically decreasing function of redshift z [$c \propto (1+z)^{-1}$, (Bullock et al., 2001b)], with large scatter. Jing (2000) and Bullock et al. (2001b) independently reported that present-day halos with fixed mass show a considerable dispersion in the concentration parameter. Given the halo mass, the dispersion in c can be well-represented by a log-normal probability distribution, with $\sigma_{\ln c} \approx 0.2 - 0.3$. Other authors also pointed out that although NFW profile is generally a good description of halo density profile, there is evidence that for small galactic halos the inner density slope can be deeper than NFW (Moore et al., 1999a; Jing & Suto, 2000). Apparently, these arguments imply a profound complexity in the formation of dark halos and a possible link between halo density profile and its formation history.

There have been several explanations on the origin of dark halo density profile and its dispersion. Some authors suggested that the details of the mass accretion history play a key role in shaping the internal mass distribution of dark halos (Wechsler et al., 2002; Zhao et al., 2003a,b; Lu et al., 2006). Lu et al. (2006) suggested that the configuration of the dark halo density profile is determined by the two accretion phases during the halo mass assembly history. An early fast phase with isotropic mass accretion builds up and sustains the central region characterized by $r_{\rm s}$, and a later slow mass inflow eventually forms a shallower halo outskirt.

1.2.2 Dark halo merging tree

In the standard scheme of CDM cosmology, dark halo assembles hierarchically. Smaller halos form first at higher redshift, and then merge along to form larger halos as the time progresses. This picture is a generic consequence of the shape of CDM power spectrum. Although the details of the dark halo assembly are very complicated, it is generally recognized that halo formation history can be represented and traced with either semi-analytical methods or N-body simulations. In the simulated universe, high-redshift small halos that eventually settle their mass into a final halo are referred to as "progenitors" of the halo. With the identified mass and redshift of each progenitor, one can chain up these quantities chronologically and generate the so-called "merging tree" of a dark halo. Based upon the dark halo merging tree, other essential assumptions, for instance gas cooling, star formation, feedbacks and so on can therefore be deployed to model the formation of galaxies. Although the construction of a merging tree involves several artificial definitions such as halo mass, it is nevertheless an efficient way that enables us to develop a backbone for modeling galaxy formation.

Fig. 1.3 illustrates the merging tree of a dark halo identified in an CDM cosmological N-body simulation. The lowest/biggest gray filled circle represents the final dark halo, smaller gray filled circles are its progenitors at higher redshift. The mergers between two progenitors are indicated by the solid lines. Clearly, in the CDM cosmology, there are more small halos at higher redshift than the lower redshift. A final halo is assembled through mergers between these small halos.

At the current stage, there are primarily three methods commonly used to construct the dark halo merging trees, listed and discussed in the following.

- The first one is the extended Press-Schechter formalism (e.g., Bond et al., 1991; Bower, 1991; Lacey & Cole, 1993), also known as the "excursion set" theory. Assuming a Gaussian initial perturbation field and a spherical halo collapse

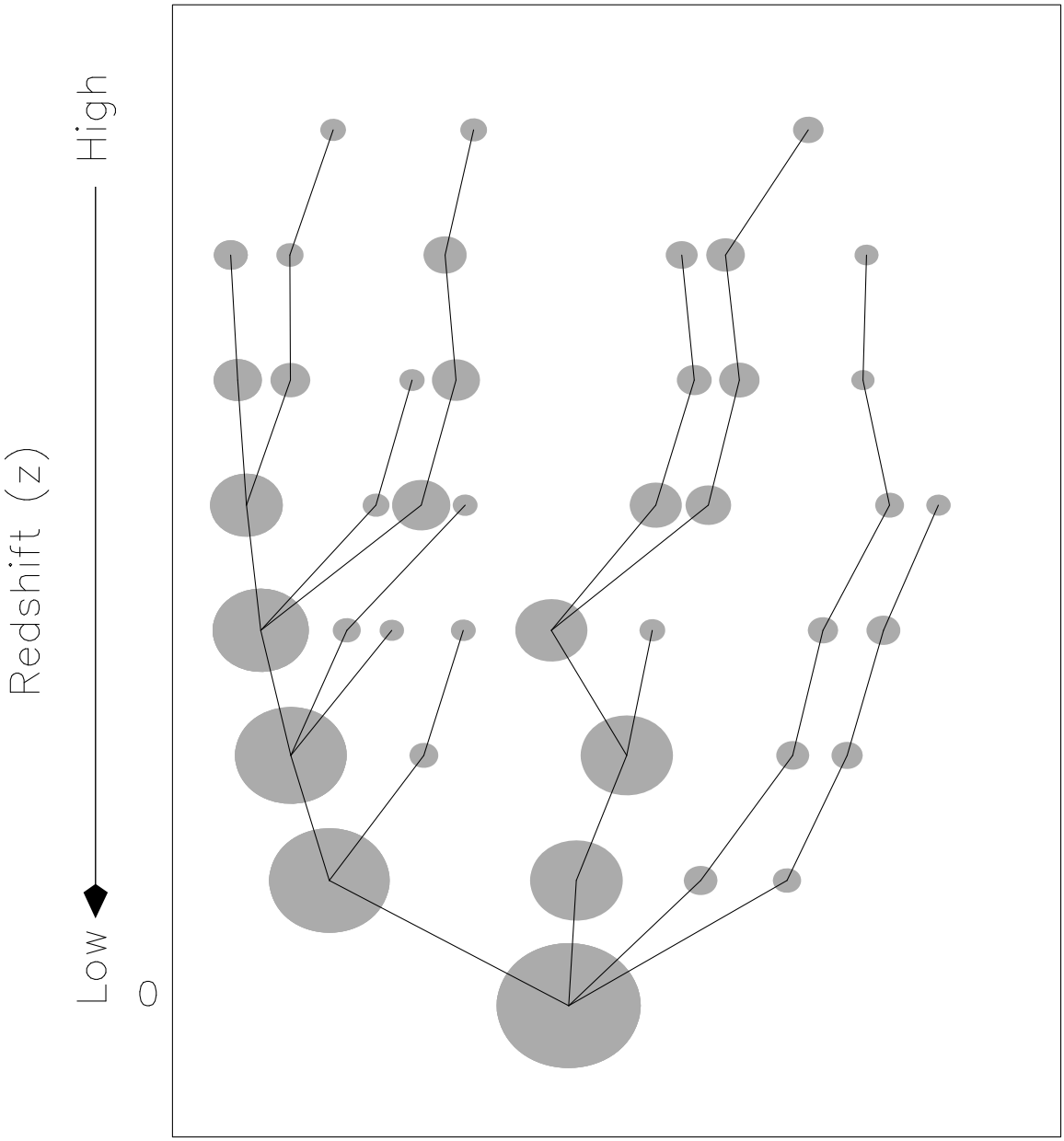

Figure 1.3. An exemplary dark halo merging tree. Each gray filled circle represents a progenitor. Progenitors at the same horizontal level are at the same redshift. Each progenitor is connected (by black solid lines) with its main progenitor at higher redshift and/or descendant at lower redshift. A convergence of two solid lines indicates a merger between two progenitors.

model, this method provides a self-consistent and scale-free upcrossing barrier of collapsing halos, which in turn enables a relatively simple and less computationally expensive way to describe the mass accumulation history of dark halos.

- The second method is known as "ellipsoidal collapse model", which corrects the false assumption that all halos form spherically. In reality, under the influences of large-scale tidal torques, dark halos are usually elongated and cannot sustain a spherical shape during the formation process (e.g. Bond & Myers, 1996a,b; Sheth, Mo & Torman, 2001). Sheth & Torman (1999) thus incorporated this effect and suggested an alternative ellipsoidal halo collapsing theory. This theory has alleviated the inaccuracy rooted in the spherical collapse assumption, but it fails to predict an accurate moving barrier on different scales in order to construct the merging history of dark halos. Fortunately, though, Monaco et al. (2002a,b) introduced a semi-numerical approach, PINOCCHIO , which uses Lagrangian perturbation theory to describe the dynamics of collapsed mass and trace the merging history of dark halos.

- The third commonly used method is the cosmological N-body simulation. Given a cosmological model, N-body simulations use massive particles to represent the initial density field in a cube and follow the gravitational evolution of these particles into the non-linear dynamic regime. In an N-body simulation, density field at different redshifts are recorded with snapshots, and dark halos are further identified. With sensible criteria, halos at different snapshots are then connected according to their kinship. N-body simulations are by far the most accurate yet most computationally expensive approach to monitor the assembly history of dark halos.

The details and comparisons of above methods will be presented and discussed in the next Chapter.

1.2.3 Dark halo formation time and the assembly history

An critical piece of information regarding the build-up of large-scale structure is the assembly of dark matter halos, which are the quasi-equilibrium systems composed

of dark matter aggregated through the non-linear gravitational collapse. As mentioned before, the assembly details of dark halos may affect the structural properties of the final halo. Besides, since the galaxies and other luminous objects are assumed to form through the cooling and condensation of baryonic component within these halos, the detailed description of dark halo assembly history would be of fundamental importance for the understanding of the properties of luminous objects.

A simple way to monitor the growth of a dark halo is to characterize the growth history of its main (usually the most massive) progenitor based on the halo merging tree. Since the mass accretion of a dark halo is in general a continuous process, the term "dark halo formation time" is quite ambiguous and requires a sensible and quantitative definition. In the literature, different authors define various "formation times" to reflect particular epochs (e.g., Wechsler et al., 2002; Li et al., 2008) in the halo assembly history. In most cases, however, the dark halo formation time refers to the time when the main progenitor acquires half of the final halo mass.

Fig. 1.4 shows the probability distribution of the time when a dark halo main progenitor acquires half of the halo mass in a standard ΛCDM model with $\Omega_0 = 0.3$, $\Omega_\Lambda = 0.7$, dimensionless Hubble parameter $h = 0.67$, and the r.m.s. linear overdensity at $z = 0$ in spheres of radius $8h^{-1}$ Mpc, σ_8, equals 0.9. Predictions from several different methods, including N-body simulation (Jing & Suto, 2002; Lin et al., 2003), extended Press-Schechter formalism (e.g., Lacey & Cole, 1993), ellipsoidal collapse model (Sheth, Mo & Torman, 2001) and non-spherical collapse boundary model (Chiueh et al., 2001), are compared. It is clear that on average, massive halos form later than small halos in the CDM scheme. For fixed halo mass, the formation time distribution spans a wide range of redshift (time). Notice that under the same cosmological model, the probability distributions of dark halo formation time predicted by different analytical methods actually differ significantly. Their differences from the N-body simulation are caused by the inaccuracies of these models.

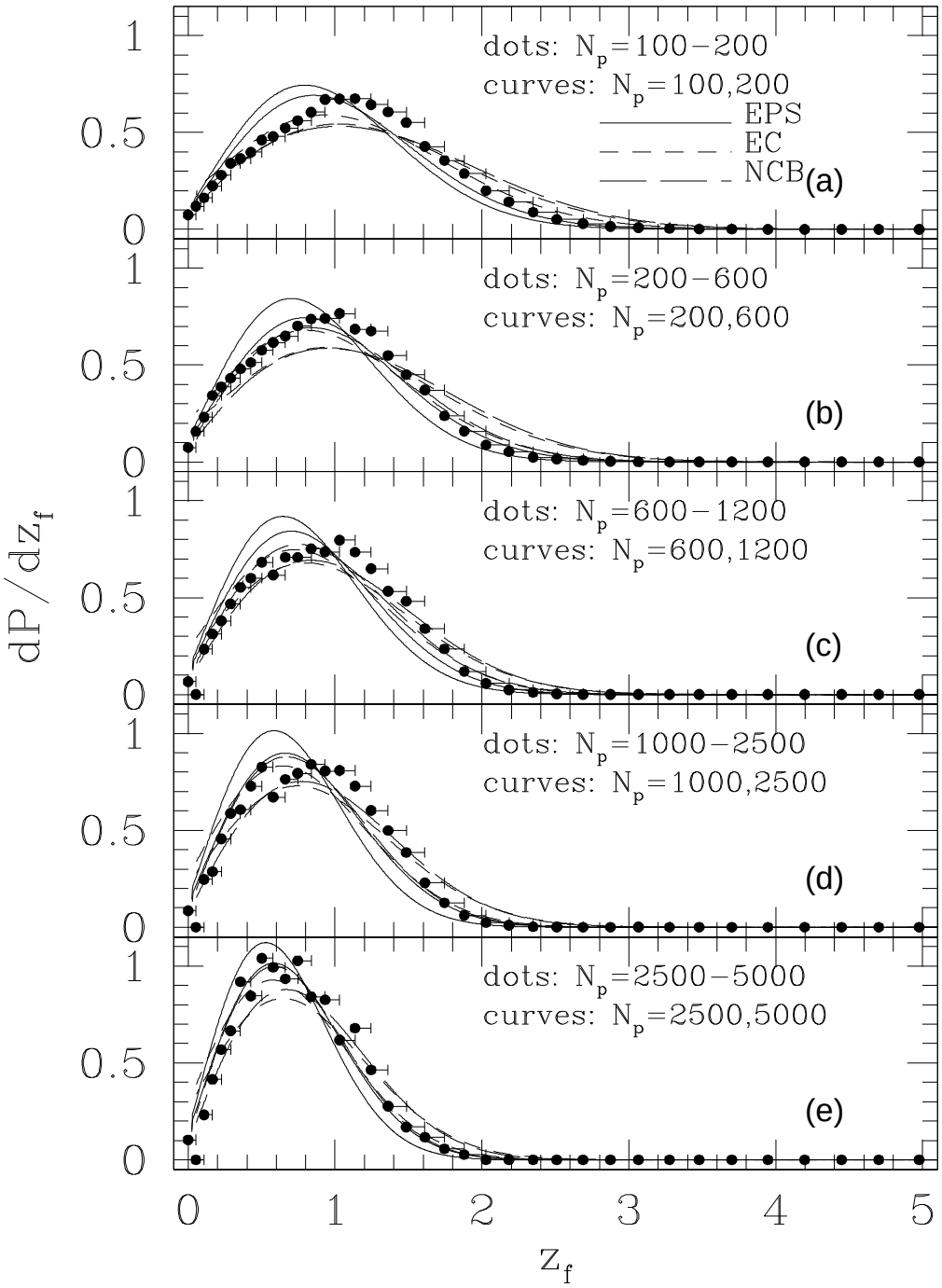

Figure 1.4. Dark halo formation time. Shown here is the probability distribution function of dark halo formation time (the time when the halo main progenitor acquires halo of the final halo mass, Lin et al., 2003) in a standard ΛCDM model. Each panel represents dark halos with different mass [indicated by the number ($N_{\rm p}$) of particles whose mass is $1.67 \times 10^{10}\ h^{-1}{\rm M}_{\odot}$ each]. Points with error bars are results from an N-body simulation. Solid lines are the prediction of the extended Press-Schechter formalism (EPS); short-dashed lines are the predictions of the ellipsoidal collapse (EC) model (Sheth, Mo & Torman, 2001); long-dashed lines are the prediction from non-spherical collapse boundary (NCB) model (Chiueh et al., 2001).

Since the mass assembly process of dark halos is very stochastic, as shown in Fig. 1.4, it is thus difficult to characterize the formation history of individual halos using a single parameter such as the formation time. Wechsler et al. (2002) suggested that both average mass accretion histories and mass accretion histories for individual halos, can be well described by the following function:

$$M(z) = M_0 \exp(-\alpha z), \tag{1.18}$$

where $M(z)$ stands for the halo mass at given redshift z, $M_0 = M(0)$ is the halo mass at redshift $z = 0$, and α is a free parameter. Interestingly, they found for a given present-day halo, α is linked to its concentration parameter, c, through $\alpha = 8.2/c$. This directly shows that the halo density profile is correlated with its formation history.

Using a different set of equations, Zhao et al. (2003a,b) confirmed that there exists a tight scaling relation between the mass in the central region of a dark halo and its concentration. In addition, they also suggested that the dark halo mass accretion history is not a gradual process, as one naively expects from equation (1.18). It is, instead, a process which can be divided roughly into two phases with different properties: a fast accretion phase which is constantly disturbed by sudden mass jumps through mergers, and a slow accretion phase which is composed of relatively smoother mass inflow. Their method, however, does not provide an easily characterized epoch that separates these two phases. As we will demonstrate in the next Chapter, this epoch is the time when the dark halo potential well reaches its historical maximum during its mass accretion process.

1.2.4 Sub-structure population of dark halos

Dark halos assemble into place through mergers and accretion. The internal structure of a forming halo has been of keen interests to populate the luminous galaxies.

In principle, the central regions of early virialized dark halos can be very compact and hence resistant to the dynamic effects during their incorporation into larger systems. As a result, the self-bound residues of these dark halos become the so-called "sub-structures", also know as sub-halos of their host halos. Since galaxies form by the condensation of gas at the centers of early halos and therefore can be well-associated with the sub-structures at later time, the properties and evolution of sub-structures within parent halos on different mass scales are a key piece of information relating sub-halos to the star formation history of their associated galaxies.

Obviously, a fundamental property of sub-halos is their abundance. Since sub-halos usually experience strong dynamical effects such as friction and stripping, there are two ingredients that would contribute to shape the final (*evolved*) sub-halo mass function. The first is the mass function of the infalling progenitors at the time of merger (also known as the *unevolved* sub-halo mass function); the second is the detailed dynamical effects mentioned above that cause sub-halos to lose mass. So far there have been several analytical studies of the sub-halo population based on the extended Press-Schechter formalism (e.g., Sheth, 2003; Giocoli et al., 2008b). These studies logically link the progenitors of a given parent halo to its present-day sub-halos and can be very useful to understand the origin of the sub-halo population. However, due to insufficient modeling, these studies ignore the fact that sub-halos would experience significant amount of mass loss during their post-merger evolution (e.g., van den Bosch et al., 2005; Giocoli et al., 2008a; Angulo et al., 2008b). Therefore, the detailed study of sub-halo properties also relies strongly on the N-body simulations that cover large volumes and a wide range of halo mass.

Interestingly, during the past few years, using different N-body simulations, a number of authors actually revealed seemingly controversial conclusions on the *evolved* sub-halo mass function (e.g., Moore et al., 1999a; De Lucia et al., 2004; Gao et al., 2004a). The first two groups claimed that the *scaled* mass function of sub-halos,

within parent halos in the mass range from galaxy-size to cluster-size, show little dependence on the mass of the parent halo, and can be described by an identical power-law. However, Gao et al. (2004a) (see also Shaw et al., 2007; Diemand et al., 2007) argued that the scaled sub-halo population actually depends on the host halo mass, especially for massive sub-halos. The sub-halo abundance in high-mass host halos is slightly higher than in low-mass host halos. As pointed out by Zentner & Bullock (2003), sub-halo mass fraction increases with host halo mass because massive halos experience more mergers at later time. Per the similarity in small sub-halo abundance found in host halos with different masses, a possible explanation to the argument of Zentner & Bullock (2003) is the higher abundance of massive sub-halos in high-mass systems. Subsequent study carried out by Angulo et al. (2008b) argued that the discovery by Gao et al. (2004a) only holds in the power-law region of the sub-halo mass function. They further suggested that when the sub-halo mass increases to even higher range ($M_{\rm sub}/M_{\rm h} > 0.04$, which requires a very large simulation volume for good statistics), the power-law would not hold and the dependence on host halo mass would reverse. Nevertheless, the difference in these studies is marginal and can be very likely caused by the different mass resolution of their simulations as well as the techniques used to identify sub-structures in the simulated dark halos. According to Angulo et al. (2008b), the *evolved* sub-halo mass function follows an arguably "universal" form:

$$\frac{{\rm d}N_{\rm sub}}{{\rm d}\ln(M_{\rm sub}/M_{\rm h})} = A\left(\frac{M_{\rm sub}}{M_{\rm h}}\right)^{\alpha} \exp\left[-\frac{1}{\sigma^2}\left(\frac{M_{\rm sub}}{M_{\rm h}}\right)^2\right], \tag{1.19}$$

where $N_{\rm sub}$ is the number of present-day sub-halos, $M_{\rm sub}$ and $M_{\rm h}$ represents the masses of sub-halos and of the host halo. The best-fit parameters $A \approx 2$, $\alpha \approx -0.9$, $\sigma \approx 0.16$, which are almost independent of the mass and redshift of the host halo.

In principle, the fraction of mass bounded to the sub-halos depends on the resolution limit of the simulations. Numerous N-body simulations to date revealed that

the resolved sub-structures contain about 10% of the total mass of a halo system, with a slight dependence on host halo mass (Ghigna et al., 2000; Gao et al., 2004a). Given a fixed mass resolution, high-mass systems tend to invest more mass in their sub-halos. Another useful perspective into the sub-structure mass fraction is to look at the fractional mass within sub-structures rank-ordered in size. Using N-body simulations, Angulo et al. (2008b) suggested that, albeit with large scatter, the most massive sub-halo on average contains about 4% of the total mass of a halo system while the second and third largest sub-halos contain about 1.5% and 1% of the mass, respectively.

Clearly, the present-day sub-halos are the consequence of heavy dynamical effects after merging, and the statistics of their population could be affected by the simulation techniques. In Chapter 4, we will demonstrate that a large portion of sub-halos have been dissolved completely after their incorporation into the host halo, and the remaining sub-structures identified in the final host halos represent a very special subset of the total sub-halo population accreted into host halos. Subsequently, the *evolved* sub-halo mass function substantially deviates from the *unevolved* one, which can be well-described by a "universal" functional form. It is worth noting that compared with the evolved sub-halo mass function, the unevolved one is in a closer connection with galaxy mergers as the stellar component of central galaxies is relatively more resilient to the tidal disruption. In addition, the *unevolved* mass function of infalling sub-halos is much less affected by the influences from artificial simulation techniques to identify sub-halos, and therefore relatively more robust.

1.2.5 Halo bias

The properties of galaxies, such as stellar mass, color, luminosity, star formation rate, are well established to be dependent on the environment. Since dark halos are the hosts of galaxies, this can be understood as a consequence of the fact that halos

with different masses and formation histories cluster differently hence host different galaxy populations. In the CDM paradigm, the clustering property of dark halos is completely determined by the initial power spectrum of the density fluctuations. However, since dark halos are highly virialized objects, their spatial distribution does not exactly follow that of the dark matter. Bardeen et al. (1986) showed that if dark halos are associated with the high peaks of the initial density field then they could be more strongly clustered than the underlying dark matter.

The clustering strength of an object kind is usually described by the autocorrelation (two-point correlation) function $\xi_{\rm obj}(r)$, which essentially measures the excessive rate of detecting object-pairs on a distance r compared to a completely random spatial distribution (Peebles, 1980). The autocorrelation function of dark halos $\xi_{\rm hh}$ can be obtained by counting halo-pairs in N-body simulations, but its difference from the autocorrelation function of the dark matter, $\xi_{\rm mm}$, could be hard to interpret. Traditionally the halo bias factor b is commonly used to connect $\xi_{\rm hh}$ and $\xi_{\rm mm}$, through the following equation:

$$\xi_{\rm hh}(r) = b^2 \xi_{\rm mm}(r). \tag{1.20}$$

Using an extended approach based on the Press-Schechter formalism, Mo & White (1996) were able to develop an analytical algorithm to derive the halo bias factor b on large scales where the dark matter density fluctuation is still believed to be linear. Let $\sigma(M, z)$ represent the r.m.s. density fluctuation, linearly extrapolated to redshift z, within a sphere which on average encloses mass M. The critical threshold for a halo of mass M_* to collapse in the linear regime can then be defined as $\sigma(M_*, z) = \delta_{\rm c} = 1.686$. The algorithm by Mo & White (1996) predicts that the bias factor b can be simply expressed by

$$b(\nu) = 1 + \frac{\nu^2 - 1}{\delta_{\rm c}}, \tag{1.21}$$

where $\nu = \delta_{\rm c}/\sigma(M, z)$ is the dimensionless amplitude of the density fluctuation that contains mass M. According to equation (1.21), the bias factor is a function of halo

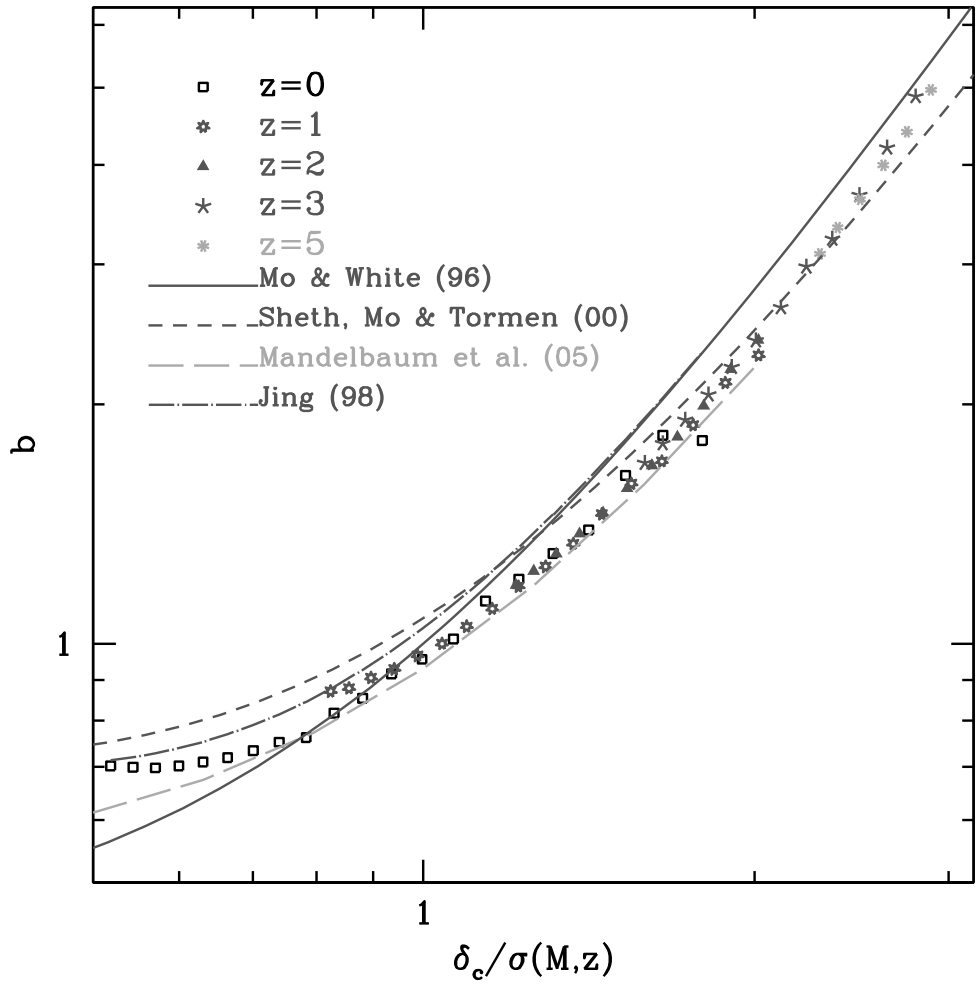

Figure 1.5. Halo bias factor as a function of ν. Different symbols represent the bias factor measured from the Millennium Simulation at different redshift. Solid line and short dashed line are the predictions from Mo & White (1996) and Sheth, Mo & Torman (2001). Long dashed line and dot-dashed line are the fitting results by Mandelbaum et al. (2005) and Jing (1998). Plot is provided by Gao et al. (2005).

mass. For halos more massive than M_*, they should show a positive clustering bias against dark matter; while for halos smaller than M_* they should show a negative clustering bias.

Fig. 1.5 shows the halo bias factor as a function of ν (or equivalently halo mass M), from both analytical models and N-body simulations. Although the result predicted

by Mo & White (1996, solid line in Fig. 1.5) agrees with the N-body simulation fairly well, the agreement is not perfect, especially for small halos (with large σ or small ν), whose bias factor is clearly underestimated. This is due to their simplified assumption that all halos are spherical. Because of the tidal torques exerted by the large-scale structure, less massive halos are more likely to be found within regions which are initially more overdense. On the other hand, the massive halos (with small σ hence large ν) should suffer less from this effect. In fact, after taking the tidal effect into account, i.e., by assuming an ellipsoidal collapse model, Sheth, Mo & Torman (2001) were able to produce better agreement on the halo bias for small halos with the N-body simulations (dashed line in Fig. 1.5).

Recently, Gao et al. (2005) further found that, for halos with fixed mass, the bias factor also shows a strong correlation with the formation time of dark halos (see also Sheth & Torman, 2004). Such correlation is particularly prominent for halos with mass less than M_*, being that halos which form early are much more strongly clustered than their younger counterparts. In addition, Wechsler et al. (2006) and Gao et al. (2007) suggested that besides the halo formation time, halo clustering strength is also a strong function of the halo concentration parameter c. For halos less massive than M_*, those with higher concentration are more clustered than those with lower concentration; while for halos more massive than M_*, this trend changes its sign and highly-concentrated halos become less clustered. Since the formation time and concentration of dark halos are associated with halo assembly history, the dependence of halo bias mentioned above is generally referred to as halo assembly bias. So far there have been several analytical attempts to explain the origin of the halo assembly bias (e.g., Wang, Mo & Jing, 2007; Desjacques, 2008; Dalal et al., 2008). For example, Wang, Mo & Jing (2007) and Dalal et al. (2008) both argued that assembly bias for low mass halos is largely caused by the presence of an old and non-accreting subpopulation of small halos in the vicinity of massive halos.

These non-accreting halos are more strongly clustered than other accreting halos with the same mass, which are negatively biased. For massive halos, however, this effect becomes negligible. Instead, peaks of low curvature from the initial density fluctuations that produce younger halos appear to be more strongly clustered, which is a generic outcome of Gaussian random field.

Halo assembly bias may have non-straightforward yet possibly important influences on the formation of observable objects like galaxies or quasars. Typical halo occupation distribution (HOD) model assumes halo mass to be a deterministic factor that accounts for halo properties. The dependence of halo bias on halo formation time as well as other quantities such as concentration induces caution in these HOD models when calculating galaxy clustering statistics. In fact, subsequent studies (e.g., Zentner et al., 2005; Conroy et al., 2006; Yang et al., 2006; Croton et al., 2007; Tinker et al., 2008; Wang et al., 2008) have not fully agreed with this theoretical speculation, and showed quite different results. For instance, Zentner et al. (2005) suggests that there is little difference between galaxy autocorrelation functions measured in standard HOD model and the N-body simulation which implicitly incorporates the halo assembly bias. Tinker et al. (2008) also found no evident environmental dependence of the properties of SDSS galaxies once the dependence of host halo mass has been accounted for. On the other hand, based on their group catalogue constructed from Two Degree Field Galaxy Redshift Survey (2dFGRS), Yang et al. (2006) found a clear clustering difference between red groups and blue groups, assuming color is a valid indicator of the age of galaxies. Moreover, Croton et al. (2007) found that in their semi-analytical catalogue the clustering bias of red halos is nearly two times as much as the halo assembly bias. The reason of these conflicting results is still under debate. It is possible that the assembly bias based on half mass formation time of dark halos cannot be correctly interpreted into current galaxy formation model.

In Chapter 3, we will use a number of definitions of halo formation time which characterize the different aspects of halo assembly history to further investigate halo assembly bias. Our results suggest that a halo age related to the formation history of its member galaxies should be the most appropriate candidate to associate with the observations to detect the assembly bias. It is also likely that larger simulations combined with more optimized galaxy formation recipe will be needed to finally address this problem.

CHAPTER 2

DARK HALO ASSEMBLY HISTORY

2.1 Introduction

The cold dark matter (CDM) paradigm has become the standard framework for the formation of large-scale structure and galaxies. Small fluctuations in the initial density field grow by means of gravitational instability until they collapse to form virialized dark matter halos. This growth process is hierarchical in the sense that small clumps virialize first, and aggregate successively into larger and larger objects. Galaxies form from the gas that is shock heated by the gravitational collapse and then subsequently cools [see White & Rees (1978); but see also Birnboim et al. (2003); Keres et al. (2004)]. Therefore, a proper understanding of galaxy formation relies on an accurate description of the structure and assembly of these dark matter halos.

This problem is tackled by a combination of both N-body simulations and analytical models. Although N-body simulations have the advantage that they follow the formation of dark matter halos into the non-linear regime, they are expensive, both in terms of labor (analyzing the simulations) and CPU time. Therefore, accurate analytical models are always useful. The most developed of these is the Press-Schechter (PS) formalism, which allows one to compute the (unconditional) halo mass function (Press & Schechter, 1974). Bond et al. (1991), Bower (1991), Lacey & Cole (1993) extended the PS formalism, using the excursion set approach, to compute conditional mass functions. These allow the construction of merger histories, the computation of halo formation times, and detailed studies of spatial clustering and large scale bias (e.g. Kauffmann & White, 1993; Mo & White, 1996; Mo, Jing &

White, 1997; Catelan et al., 1998; Sheth, 1998; Nusser & Sheth, 1999; Somerville & Kolatt, 1999; Cohn et al., 2001).

Numerous studies in the past have tested the predictions of extended Press-Schechter (EPS) theory against numerical simulations. Although the unconditional mass function was found to be in reasonable agreement, it systematically over (under) predicts the number of low (high) mass halos (e.g. Jain & Bertschinger, 1994; Torman, 1998; Gross et al., 1998; Governato et al., 1999; Jenkins et al., 2001). Similar discrepancies have been found regarding the conditional mass function (Sheth & Torman, 1999; Somerville et al., 2000), which results in systematic offsets of the halo formation times predicted by EPS (e.g., van den Bosch, 2002a). Finally, Bond et al. (1991) have shown that the PS approach achieves a very poor agreement on an object-by-object basis when compared with simulations (for a review, see Monaco et al., 1998).

It is generally understood that these discrepancies stem from the assumption of spherical collapse. Numerous studies have investigated schemes to improve the EPS formalism by using ellipsoidal, rather than spherical collapse conditions, thereby taking proper account of the aspherical nature of collapse in a CDM density field [Sheth, Mo & Torman (2001, hereafter SMT01); see also Sheth & Torman (2002); Chiueh et al. (2001); Lin et al. (2002)]. Although this results in unconditional mass functions that are in much better agreement with numerical simulations (e.g., Sheth, Mo & Torman, 2001; Jenkins et al., 2001), they have been unable thus far to yield conditional mass functions of sufficient accuracy that reliable merger trees can be constructed.

Despite its systematic errors and uncertainties, the PS formalism has remained the standard analytical approach in galaxy formation modeling. In particular, the extended Press-Schechter theory is used extensively to compute merger histories and mass assembly histories (hereafter MAHs) which serve as the back-bone for models

of galaxy formation (Kauffmann et al., 1993; Somerville & Primack, 1999; Cole et al., 2000; van den Bosch, 2001; Firmani et al., 2000). This may have profound implications for the accuracy of these models. For instance, the mass assembly histories of dark matter halos are expected to impact on the star formation histories of the galaxies that form inside these halos. In addition, the merger and mass assembly history of individual halos may also be tightly related to their internal structure. As shown by Wechsler et al. (2002, hereafter W02 in this Chapter) and Zhao et al. (2003a,b), the MAH is directly related to the concentration of the resulting dark matter halo (see also Navarro, Frenk & White, 1997; Bullock et al., 2001b; Eke, Navarro & Steinmetz, 2001). Errors in the mass assembly histories of dark matter halos may therefore result in erroneous predictions regarding the star formation history and the rotation curve shapes and/or the zero-point of the Tully-Fisher relation (e.g. Alam et al., 2002; Zentner & Bullock, 2002; Mo & Mao, 2000; van den Bosch, Mo & Yang, 2003b). Clearly, a detailed understanding of galaxy formation requires a description of the growth history of dark matter halos that is more accurate than EPS. Although N-body simulations are probably the most reliable means of obtaining accurate assembly histories of dark matter halos, they are computationally too expensive.

As an alternative to the EPS formalism and N-body simulations, perturbative techniques have been developed that describe the growth of dark matter halos in a given numerical realization of a linear density field. These include, amongst others, the truncated Zel'Dovich (1970) approximation (Borgani, Coles & Moscardini, 1994), the peak-patch algorithm (Bond & Myers, 1996a,b) and the merging cell model (Rodrigues & Thomas, 1996; Lanzoni, Mamon & Guiderdoni, 2000). Recently, Monaco et al. (2002b) developed a numerical code that uses local ellipsoidal collapse approximations (Bond & Myers, 1996a; Monaco, 1995) within Lagrangian Perturbation Theory (LPT Buchert & Ehlers, 1993; Catelan, 1995). This code, called PINOCCHIO (PINpointing Orbit-Crossing Collapsed HIerarchical Objects), has been shown

to yield accurate mass functions, both conditional and unconditional (Monaco et al., 2002a,b; Taffoni et al., 2002), and is therefore ideally suited to study halo assembly histories, without having to rely on computationally expensive N-body simulations.

This Chapter is organized as follows. In Section 2.2 we give a detailed overview of (extended) Press-Schechter theory, including a discussion of its short-comings and its modifications under ellipsoidal collapse conditions, and describe the Lagrangian perturbation code PINOCCHIO . In Section 2.3 we compare the MAHs obtained from PINOCCHIO , the EPS formalism, and N-body simulations. We show that PINOCCHIO yields MAHs that are in excellent agreement with numerical simulations, and do not suffer from the shortcomings of the EPS formalism. In the second part of this Chapter we then analyze a large, statistical sample of MAHs obtained with PINOCCHIO for halos spanning a wide range in masses. In Section 2.5 we use these MAHs to study, in a statistical sense, various characteristic epochs and events in the mass assembly history of a typical CDM halo. We analyze the statistics of major merger events in Section 2.6. Finally, Section 2.9 summarizes our results.

2.2 Theoretical background

2.2.1 Extended Press-Schechter theory

In the standard model for structure formation the initial density contrast $\delta(\mathbf{x}) = \rho(\mathbf{x})/\bar{\rho} - 1$ is considered to be a Gaussian random field, which is therefore completely specified by the power spectrum $P(k)$. As long as $\delta \ll 1$ the growth of the perturbations is linear and $\delta(\mathbf{x}, t_2) = \delta(\mathbf{x}, t_1)D(t_2)/D(t_1)$, where $D(t)$ is the linear growth factor linearly extrapolated to the present time. Once $\delta(\mathbf{x})$ exceeds a critical threshold $\delta^0_{\rm crit}$ the perturbation starts to collapse to form a virialized object (halo). In the case of spherical collapse $\delta^0_{\rm crit} \simeq 1.68$. In what follows we define δ_0 as the initial density contrast field linearly extrapolated to the present time. In terms of δ_0, regions that

have collapsed to form virialized objects at redshift z are then associated with those regions for which $\delta_0 > \delta_c(z) \equiv \delta^0_{\rm crit}/D(z)$.

In order to assign masses to these collapsed regions, the PS formalism considers the density contrast δ_0 smoothed with a spatial window function (filter) $W(r; R_f)$. Here R_f is a characteristic size of the filter, which is used to compute a halo mass $M = \gamma_f \bar{\rho} R_f^3/3$, with $\bar{\rho}$ the mean mass density of the Universe and γ_f a geometrical factor that depends on the particular choice of filter. The *ansatz* of the PS formalism is that the fraction of mass that at redshift z is contained in halos with masses greater than M is equal to two times the probability that the density contrast smoothed with $W(r; R_f)$ exceeds $\delta_c(z)$. This results in the well known PS mass function for the co-moving number density of halos:

$$\frac{{\rm d}n}{{\rm d}\ln M}(M, z)\,{\rm d}M = \sqrt{\frac{2}{\pi}}\,\bar{\rho}\,\frac{\delta_c(z)}{\sigma^2(M)}\,\left|\frac{{\rm d}\sigma}{{\rm d}M}\right|\,\exp\left[-\frac{\delta_c^2(z)}{2\sigma^2(M)}\right]\,{\rm d}M \tag{2.1}$$

(Press & Schechter, 1974). Here $\sigma^2(M)$ is the mass variance of the smoothed density field given by

$$\sigma^2(M) = \frac{1}{2\pi^2}\int_0^\infty P(k)\,\widehat{W}^2(k; R_f)\,k^2\,{\rm d}k. \tag{2.2}$$

with $\widehat{W}(k; R_f)$ the Fourier transform of $W(r; R_f)$.

The *extended* Press-Schechter (EPS) model developed by Bond et al. (1991), is based on the excursion set formalism. For each point one constructs 'trajectories' $\delta(M)$ of the linear density contrast at that position as function of the smoothing mass M. In what follows we adopt the notation of Lacey & Cole (1993) and use the variables $S = \sigma^2(M)$ and $\omega = \delta_c(z)$ to label mass and redshift, respectively. In the limit $R_f \to \infty$ one has that $S = \delta(S) = 0$, which can be considered the starting point of the trajectories. Increasing S corresponds to decreasing the filter mass M, and $\delta(S)$ starts to wander away from zero, executing a random walk (if the filter is a sharp k-space filter). The fraction of matter in collapsed objects in the mass interval

M, $M + \mathrm{d}M$ at redshift z is now associated with the fraction of trajectories that have their *first upcrossing* through the barrier $\omega = \delta_c(z)$ in the interval S, $S + \mathrm{d}S$, which is given by

$$P(S, \omega)\, \mathrm{d}S = \frac{1}{\sqrt{2\pi}}\, \frac{\omega}{S^{3/2}}\, \exp\left[-\frac{\omega^2}{2S}\right]\, \mathrm{d}S \tag{2.3}$$

(Bond et al., 1991; Bower, 1991; Lacey & Cole, 1993). After conversion to number counting, this probability function yields the PS mass function of equation (2.1). Note that this approach does not suffer from the arbitrary factor two in the original Press & Schechter approach.

Since for random walks the upcrossing probabilities are independent of the path taken (i.e., the upcrossing is a Markov process), the probability for a change ΔS in a time step $\Delta\omega$ is simply given by equation (2.3) with S and ω replaced with ΔS and $\Delta\omega$, respectively. This allows one to immediate write down the *conditional* probability that a particle in a halo of mass M_2 at z_2 was embedded in a halo of mass M_1 at z_1 (with $z_1 > z_2$) as

$$P(S_1, \omega_1 | S_2, \omega_2)\, \mathrm{d}S_1 = \frac{1}{\sqrt{2\pi}}\, \frac{(\omega_1 - \omega_2)}{(S_1 - S_2)^{3/2}}\, \exp\left[-\frac{(\omega_1 - \omega_2)^2}{2(S_1 - S_2)}\right]\, \mathrm{d}S_1 \tag{2.4}$$

Converting from mass weighting to number weighting, one obtains the average number of progenitors at z_1 in the mass interval M_1, $M_1 + \mathrm{d}M_1$ which by redshift z_2 have merged to form a halo of mass M_2:

$$\frac{\mathrm{d}N}{\mathrm{d}M_1}(M_1, z_1 | M_2, z_2)\, \mathrm{d}M_1 = \frac{M_2}{M_1}\, P(S_1, \omega_1 | S_2, \omega_2)\, \left|\frac{\mathrm{d}S}{\mathrm{d}M}\right|\, \mathrm{d}M_1. \tag{2.5}$$

This conditional mass function can be combined with Monte-Carlo techniques to construct merger histories (also called merger trees) of dark matter halos.

2.2.2 Ellipsoidal collapse

In an attempt to improve the inconsistencies between EPS and numerical simulations (see Section 2.1), various authors have modified the EPS formalism by considering ellipsoidal rather than spherical collapse. For ellipsoidal density perturbations, the conditions for collapse not only depend on the self-gravity of the perturbation, but also on the tidal coupling with the external mass distribution; external shear can actually rip overdensities apart and thus prevent them from collapsing. Since smaller mass perturbations typically experience a stronger shear field, they tend to be more ellipsoidal. Therefore, it is to be expected that the assumptions of spherical collapse in the standard EPS formalism are more accurate for more massive halos, whereas modifications associated with ellipsoidal collapse will be more dramatic for smaller mass halos. The way in which ellipsoidal collapse modifies the halo formation times with respect to the EPS predictions depends on the definition of collapse. Ellipsoidal perturbations collapse independently along the three different directions defined by the eigen vectors of the deformation tensor (defined as the second derivative of the linear gravitational potential). It is customary to associate the first axis collapse with the formation of a 2-dimensional pancake-like structure, the second axis collapse with the formation of a 1-dimensional filament, and the third axis collapse with the formation of a dark matter halo. Most authors indeed have associated halo formation with the collapse of the third axis (e.g. Bond & Myers, 1996a; Audit et al., 1997; Lee et al., 1998; Sheth, Mo & Torman, 2001), though some have considered the first axis collapse instead (Bertschinger et al., 1994; Monaco, 1995). For first-axis collapse one predicts that halos form earlier than in the spherical case, whereas the opposite applies when considering third-axis collapse. Clearly, the implications of considering ellipsoidal rather than spherical collapse depend sensitively on the collapse definition.

In order to incorporate ellipsoidal collapse in a PS-like formalism, one needs to obtain an estimate of the critical overdensity for collapse δ_{ec}. Various studies have

attempted such schemes. For instance, SMT01 used the ellipsoidal collapse model to obtain

$$\delta_{ec}(M,z) = \delta_c(z)\left(1 + 0.47\left[\frac{\sigma^2(M)}{\delta_c^2(z)}\right]^{0.615}\right). \tag{2.6}$$

Here $\delta_c(z)$ is the standard value for the spherical collapse model. Solving for the upcrossing statistics with this particular barrier shape results in halo mass functions that are in excellent agreement with those found in simulations (Sheth & Torman, 1999; Jenkins et al., 2001). Unfortunately, no analytical expression for the conditional mass function is known for a barrier of the form of equation (2.6), and one has to resort to either approximate fitting functions (Sheth & Torman, 2002), or one has to use time-consuming Monte-Carlo simulations to determine the upcrossing statistics (Chiueh et al., 2001; Lin et al., 2002). Although the resulting conditional mass functions $\frac{\mathrm{d}N}{\mathrm{d}M_1}(M_1,z_1|M_2,z_2)\ \mathrm{d}M_1$ have been found to be in good agreement with numerical simulations if a relatively large look-back time is considered (i.e., if $\Delta z = z_2 - z_1 \geq 0.5$), there is still a large disagreement for small Δz. This is probably due to the neglect of correlations between scales in the excursion set approach (Peacock & Heavens, 1999; Sheth & Torman, 2002). This is unfortunate as it does not allow these methods to be used for the construction of merger histories or MAHs. Lin et al. (2002) tried to circumvent this problem by introducing a small mass gap between parent halo and progenitor halo, i.e., each time step they require that $S_1 - S_2 \geq f\,\delta_c^2(z_2)$. Upon testing their conditional mass function with this mass gap against numerical simulations they find good agreement for $f = 0.06$, and claim that with this modification the excursion set approach *can* be used to construct merger histories under ellipsoidal collapse conditions. However, they only tested their conditional mass functions for $\Delta z \geq 0.2$, whereas accurate merger histories require significantly smaller time steps. For instance, van den Bosch (2002a) has argued for timesteps not larger than $\Delta\omega = \omega_1 - \omega_2 \simeq 0.1$, which, for an Einstein-de Sitter (EdS) cosmology, corresponds to $\Delta z \simeq 0.06$ [see also discussion in Somerville & Primack

(1999)]. Furthermore, with the mass gap suggested by Lin et al. (2002), each time step there is a minimum amount of mass accreted by the halo, which follows from $S_1 - S_2 = f\,\delta_c^2(z_2)$. This introduces a distinct maximum to the halo half-mass formation time, the value of which depends sensitively on the actual time-steps taken. To test this, we constructed MAHs of CDM halos using the method of van den Bosch (2002a) but adopting the conditional probability function of Lin et al. (2002). This resulted in MAHs that are in very poor agreement with numerical simulations. In particular, the results were found to depend strongly on the value of $\Delta\omega$ adopted.

In summary, although introducing ellipsoidal collapse conditions in the excursion set formalism has allowed the construction of accurate unconditional mass functions, there still is no reliable method based on the EPS formalism that allows the construction of accurate merger histories and/or MAHs.

2.2.3 PINOCCHIO

Although the problem of obtaining accurate merging histories under ellipsoidal collapse conditions can be circumvented by using N-body simulations, the time-expense of these simulations is a major hurdle. An attractive alternative is provided by the LPT code PINOCCHIO developed recently by Monaco et al. (2002b). Below we give a short overview of PINOCCHIO , and we refer the interested reader to Monaco et al. (2002a,b) and Taffoni et al. (2002) for a more elaborate description.

PINOCCHIO uses Lagrangian perturbation theory to describe the dynamics of gravitational collapse. In LPT the co-moving (Eulerian) coordinate $\mathbf{x}$ and the initial Lagrangian coordinate $\mathbf{q}$ of each particle are connected via

$$\mathbf{x}(\mathbf{q}, t) = \mathbf{q} + \mathbf{S}(\mathbf{q}, t), \tag{2.7}$$

with $\mathbf{S}$ the displacement field. The first-order term of $\mathbf{S}(\mathbf{q}, t)$ is the well-known Zel'dovich approximation (Zel'Dovich, 1970):

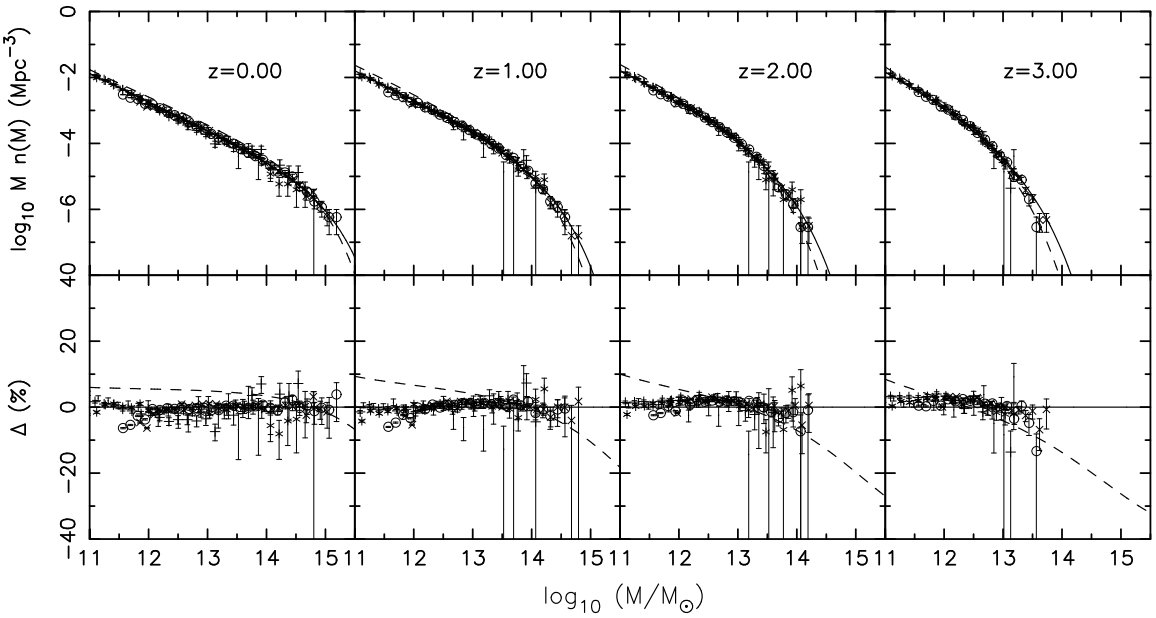

Figure 2.1. Panels in the upper row show the (unconditional) halo mass functions at 4 different redshifts, as indicated. Different symbols (each with Poissonian error bars) correspond to 5 different PINOCCHIO simulations randomly selected from P0, each with a different mass resolution. Dashed and solid lines correspond to the PS and SMT01 mass functions, respectively, and are shown for comparison. Panels in the lower row show the percentual difference between the PS and SMT01 mass functions (dashed lines) and that between the PINOCCHIO and the SMT01 mass functions (symbols with errorbars). Clearly, the PS mass function overestimates (underestimates) the number of small (high) mass halos, while PINOCCHIO yields mass functions that are in excellent agreement with SMT01 (and thus with N-body simulations).

$$\mathbf{S}(\mathbf{q},t) = -D(t)\frac{\partial \psi}{\partial \mathbf{q}} \tag{2.8}$$

with $\psi(\mathbf{q})$ the rescaled linear gravitational potential, which is related to the density contrast $\delta_0(\mathbf{q})$ extrapolated to the present time by the Poisson equation

$$\nabla^2\psi(\mathbf{q}) = \delta_0(\mathbf{q}), \tag{2.9}$$

Since the Lagrangian density field is basically $\rho_{\rm L}(\mathbf{q}) = \bar{\rho}$, the (Eulerian) density contrast is given by

$$1 + \delta(\mathbf{x}, t) = \frac{1}{\det(J)} \tag{2.10}$$

with $J = \partial\mathbf{x}/\partial\mathbf{q}$ the Jacobian of the transformation given in (2.7). Note that the density formally goes to infinity when the Jacobian determinant vanishes, which corresponds to the point in time when the mapping $\mathbf{q} \rightarrow \mathbf{x}$ becomes multi-valued, i.e. when orbits first cross leading to the formation of a caustic. Since the (gravitationally induced) flow is irrotational the matrix J is symmetric and can thus be diagonalized:

$$1 + \delta(\mathbf{x}, t) = \frac{1}{\prod_{i=1}^{3}[1 - D(t)\lambda_i(\mathbf{q})]} \tag{2.11}$$

with $-\lambda_i$ the eigenvalues of the deformation tensor $\partial^2\psi/\partial q_i \partial q_j$.

PINOCCHIO starts by constructing a random realization of a Gaussian density field $\rho(\mathbf{q})$ (linearly extrapolated to $z = 0$) and the corresponding peculiar potential $\phi(\mathbf{q})$ on a cubic grid. The density fluctuation field is specified completely by the power spectrum $P(k)$, which is normalized by specifying the value of σ_8, defined as the r.m.s. linear overdensity at $z = 0$ in spheres of radius $8h^{-1}$ Mpc. The density and peculiar potential fields are subsequently convolved with a series of Gaussians with different values for their FWHM R. For the 256^3 simulations used in this work, 26 different linearly sampled values of R are used. For a given value of R the density of a mass element (i.e., 'particle') will become infinite as soon as at least one of the ellipsoid's axes reaches zero size (i.e., when $D(t) = 1/\lambda_i$). At this point orbit crossing (OC) occurs and the mass element enters a high-density multi-stream region. This is the moment of first-axis collapse. Since the Jacobian determinant becomes multivalued at this stage, one can not make any further predictions of the mass element's fate beyond this point in time. Consequently, it is not possible in PINOCCHIO to associate halo collapse with that of the third axis.

For each Lagrangian point $\mathbf{q}$ (hereafter 'particle') and for each smoothing radius R this OC (i.e., collapse) time is computed, and the highest collapse redshift z_c,

the corresponding smoothing scale R_c, and the Zel'dovich estimate of the peculiar velocity $\mathbf{v}_c$ are recorded. PINOCCHIO differs from the standard PS-like method when it comes to assigning masses to collapsed objects. Rather than associating a halo mass with the collapsed mass element based directly on the smoothing scale R_c at collapse, PINOCCHIO uses a fragmentation algorithm to link neighboring mass elements into a common dark matter halo. In fact, the collapsed mass element may be assigned to a filament or sheet rather than a halo.

After sorting particles according to decreasing collapse redshift z_c the following rules for accretion and merging are adopted: Whenever a particle collapses and non of its Lagrangian neighbors (the six nearest particles) have yet collapsed, the particle is considered a seed for a new halo. Otherwise, the particle is accreted by the nearest Lagrangian neighbor that already has collapsed if the Eulerian distance d, computed using the Zel'dovich velocities $\mathbf{v}$ at the time of collapse, obeys $d \leq f_a R_M$, where $R_M = M^{1/3}$ is the radius of a halo of M particles. If more than one Lagrangian neighbor has already collapsed, it is simultaneously checked whether these halos merge. This occurs whenever, again at the time of collapse, the mutual Eulerian distance between these halos is $d \leq f_M R_M$, where R_M refers to the larger halo. Note that with this description, up to six halos may merge at a given time. The collapsing particles that according to these criteria do not accrete onto a halo at their collapse time are assigned to a filament. In order to mimic the accretion of filaments onto halos, filament particles can be accreted by a dark matter halo at a later stage when they neighbor (in Lagrangian space) an accreting particle. Finally, in high density regions it can happen that pairs of halos that are able to merge are not touched by newly collapsing particles for a long time. Therefore, at certain time intervals pairs of touching halos are merged if they obey the above merging condition.

The accretion and merging algorithm described above has five free parameters. In addition to the parameters f_a and f_M three additional free parameters have been

Table 2.1. Ensemble of PINOCCHIO simulations (P0)

Box size (h^{-1} Mpc)	$N_{\rm run}$	M_p ($h^{-1}\,{\rm M}_\odot$)	$N_{\rm MAH}$
20	12	4.0×10^7	2,690
40	8	3.2×10^8	1,863
60	8	1.1×10^9	796
80	6	2.5×10^9	1,438
100	6	5.0×10^9	2,799
140	4	1.4×10^{10}	410
160	2	2.0×10^{10}	299
200	9	4.0×10^{10}	2,629

A listing of the PINOCCHIO simulations used in this Chapter. All simulations use 256^3 particles and adopt the standard ΛCDM concordance cosmology. In order to get good statistics, we choose a combination of box sizes so that we can select thousands of well-resolved (with more than 2000 particles) halos in each mass bin we adopt in the work. This ensemble of PINOCCHIO simulations is referred to as 'P0' in the text. The first column of Table 1 lists the box size of the simulation in $h^{-1}\,$Mpc. The second column lists the number of independent realizations run. The particle mass M_p (in $h^{-1}\,{\rm M}_\odot$) is listed in the third column, while the fourth column lists the total number of halos (summed over all $N_{\rm run}$ realizations) with more than 2000 particles and for which a MAH has been obtained.

introduced by Monaco et al. (2002b). We refer the reader to this paper for details. This relatively large amount of freedom may seem a weakness of PINOCCHIO . However, it is important to realize that even N-body codes require some free parameters, such as the linking-length in the Friends-Of-Friends (FOF) algorithm used to identify dark matter halos. Furthermore, we do not consider these parameters as free in what follows. Rather, we adopt the values advocated by Monaco et al. (2002a,b), which they obtained by tuning PINOCCHIO to reproduce the conditional and unconditional mass function of N-body simulations.

2.3 Simulations

In this Chapter we use PINOCCHIO simulations to study the mass assembly histories (MAHs) of dark matter halos. We follow previous studies (Lacey & Cole, 1993; Eisenstein & Loeb, 1996; Nusser & Sheth, 1999; van den Bosch, 2002a) and

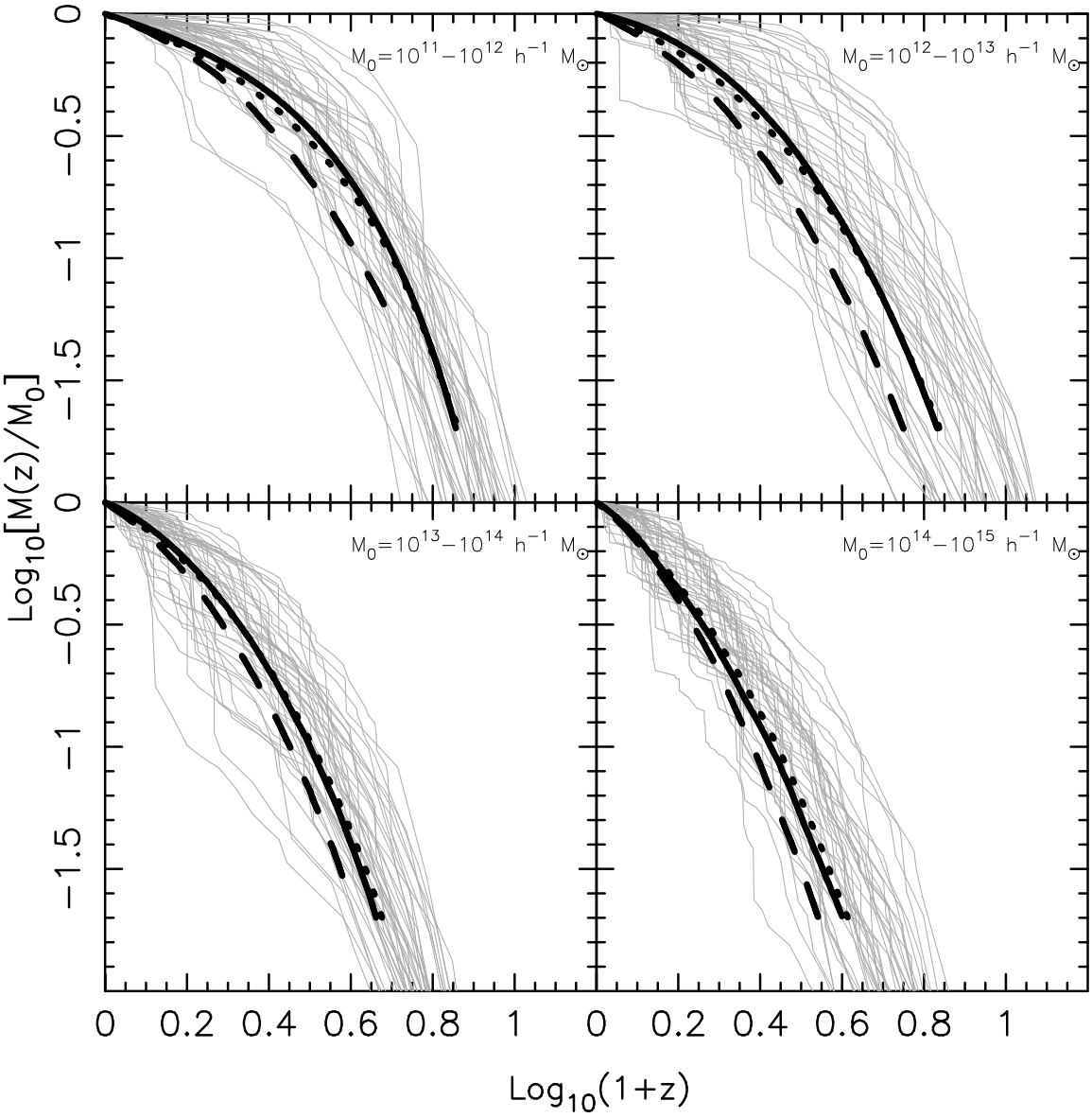

Figure 2.2. The mass assembly histories of dark matter halos with present-day masses in the four mass bins as indicated in the panels. The upper two panels are based on the $100h^{-1}$Mpc-box simulations, P1 and S1, while the lower two panels use data from the $300h^{-1}$Mpc-box simulations, P2 and S2. The thin lines are 40 MAHs randomly selected from the PINOCCHIO simulations. The thick solid line in each panel shows the average of all the MAHs obtained in the PINOCCHIO simulations in the corresponding mass bin. The thick dotted line shows the average MAH extracted from the simulations. The thick dashed line shows the average MAH obtained from 3000 EPS realizations (properly sampled from halo mass function).

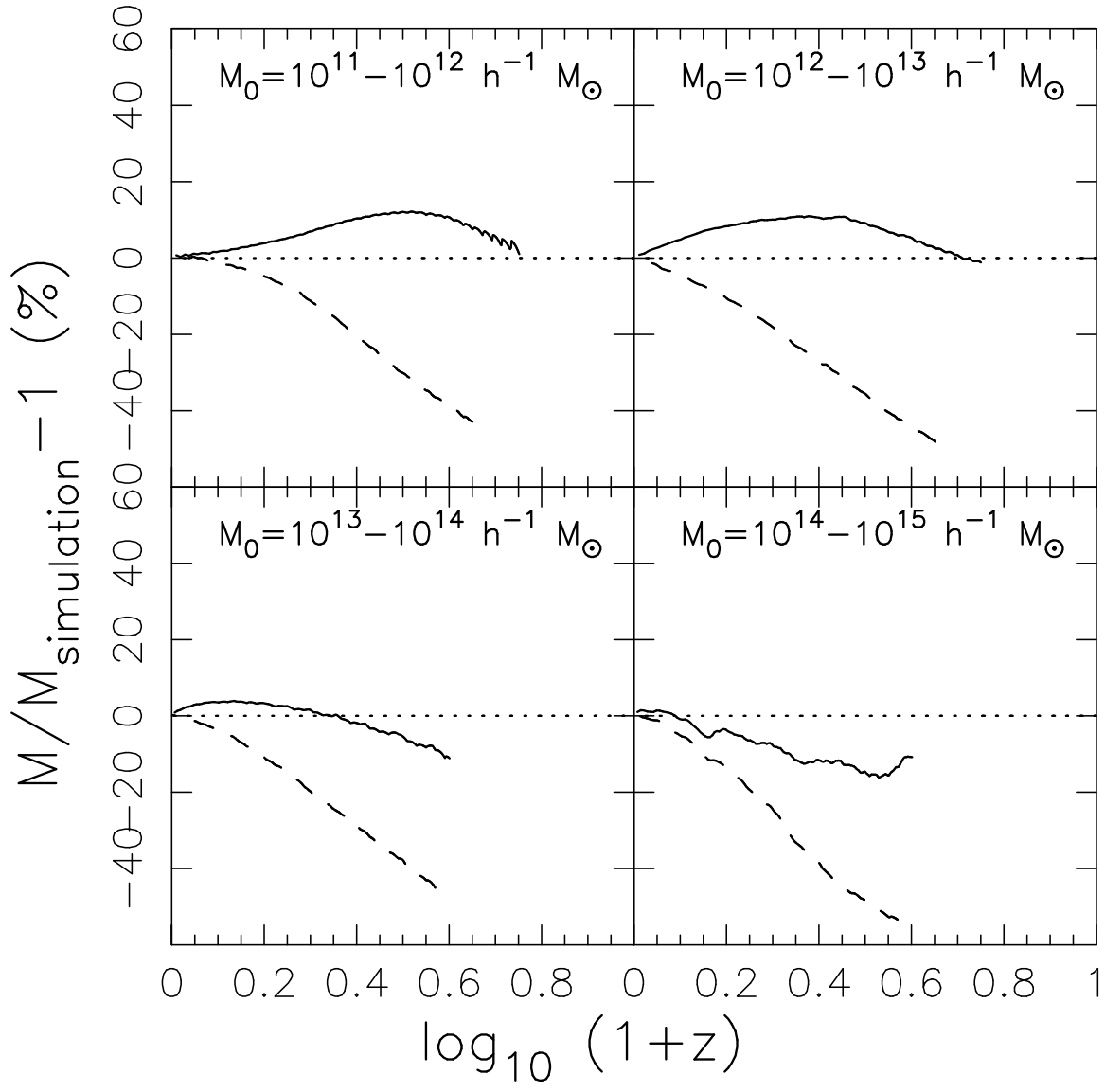

Figure 2.3. Difference between halo MAHs predicted by N-body simulation, EPS, and PINOCCHIO . The dashed curve in each panel shows the difference between the average MAHs predicted by the EPS model and by the N-body simulation, while the solid curve shows the difference between PINOCCHIO prediction and N-body simulation. The upper two panels use data from P1 and S1, while the lower two panels use data from P2 and S2. Data are not shown for $z \gtrsim 3$ because the MAHs are not well represented at such high redshifts in the simulations.

define the MAH, $M(z)$, of a halo as the main trunk of its merger tree: at each redshift, the mass $M(z)$ is associated with the mass of the most massive progenitor

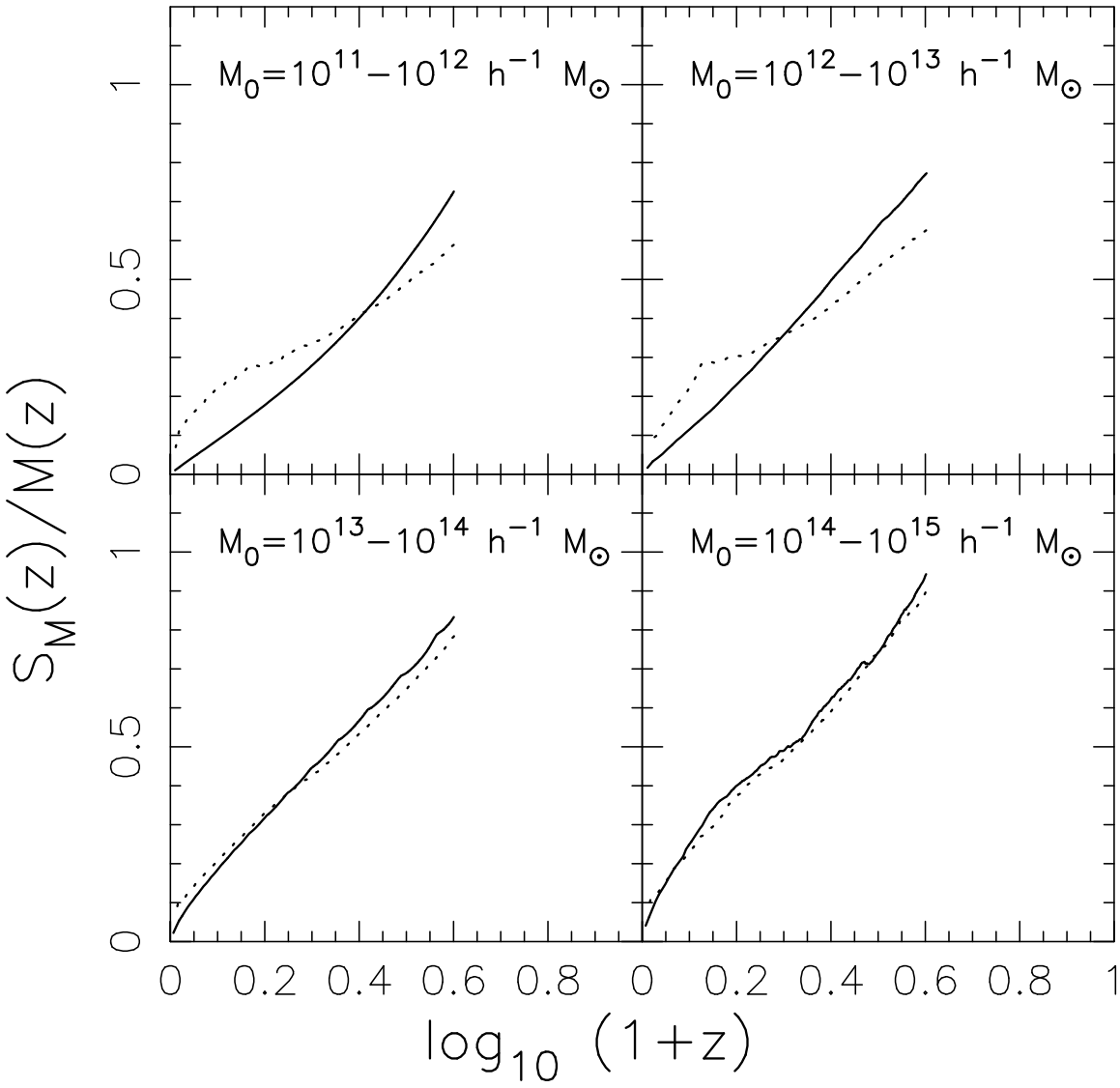

Figure 2.4. The *standard deviation* of the MAHs, $S_{\rm M}(z)$, normalized by the average MAH, $M(z)$, in four mass bins. Solid lines are results from PINOCCHIO , while dotted lines are results from N-body simulations. As in Fig. 2.2 and Fig. 2.3, the upper two panels use data from P1 and S1, while the lower two panels use data from P2 and S2.

at this redshift, and we follow this progenitor, and this progenitor only, further back in time. In this way, this 'main progenitor halo' never accretes other halos that are more massive than itself. Note that although at each branching point we follow the most massive branch, this does not necessarily imply that the main progenitor is also the most massive of *all* progenitors at any given redshift.

Below we describe the PINOCCHIO simulations, the N-body simulations, and the EPS method used to construct MAHs.

2.3.1 PINOCCHIO simulations

Because the progenitors of a present-day halo become smaller at higher redshift, we can only follow the MAHs to a sufficiently high redshift if the halo at $z = 0$ contains a large enough number of particles. When constructing MAHs with PINOCCHIO , we only use halos that contain more than 2000 particles at the present time, and we trace each MAH to the redshift at which its main progenitor contains less than 10 particles. In order to cover a large range of halo masses, we have carried out 55 PINOCCHIO simulations with 256^3 particles each and spanning a wide range of box sizes and particle masses (see Table 1, we call this suite of PINOCCHIO simulations P0 hereafter). The choice of box sizes ensures that there are several thousand well-resolved halos in each of the mass bins considered. Each of these simulations takes only about 6 hours of CPU time on a common PC (including the actual analysis), clearly demonstrating its advantage over regular N-body simulations. This suite of PINOCCHIO simulations has adopted the ΛCDM concordance cosmology with $\Omega_m = 0.3$, $\Omega_\Lambda = 0.7$, $h = 0.7$ and $\sigma_8 = 0.9$.

With simulation box sizes ranging from $20\,h^{-1}$Mpc to $200\,h^{-1}$Mpc, and particle masses ranging from $4\times10^7 h^{-1}\,\mathrm{M}_\odot$ to $4\times10^{10} h^{-1}\,\mathrm{M}_\odot$, we are able to study the MAHs of present-day halos with masses $> 8\times10^{10} h^{-1}\,\mathrm{M}_\odot$. The construction of the MAHs is straightforward: PINOCCHIO outputs a halo mass every time a merger occurs, i.e., when a halo with more than 10 particles merges into the main branch. If we require an estimate of the halo mass at any intermediate redshift, z, we use linear interpolation in $\log(1 + z)$ between the two adjacent output redshifts.

2.3.2 N-body simulations

For comparison we also used MAHs extracted from two sets of N-body simulations (referred to as S1 and S2). These N-body simulations follow the evolution of 512^3 particles in a periodic box of $100\,h^{-1}$Mpc (S1) and $300\,h^{-1}$Mpc (S2) on a side, assuming slightly different cosmologies (see Table 2 for details). The simulations were carried out with the publicly available code GADGET-2. The snapshot outputs of each simulation are evenly placed at 60 redshifts between $z = 0$ and $z = 15$ in $\ln(1 + z)$ space.

In each simulation and at each output, halos are identified using the standard FOF algorithm with a linking length of $b = 0.2$. Halos obtained with this linking length have a mean overdensity of ~ 180. A halo at redshift z_1 is identified as a progenitor of a halo at $z_2 < z_1$ if more than half of its mass is included in the halo at z_2. For each halo identified at $z = 0$, we trace its most massive progenitor at the next higher snapshot, and then repeatedly perform this procedure on the selected progenitor to the next higher snapshot until the mass of the progenitor reaches the resolution limit of the simulations. The chronologically linked progenitors are referred to as the "main branch" of the dark halo and used to construct the MAHs. In our analysis, we only use halos more massive than $10^{11}h^{-1}\,\mathrm{M}_\odot$ at the present time in S1 and halos more massive than $10^{13}h^{-1}\,\mathrm{M}_\odot$ in S2. Thus, in each simulation only halos with more than ~ 600 particles at $z = 0$ are used, which allows us to trace the MAHs to sufficiently high redshift with sufficiently high resolution. For comparison, we also generate two sets of PINOCCHIO simulations, P1 and P2, using exactly the same numbers of particles and cosmologies as in S1 and S2, respectively (see Table 2).

2.3.3 Monte-Carlo simulations

We also generate MAHs using Monte-Carlo simulations based on the standard EPS formalism. We adopt the N-branch tree method with accretion suggested by Somerville

& Kolatt (1999, hereafter Sk99). This method yields more reliable MAHs than for example the binary-tree method of Lacey & Cole (1993). In particular, it ensures exact mass conservation, and yields conditional mass functions that are in good agreement with direct predictions from EPS theory (i.e., the method is self-consistent).

To construct a merger tree for a parent halo of mass M the SK99 method works as follows. First a value for ΔS is drawn from the mass-weighted probability function

$$P(\Delta S, \Delta\omega)\,\mathrm{d}\Delta S = \frac{1}{\sqrt{2\pi}}\,\frac{\Delta\omega}{\Delta S^{3/2}}\,\exp\left[-\frac{(\Delta\omega^2)}{2\Delta S}\right]\,\mathrm{d}\Delta S \qquad (2.12)$$

(cf. equation [2.4]). Here $\Delta\omega$ is a measure for the time step used in the merger tree, and is a free parameter (see below). The progenitor mass, M_p, corresponding to ΔS follows from $\sigma^2(M_p) = \sigma^2(M) + \Delta S$. With each new progenitor it is checked whether the sum of the progenitor masses drawn thus far exceeds the mass of the parent, M. If this is the case the progenitor is rejected and a new progenitor mass is drawn. Any progenitor with $M_p < M_{\rm min}$ is added to the mass component $M_{\rm acc}$ that is considered to be accreted onto the parent in a smooth fashion (i.e., the formation history of these small mass progenitors is not followed further back in time). Here $M_{\rm min}$ is a free parameter that has to be chosen sufficiently small. This procedure is repeated until the total mass left, $M_{\rm left} = M - M_{\rm acc} - \sum M_p$, is less than $M_{\rm min}$. This remaining mass is assigned to $M_{\rm acc}$ and one moves on to the next time step. For the construction of MAHs, however, it is not necessary to construct an entire set of progenitors. Rather, at each time step, one can stop once the most massive progenitor drawn thus far is more massive than $M_{\rm left}$. This has the additional advantage that one does not have to define a minimum progenitor mass $M_{\rm min}$ (see van den Bosch, 2002a, for details).

In principle, since the upcrossing of trajectories through a boundary is a Markov process, the statistics of progenitor masses should be independent of the time steps taken. However, the SK99 algorithm is based on the *single* halo probability (equa-

Table 2.2. Reference PINOCCHIO and N-body simulations

Simulation Name	$N_{\rm p}$	Box size (h^{-1} Mpc)	M_p ($h^{-1}\,{\rm M}_\odot$)	$\Omega_{\rm m}$	Ω_Λ	h	σ_8
S1 (N-body)	512^3	100	5.5×10^8	0.268	0.732	0.71	0.85
P1 (PINOCCHIO)	512^3	100	5.5×10^8	0.268	0.732	0.71	0.85
S2 (N-body)	512^3	300	1.3×10^{11}	0.236	0.764	0.73	0.74
P2 (PINOCCHIO)	512^3	300	1.3×10^{11}	0.236	0.764	0.73	0.74

tion [2.12]), which does not contain any information about the *set* of progenitors that make up the mass of M. In fact, mass conservation is enforced 'by hand', by rejecting progenitor masses that overflow the mass budget. As shown in van den Bosch (2002a), this results in a time step dependency, but only for relatively large time steps. For sufficiently small values of $\Delta\omega$ the algorithm outlined above yields accurate and robust results (see also SK99). Throughout this Chapter we adopt a timestep of $\Delta z = 0.05$. Our tests with different values of Δz from 0.01 to 0.05 have shown that this time step is small enough to achieve stable results, that is, when we decrease the time step to $\Delta z = 0.01$, the change in the average MAH is less than 1%.

2.4 Comparison between MAHs generated by different methods

We now compare the MAHs obtained with all three methods discussed above. The upper panels of Fig. 2.1 plot the (unconditional) halo mass functions at four different redshifts, as indicated, obtained from 5 arbitrary PINOCCHIO runs with different box sizes in P0. Dashed lines correspond to the analytical halo mass functions obtained using the standard PS formalism (equation [2.1]), while the solid lines indicate the mass functions of SMT01 based on ellipsoidal collapse. The latter have been shown to accurately match the mass functions obtained from N-body simulations (e.g., Sheth & Torman, 1999, SMT01). The symbols in the lower panels of Fig. 2.1 plot the dif-

ferences between the PINOCCHIO and the SMT01 mass functions, while the dashed lines indicate the differences between the PS and the SMT01 mass functions. Clearly, the PINOCCHIO mass functions are in excellent agreement with those of SMT01, and thus also with those obtained from N-body simulations. In addition, Taffoni et al. (2002) have shown that PINOCCHIO also accurately matches the *conditional* mass functions obtained from numerical simulations. We now investigate whether the actual MAHs obtained from PINOCCHIO are also in good agreement with the numerical simulations.

Fig. 2.2 plots the average MAHs obtained from the PINOCCHIO , N-body and EPS simulations, for halos with the present masses in the following four mass ranges: $\log(M_0/h^{-1}\,\mathrm{M}_\odot)$ =11-12, 12-13, 13-14 and 14-15. For comparison, in each panel we also show 40 randomly selected MAHs from the PINOCCHIO simulations (P1 and P2). To ensure mass resolution, results for the low-mass bins (the two upper panels) are based on simulations with the small box size, i.e. S1 and P1. Results for the high-mass bins (the two lower panels) are based only on simulations with the large-box size (S2 and P2) in order to obtain a large number of massive halos. The thick solid curve in each panel corresponds to the average MAH obtained by averaging over all the halos, in the mass range indicated, found in one of the PINOCCHIO simulations (P1 and P2). The thick dashed lines correspond to the average MAHs obtained from 3000 EPS Monte-Carlo simulations (properly weighted by the halo mass function). The thick dotted lines show the average MAHs obtained from the two N-body simulations (S1 and S2). In Fig. 2.3, a detailed comparison between these results are presented. As can be seen in Fig. 2.3, the average MAHs obtained with PINOCCHIO are in good agreement with those obtained from the N-body simulations (with differences smaller than 10%). Note that there are uncertainties in the identification of dark halos in N-body simulations using the FOF algorithm. Sometimes two physically separated halos can be linked together and identified as one halo if they are bridged by dark

matter particles, which can change the halo mass by 5% on average. The agreement between PINOCCHIO and simulation shown in Fig. 2.3 is probably as good as one can hope for. The EPS model, however, yields MAHs that are systematically offset with respect to those obtained from the N-body simulations: the EPS formalism predicts that halos assemble too late (see also van den Bosch, 2002a; Lin et al., 2003; Wechsler et al., 2002). Fig. 2.4 shows the ratio between the standard deviation of the MAHs, $S_{\rm M}(z)$, and the average MAH $M(z)$, as a function of redshift z. As one can see, the agreement between the PINOCCHIO and N-body simulations is also reasonably good.

In summary, the Lagrangian Perturbation code PINOCCHIO yields halo mass functions (both conditional and unconditional), and mass assembly histories that are all in good agreement with N-body simulations. In particular, it works much better than the standard PS formalism, and yet is much faster to run than numerical simulations. PINOCCHIO therefore provides a unique and fast platform for accurate investigations of the assembly histories of a large, statistical sample of CDM halos.

2.5 Halo formation times

Having demonstrated that the PINOCCHIO MAHs are in good agreement with those obtained from N-body simulations, we now use the suite of 55 PINOCCHIO simulations, P0, listed in Table 1 to investigate the assembly histories of a large sample of halos spanning a wide range in halo masses.

The assembly history of a halo can be parameterized by a formation time (or equivalently formation redshift), which characterizes when the halo assembles. However, since the assembly of a halo is a continuous process, different 'formation times' can be defined, each focusing on a different aspect of the MAH. Here we define and compare the following four formation redshifts:

1. $z_{\rm half}$: This is the redshift at which the halo has assembled half of its final mass. This formation time has been widely used in the literature.

2. $z_{\rm lmm}$: This is redshift at which the halo experiences its last major merger. Unless stated otherwise we define a major merger as one in which the mass ratio between the two progenitors is larger than 1/3. This definition is similar to $z_{\rm jump}$ defined in Cohn & White (2005). Major mergers may have played an important role in transforming galaxies and in regulating star formation in galaxies. Their frequency is therefore important to quantify.

3. $z_{\rm vvir}$: This is the redshift at which the virial velocity of a halo, $V_{\rm v}$, defined as the circular velocity at the virial radius, reaches its current value, V_0, for the first time. Since $V_{\rm v}$ is a measure for the depth of the potential well, $z_{\rm vvir}$ characterizes the formation time of the halo's gravitational potential.

4. $z_{\rm vmax}$: This is the redshift at which the halo's virial velocity reaches its maximum value over the entire MAH. As we show below, the value of $V_{\rm v}$ is expected to increase (decrease) with time, if the time scale for mass accretion is shorter (longer) than the time scale of the Hubble expansion. Therefore, $z_{\rm vmax}$ indicates the time when the MAH transits from a fast accretion phase to a slow accretion phase.

In an N-body simulation one can infer the virial velocity of a halo from its internal structure. In the case of PINOCCHIO simulations, however, no information regarding the density distribution of halos is available. However, we may use the fact that CDM halos always have a particular (redshift and cosmology dependent) overdensity. This allows us to define the virial velocity at redshift z as

$$V_{\rm v}(z) = \sqrt{\frac{GM_{\rm v}}{R_{\rm v}}} = \left[\frac{\Delta_{\rm vir}(z)}{2}\right]^{1/6} \left[M_{\rm v}(z)\, H(z)\right]^{1/3} \tag{2.13}$$

Here $M_{\rm v}$ and $R_{\rm v}$ are the virial mass and virial radius of the halo, respectively, and $H(z)$ is the Hubble parameter. The quantity $\Delta_{\rm vir}(z)$ is the density contrast between the mean density of the halo and the critical density for closure, described by equation (1.16).

As an illustration, Fig. 2.5 plots the MAH, $M(z)/M_0$ (upper panel), and the history of the virial velocity, $V_{\rm v}(z)/V_0$ (lower panel) for a randomly selected halo (with $M_0 = 1.02 \times 10^{13} h^{-1}\,{\rm M}_\odot$). All major merger events are marked by a solid dot plus arrow. The last major merger occurs at $z_{\rm lmm} = 1.60$. The other formation redshifts, $z_{\rm half} = 1.59$, $z_{\rm vvir} = 3.77$, and $z_{\rm vmax} = 1.23$ are marked by an open circle, a cross, and an open triangle, respectively.

Fig. 2.6 plots the correlations between the various formation redshifts, for halos with masses in the range $10^{11} - 10^{12} h^{-1}\,{\rm M}_\odot$. The value of r_s in each panel shows the corresponding Spearman rank-order correlation coefficients. Clearly, there is significant correlation among all the formation redshifts, but the scatter is quite large. This demonstrates that these different formation times characterize different aspects of a given MAH. Unlike simulation which outputs snapshots at arbitrary times, PINOCCHIO only outputs when a merger occurs and the merger is treated as instantaneous. Consequently, some formation times can have exactly the same value in PINOCCHIO simulations. Note that the correlation shown in the lower left panel is quite similar to that obtained by (Cohn & White, 2005) for simulated clusters of galaxies. Note also that typically, $z_{\rm vvir} > z_{\rm half}$ and $z_{\rm vvir} > z_{\rm lmm}$. This shows that halos *in this mass range* established their potential wells before they accreted a major fraction of their mass. The last major merger typically occurred well before $z_{\rm half}$, which indicates that most of that mass has been accreted in a fairly smooth fashion (see also W02 and Zhao et al., 2003a).

Fig. 2.7 shows the distributions of the four formation redshifts defined above. Results are shown for four different mass bins, as indicated. For all four formation

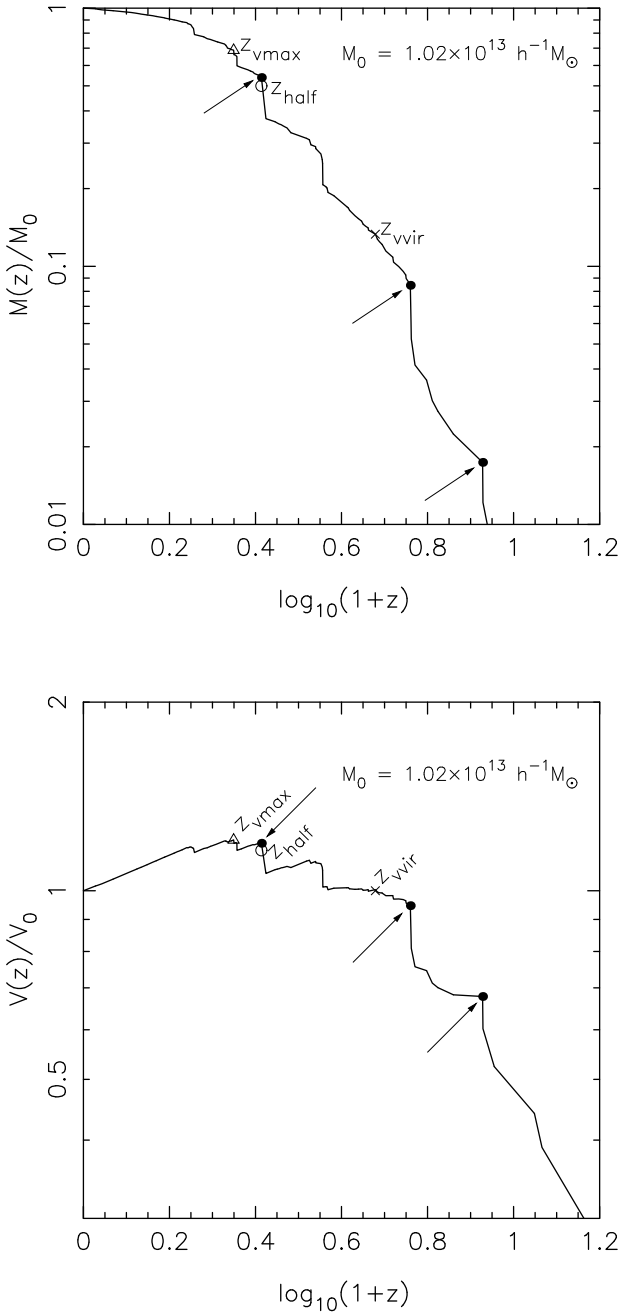

Figure 2.5. *Upper panel:* the MAH of a randomly chosen halo with a mass of $1.02 \times 10^{13} h^{-1}\,\mathrm{M}_{\odot}$. Various characteristic events during the assembly of this halo are indicated: $z_{\rm vmax}$ (open triangle), $z_{\rm half}$ (open circle), and $z_{\rm vvir}$ (cross). The solid dots with an arrow indicate major mergers (those with a mass ratio larger than 1/3). *Lower panel:* same as in upper panel, except that here the evolution of the halo virial velocity is shown.

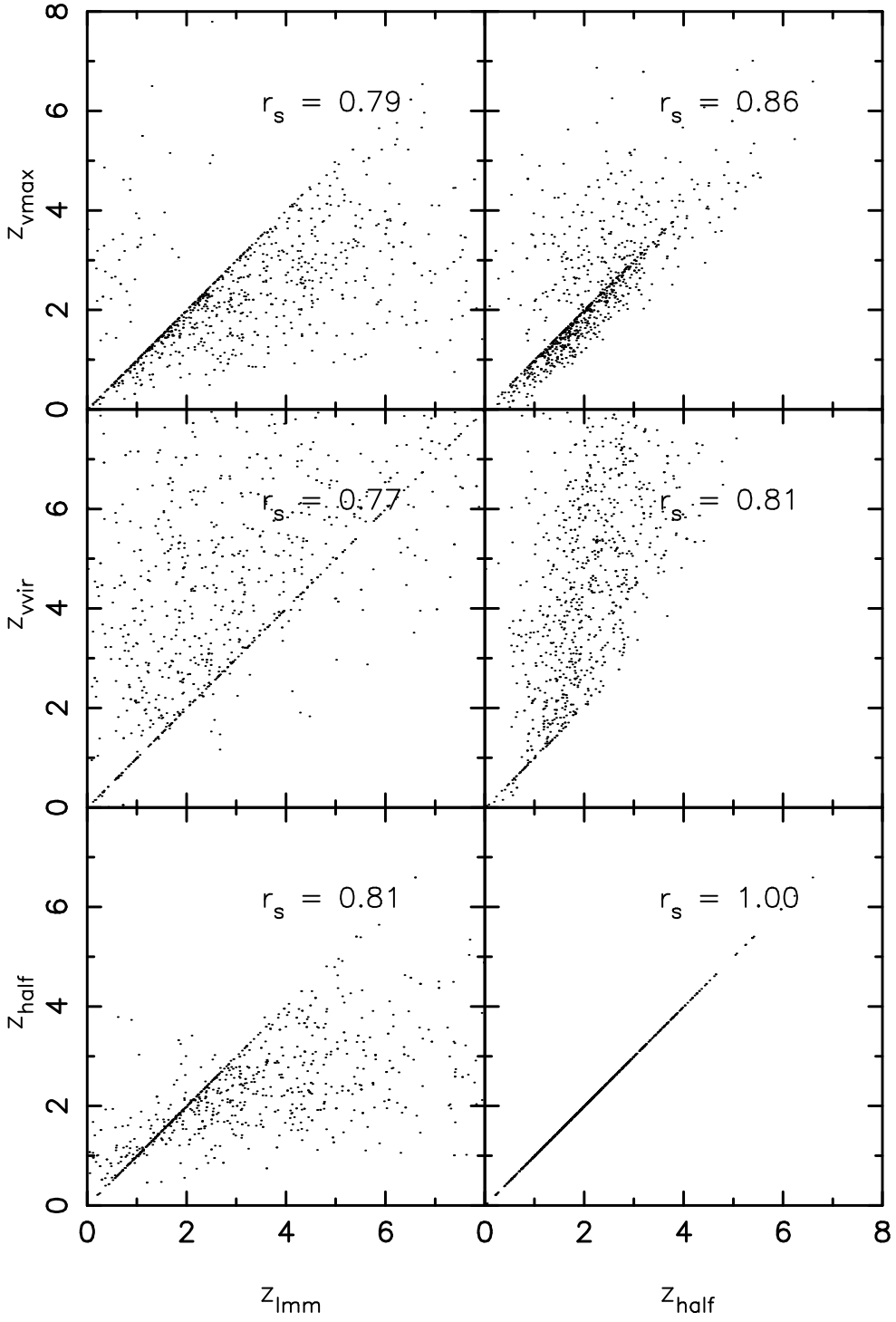

Figure 2.6. The correlations between various halo formation redshifts for halos with present day masses in the range $10^{11}h^{-1}\,\mathrm{M}_\odot \leq M \leq 10^{12}h^{-1}\,\mathrm{M}_\odot$. The value of r_s in each panel shows the corresponding Spearman rank-order correlation coefficient. Due to the finite time resolution in the PINOCCHIO simulations, in some cases the values of two formation times can be the same.

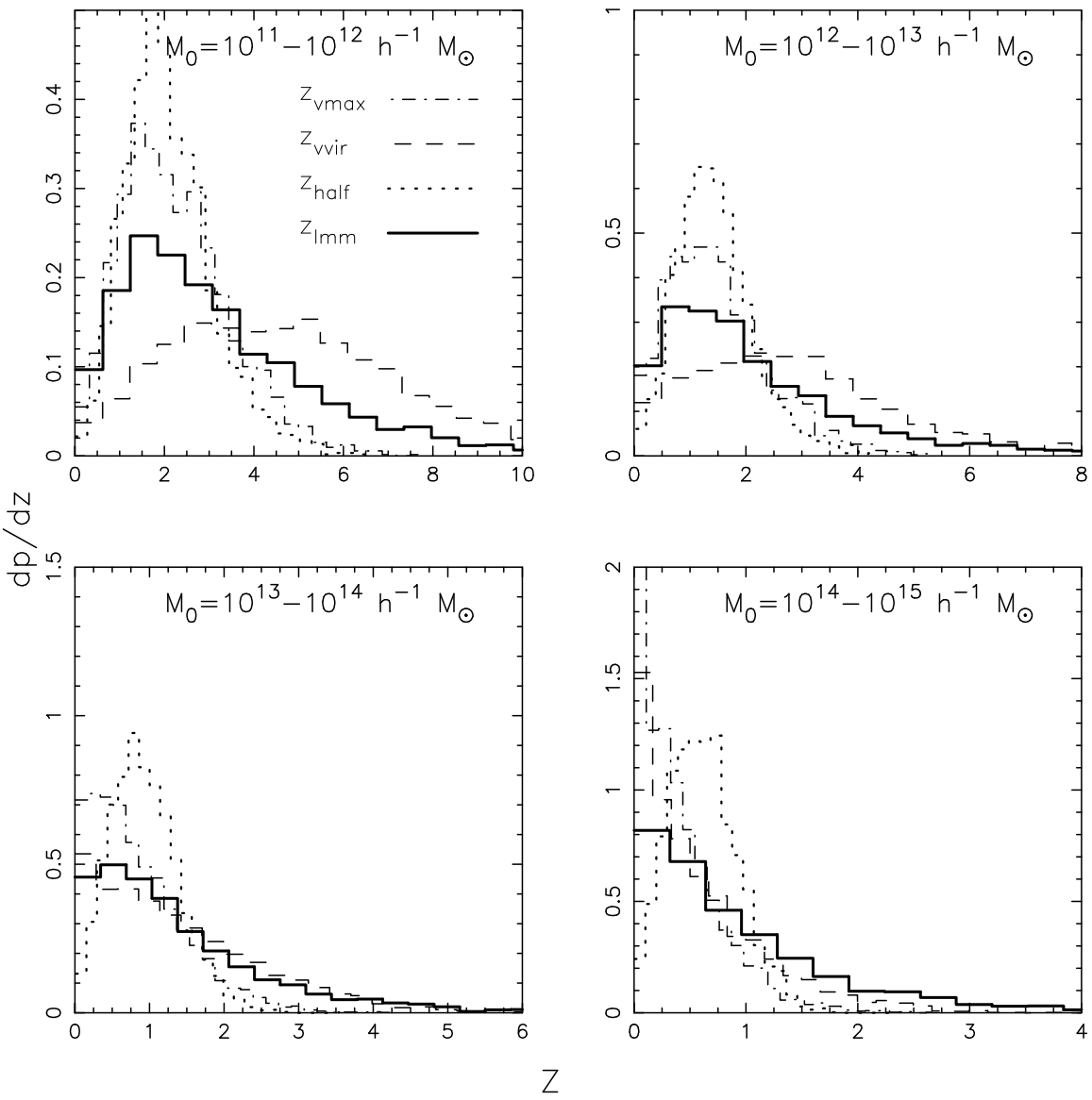

Figure 2.7. The probability distributions of $z_{\rm half}$ (dotted lines), $z_{\rm vvir}$ (dashed lines), $z_{\rm vmax}$ (dot-dashed lines) and $z_{\rm lmm}$ (thick solid lines). Results are shown for four different mass bins, as indicated in each panel. Note that the scale of the four panels is different! See text for a detailed discussion.

redshifts, the median is higher for halos of lower masses. This reflects the hierarchical nature of the assembly of dark matter halos: less massive systems assemble ('form') earlier. Note that the distribution of formation times is also broader for lower mass halos. For halos with $M_0 \geq M_* \simeq 10^{13}h^{-1}\,{\rm M}_\odot$[1], all the distribution functions except

[1]Here M_* is the characteristic non-linear mass defined by $\sigma(M_*) = \delta^0_{\rm crit}$

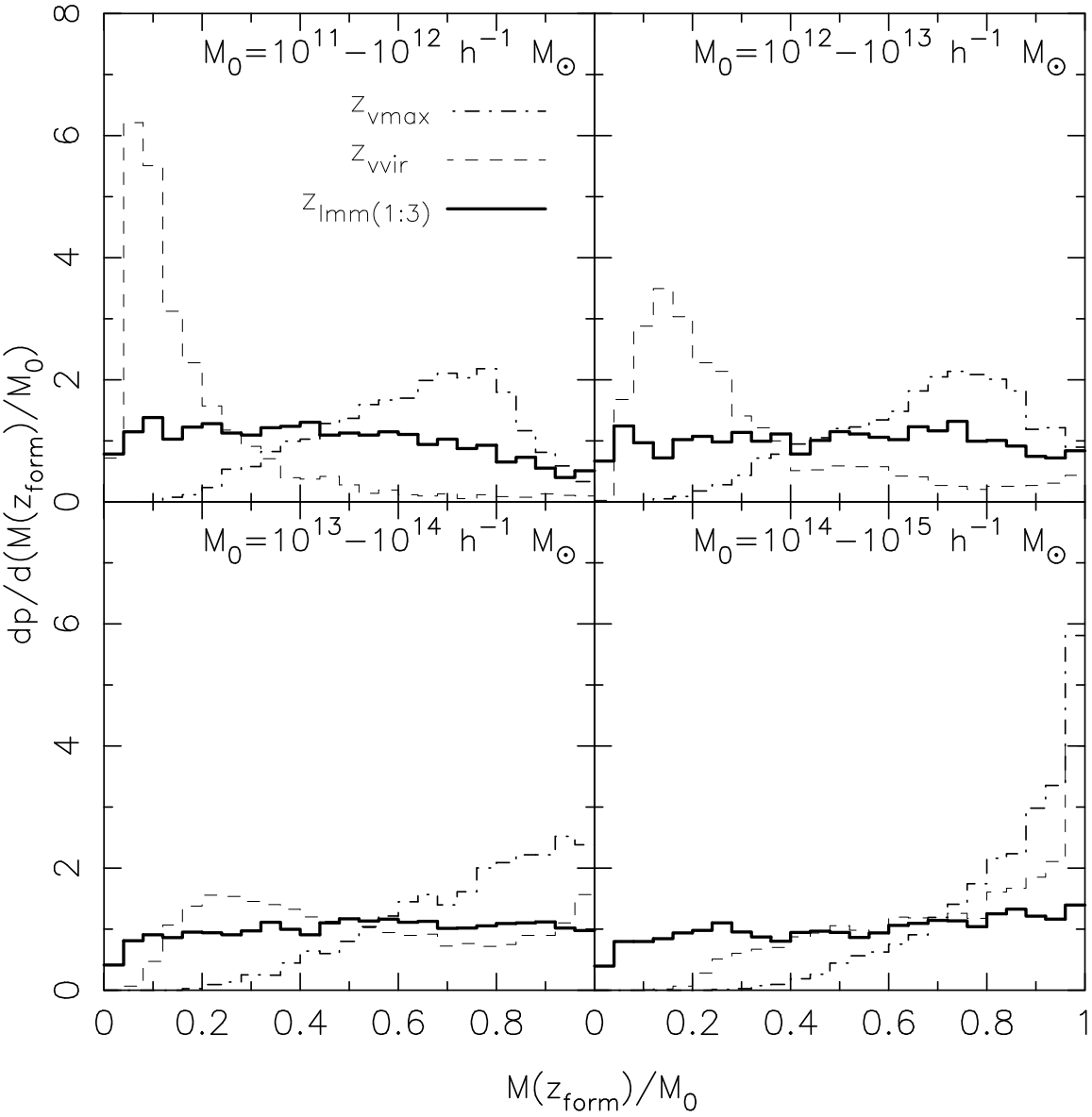

Figure 2.8. The distributions of the halo mass fraction at various formation times. Different line-styles correspond to different definitions of the formation time, as indicated in the upper left-hand panel. As in Fig. 2.7, different panels correspond to different halo mass bins, as indicated.

that of $z_{\rm half}$ are peaked at, or very near to, $z = 0$. This shows that the majority of these halos are still in their fast accretion phase, so that their potential wells are still deepening with time. On the other hand, halos with $M_0 \ll M_*$ typically have $z_{\rm vvir} > z_{\rm half}$ and $z_{\rm vvir} > z_{\rm lmm}$ (cf. Fig. 2.6), indicating that their potential wells have

already been established, despite the fact that they continue to accrete appreciable amounts of mass.

Fig. 2.8 shows the distributions of the ratio $M(z_{\rm form})/M_0$, with $z_{\rm form}$ one of our four formation redshifts. By definition, the distribution of $M(z_{\rm half})/M_0$ is a δ-function at $M(z_{\rm form})/M_0 = 0.5$, and is therefore not shown. For halos with $M_0 < 10^{13}h^{-1}\,{\rm M}_\odot$, the virial velocity has already reached the present day value when the halo has only assembled 10%-20% of its final mass. Thus, these systems assemble most of their mass without significant changes to the depth of their potential well. Only for massive halos with $M_0 \geq 10^{14}h^{-1}\,{\rm M}_\odot$ is the median of $M(z_{\rm vvir})/M_0$ larger than 0.5, implying that they have assembled the majority of their present day mass through major (violent) mergers.

If we define major mergers as those with a progenitor mass ratio that is at least 1/3, the distribution of $M(z_{\rm lmm})/M_0$ is remarkably flat. This implies that some halos accrete a large amount of mass after their last major merger, while for others the last major merger signals the last significant mass accretion event. Remarkably, the distribution of $M(z_{\rm lmm})/M_0$ is virtually independent of M_0. For low mass halos, the flatness of the distribution of $M(z_{\rm lmm})/M_0$ simply reflects the broad distribution of $z_{\rm lmm}$. However, for massive halos with $M \geq M_*$, the distribution of $z_{\rm lmm}$ is fairly narrow. Therefore, for these halos the flatness of the $M(z_{\rm lmm})/M_0$ distribution implies that, since their last major merger, they have accreted a significant amount of mass due to minor mergers. Since the last major merger occurred fairly recently, this is another indication that massive halos are still in their fast accretion phase.

2.6 The properties of major mergers

During the assembly of dark matter halos, major mergers play an important role. Not only does a major merger add a significant amount of mass, it also deepens the halo's potential well. Furthermore, in current models of galaxy formation, a major

merger of two galaxy-sized halos is also expected to result in a merger of their central galaxies, probably triggering a starburst and leading to the formation of an elliptical galaxy. Therefore, it is important to quantify the frequency of major mergers during the formation of CDM halos.

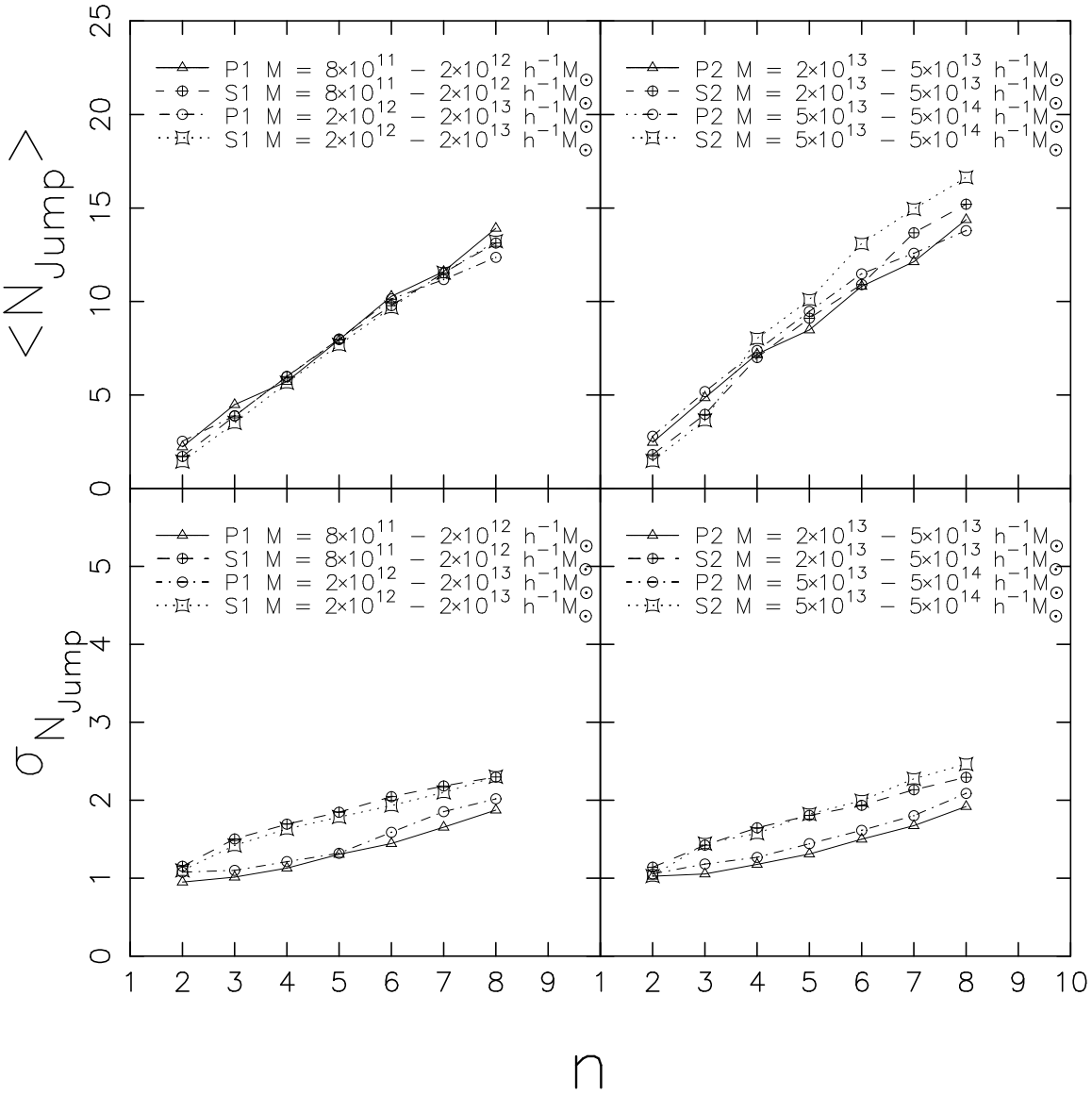

Figure 2.9. The median, $\langle N_{\rm jump}\rangle$, and dispersion, $\sigma_{N_{\rm jump}}$, of the distribution of the number of mass jumps, $N_{\rm jump}$, in the MAHs, versus n (see text for definitions). Left panels show comparison between P1 and S1, while right panels show comparison between P2 and S2. Note that the agreement between the PINOCCHIO simulations and N-body simulations is remarkable and the mass dependence is rather weak.

As mentioned above, in a PINOCCHIO simulation mergers of dark matter halos are treated as instantaneous events, and the masses of the merger progenitors are recorded whenever a merger happens. This makes it very convenient to identify mergers in PINOCCHIO . On the other hand, in an N-body simulation halos are identified only in a number of snapshots, and so the accuracy of identifying mergers is limited by the times intervals of the snapshots. For example, if we define major mergers by looking for halos for which the mass ratio between its second largest and largest progenitors exceeds 1/3 in the last snapshot, we may miss major mergers in which the two progenitors were assembled during the two snapshots. On the other hand, if we identify major mergers in a simulation by looking for halos whose masses increase by a factor between 1/4 and 1 in the next snapshot, we will overestimate the number of major merger events, because some of the halos may have increased their masses by accretion of small halos rather than through major mergers. The simulations used here (S1 and S2), the time intervals between successive snapshots are about 0.3-0.6 Gyr, comparable to the time scales of major mergers, and the two definitions of major mergers described above lead to a factor of 2 difference in the number of major mergers. Because of this, it is difficult to make a direct comparison between PINOCCHIO and N-body simulations in their predictions for the number of major mergers. In order to check the reliability of PINOCCHIO in predicting the number of major mergers, we use quantities that are related to the number of major mergers but yet can be obtained from both our N-body and PINOCCHIO simulations. We first construct PINOCCHIO halos at each of the snapshots of our N-body simulations. We then follow the MAH of each of the present halo using the snapshots and identify the number of events in which the mass of a halo increases by a factor exceeding $1/n$ between two successive snapshots, where n is an integer used to specify the heights of the jumps. In practice, we trace the MAH backward in time until the mass of the halo is 1% of the final halo mass. Since exactly the

same analysis can also be carried out for the N-body simulations, we can compare, for a given n and for halos of given mass at the present time, the statistics of the number of jumps, $N_{\rm jump}$, predicted by PINOCCHIO simulations with that given by the N-body simulations. We found that the distribution of $N_{\rm jump}$ for a given n can be well fit by a Gaussion distribution, and in Fig. 2.9 we plot the median $\langle N_{\rm jump}\rangle$ and standard deviation $\sigma_{N_{\rm jump}}$ versus n, in several mass bins. The agreement between PINOCCHIO and N-body simulations is remarkably good. Although $N_{\rm jump}$ is not exactly the number of major mergers, the good agreement between PINOCCHIO and N-body simulations makes us believe that it is reliable to use PINOCCHIO to make predictions for the statistics of major mergers.

In order to investigate the statistic on major mergers in detail, we count the number of major mergers for each of the halos in the ensemble of simulations P0. Here again we only trace a halo back to a time when the mass of its main progenitor is 1% of the halo's final mass. This choice of lower mass limit is quite arbitrary. However, some limit is necessary, because otherwise there will be a large number of major mergers involving progenitors with excessively small masses at very early times. Furthermore this mass limit is also the one we use in defining $N_{\rm jump}$. The large number of halos in the ensemble ensures that each mass bin contains about 2000 halos. Fig. 2.10 plots the distributions of the number of major mergers (with a progenitor mass ratio $\geq 1/3$) for halos of different masses at the present time. A halo experiences about 1 to 5 major mergers during its mass assembly history, with an average of about 3. Note that the $N_{\rm mm}$-distributions are virtually independent of halo mass. As we have shown in Section 2.5, however, the redshifts at which these mergers occur do depend strongly on halo mass: while most major mergers occur before $z \simeq 2$ for galaxy-sized halos, they occur much more recently in the more massive, cluster-sized halos.

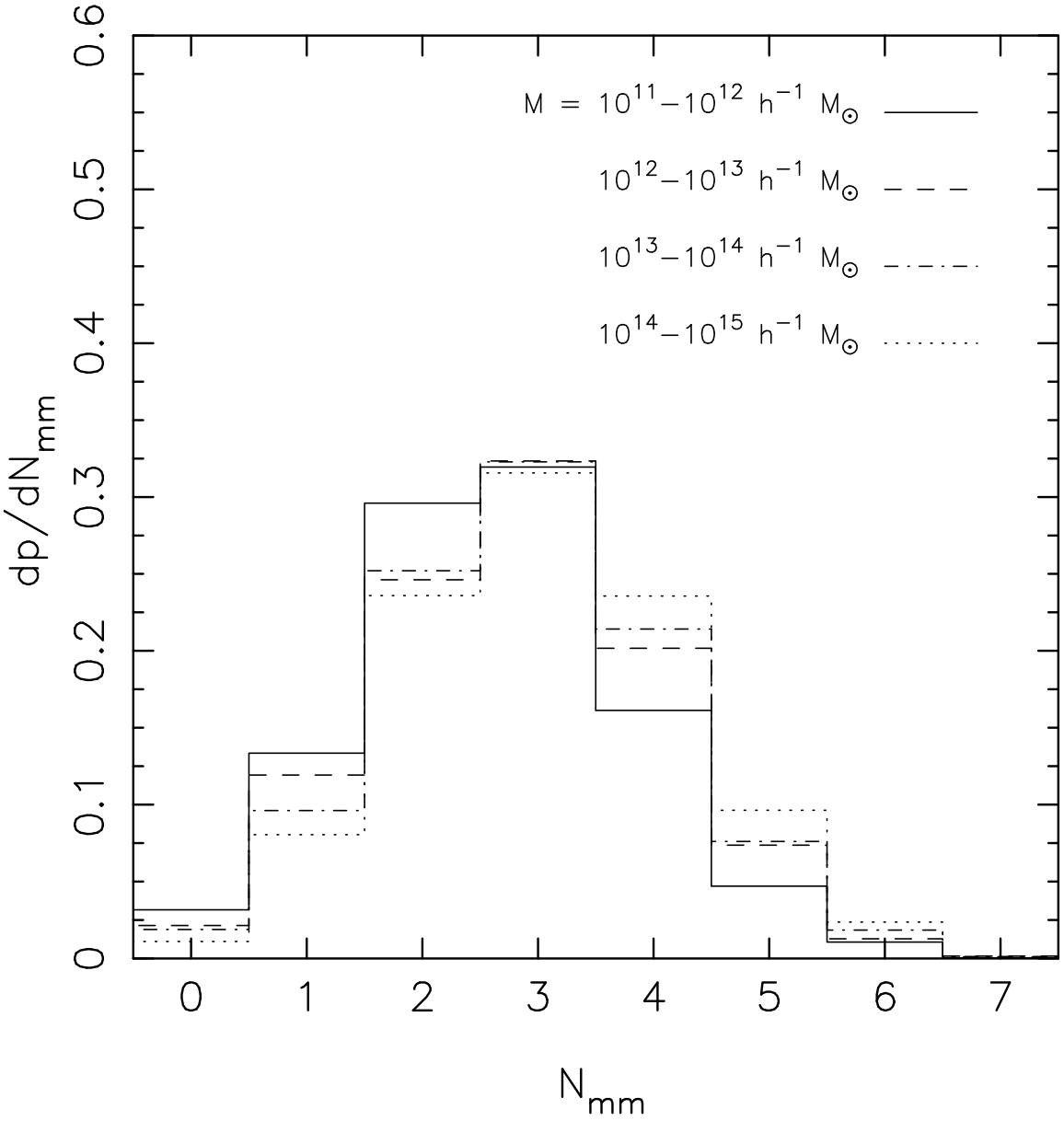

Figure 2.10. The distribution of the number of major mergers (those with a mass ratio larger than 1/3) in our PINOCCHIO simulations. Lines in different styles represent different mass bins. Note that the distributions are virtually independent of halo mass.

As pointed out above, the progenitor mass ratio used to define a major merger is quite arbitrary. We therefore also investigate the frequency of mergers with a mass ratio larger than $1/n$ with $n = 2, 4, 5, 6, 7, 8$ (in addition to the $n = 3$ discussed thus far). We find that even with these values of n the distributions of $N_{\rm mm}$ are still virtu-

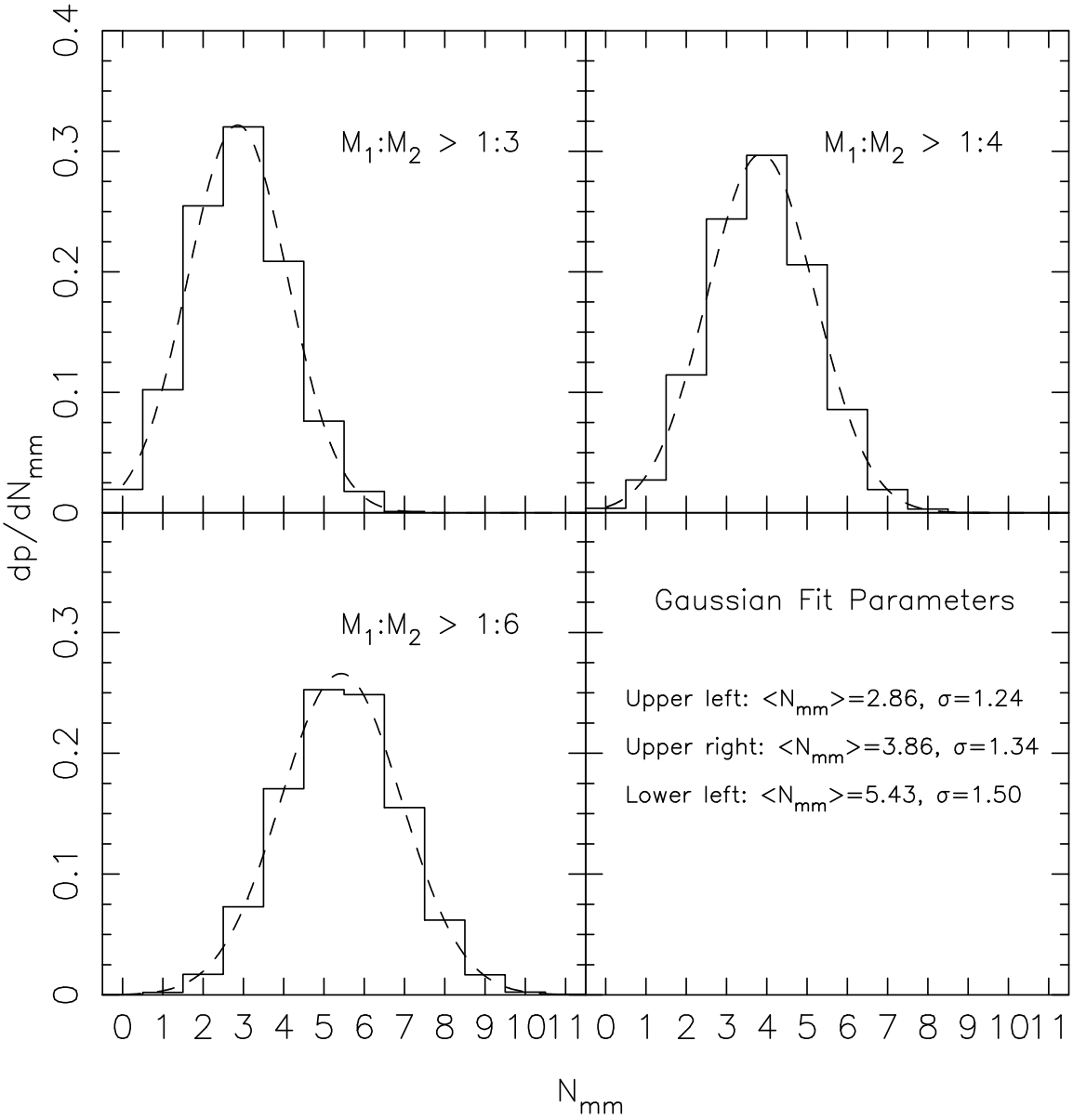

Figure 2.11. Distribution of the number of mergers (in PINOCCHIO simulations) with a mass ratio larger than 1/3 (upper left-hand panel), 1/4 (upper right-hand panel), and 1/6 (lower left-hand panel). In all three cases all halos with masses in the range from $10^{11}h^{-1}\,\mathrm{M}_\odot$ to $10^{15}h^{-1}\,\mathrm{M}_\odot$ are used. The dotted curves show the best-fit Gaussians, the median and standard deviation of which are indicated in the lower right-hand panel.

ally independent of halo mass. This allows us to consider a single $N_{\rm mm}$-distribution for halos of all masses. Fig. 2.11 plots these distributions for three different values of n as indicated. Each of these distributions is reasonably well described by a Gaussian

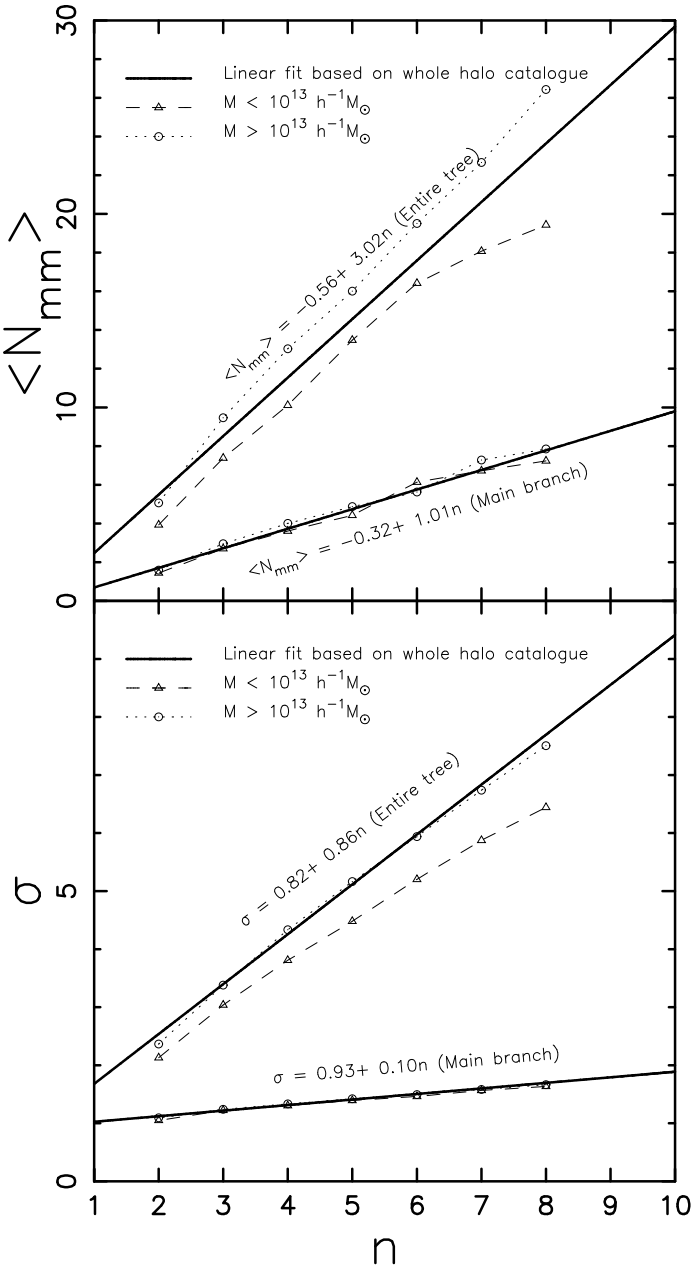

Figure 2.12. The median (upper panel) and dispersion (lower panel) of the number distributions of mergers with a mass ratio $M_1/M_2 \geq 1/n$, as a function of n. Steeper lines in each panel are the data from all progenitors (summing over all branches of the merger trees) while flatter lines are the results from the main branch. In both cases, we have divided halos into two mass bins as indicated in each panel. Open triangles connected with dashed lines show the results for halos with masses $< 10^{13}h^{-1}\mathrm{M}_{\odot}$, while open circles connected with dotted lines show the results for halos with masses $\geq 10^{13}h^{-1}\mathrm{M}_{\odot}$. The solid lines are the linear regressions of the data drawn from the whole halo catalogue, with the slopes and zero points indicated.

function (dashed curves). Note that the use of a Gaussian function is not entirely appropriate, because $N_{\rm mm}$ cannot be negative. However, since the median value of $N_{\rm mm}$ is, in all cases, significantly larger than the width of the distribution, a Gaussian fit is still appropriate. To show how the $N_{\rm mm}$-distribution depends on n, we plot, as in Fig. 2.12, the median and the dispersion of this distribution as functions of n. As one can see, both the median and the dispersion increase roughly linearly with n, but the slope for the median (~ 1) is much larger than that for the dispersion (~ 0.1). Note that the results for halos with masses $< 10^{13}h^{-1}\,{\rm M}_\odot$ and $> 10^{13}h^{-1}\,{\rm M}_\odot$ are similar, suggesting the distribution of the number of major mergers is quite independent of halo mass.

Thus far we have only focused on the (major) merger events that merge into the main branch of the merger tree. For comparison, we also consider the merger rates of *all* progenitors, independent of whether they are part of the main branch or not. As before we only consider progenitors with masses in excess of one percent of the final halo mass. The skewer lines in Fig. 2.12 show the median and dispersion of the number of such mergers as functions of n. Here again, both the median and dispersion have roughly linear relations with n. The median number of such major mergers is roughly three times as high as that of major mergers associated with the main branch, and the dispersion increases with n much faster.

2.7 Fast and slow accretion phases

As mentioned above, major mergers are expected to be accompanied by rapid changes of the halo's potential well, due to a resulting phase of violent relaxation. To show such relation in more detail, Fig. 2.13 shows the distributions of the number of major mergers (defined with $n = 3$) before and after the formation redshift $z_{\rm vmax}$. For halos in all mass ranges, only a very small fraction (less than 5%) experiences

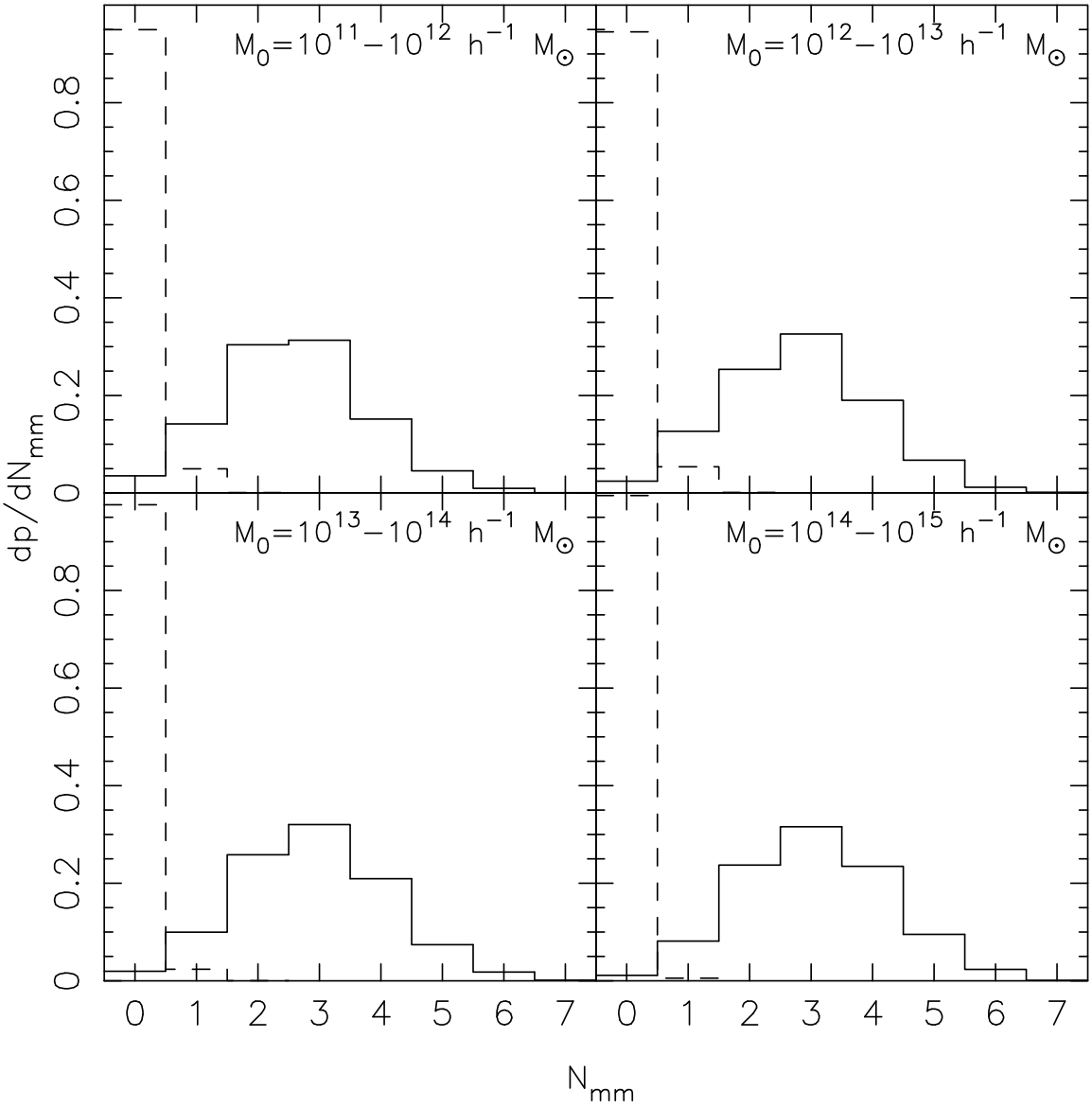

Figure 2.13. The probability distributions of the number of major mergers (those with a mass ratio larger than 1/3) before (solid lines) and after (dashed lines) $z_{\rm vmax}$. Note that the vast majority of major mergers occur at $z > z_{\rm vmax}$, demonstrating that the growth of the halo's virial velocity is mainly driven by major mergers.

a major merger at $z < z_{\rm vmax}$. This demonstrates once again that the growth of the virial velocity is mainly caused by major mergers.

Fig. 2.14 demonstrates the MAHs of 30 dark halos randomly selected from one of our PINOCCHIO simulations with cubic box size 40 h^{-1}Mpc on a side. Each halo MAH is calibrated to $z_{\rm vmax}$, in the way that both the mass $M(z)$ and the physi-

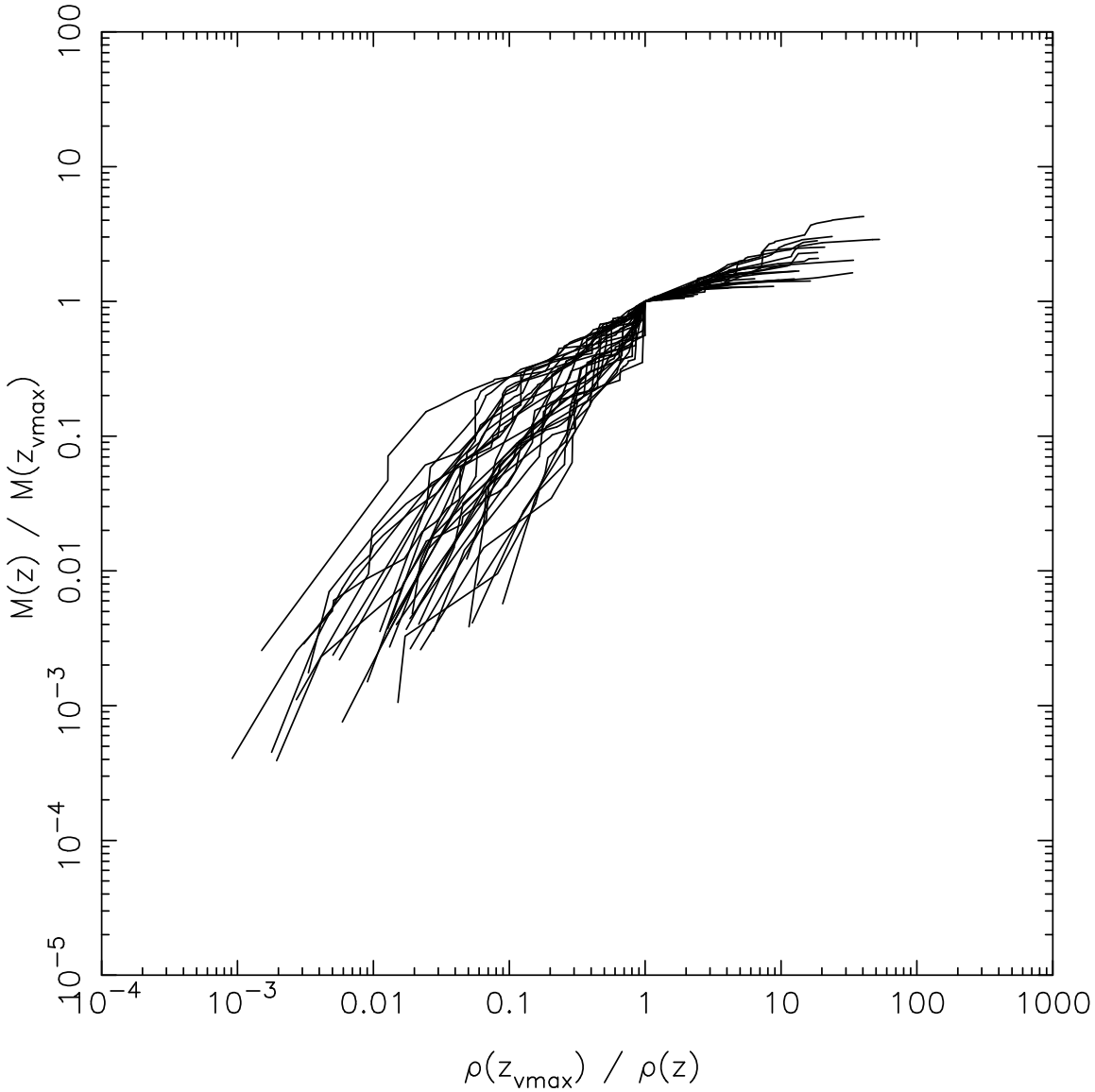

Figure 2.14. Randomly selected halo MAHs calibrated to $z_{\rm vmax}$, when the mass accretion changes from the fast phase to the slow phase. Vertical axis is the halo mass $M(z)$ scaled to $M(z_{\rm vmax})$, and horizontal axis is the halo physical density $\rho(z)$ scaled $\rho(z_{\rm vmax})$.

cal density $\rho(z)$ of the halo are scaled to their quantities at this particular epoch, $M(z_{\rm vmax})$ and $\rho(z_{\rm vmax})$. Clearly, after $z_{\rm vmax}$, the mass growth of each halo becomes flatter and smoother compared to its mass growth before $z_{\rm vmax}$, due to the lack of major mergers. However, the ratio between the final halo mass and $M(z_{\rm vmax})$ varies in a wide range and can be as large as ~ 10. This indicates that some halos have

terminated their fast accretion phase well before they acquire the main body of their mass. Based on five well-identified halos in their N-body simulations, Zhao et al. (2003a) proposed an empirical formula to determine the time $z_{\rm tp}$ (redshift at the so-called "turn point") when the mass accretion of the five halos changes from fast to slow. They suggested that $z_{\rm tp}$ equals the time when $V_{\rm v}H(z)^{\gamma}$ reaches its maximum, where $\gamma = -1/4$ to $-1/8$. While seemingly different, the epoch of their "turn point" is in fact quite similar to $z_{\rm vmax}$. Since γ is small, the effect of the Hubble expansion they tried to account for is negligible. On the other hand, $z_{\rm vmax}$ as the time that separates the two accretion phases, is more clearly defined, and directly suggests that the potential well of a dark halo is mainly driven by the fast accretion phase.

The results presented above may have important implications for understanding the structure of dark matter halos. As shown in Lu et al. (2006), if the buildup of the potential well associated with a dark matter halo is through major mergers, then the velocities of dark matter particles may be effectively randomized, a condition that may lead to a density profile close to the universal density profile observed in N-body simulations. Also, if galaxy disks are formed during a period when no major mergers occur, our result suggests that the potential wells of the halos of spiral galaxies should change little during disk formation.

2.8 The relationship between halo density profile and its mass accretion phases

As mentioned in Chapter 1, high-resolution N-body simulations have demonstrated that the density profile of CDM halos can roughly be described by a universal functional form, equation (1.15). The overall shape of the density distribution can be characterized by the so-called concentration parameter $c = R_{\rm v}/r_{\rm s}$. Several studies have shown that c is correlated with the halo's mass assembly history. In particular, (Zhao et al., 2003a) have shown that the value of $r_{\rm s}$ changes little during the slow

accretion phase so that c increases linearly with $R_{\rm v}$. During the fast accretion phase, however, $r_{\rm s}$ and $R_{\rm v}$ grow more or less in sync, so that c remains roughly constant. Therefore, if the transition from the fast accretion phase to the slow accretion phase occurs at a redshift $z_{\rm f}$, the halo concentration at the present time can approximately be written as

$$c = \frac{H(z_{\rm f})}{H_0}\left[\frac{\Delta_{\rm vir}(z_{\rm f})}{\Delta_{\rm vir,0}}\right]^{1/2}\frac{V_0}{V_{\rm v}(z_{\rm f})}c(z_{\rm f})\,, \tag{2.14}$$

with $c(z_{\rm f})$ the halo concentration at the transition redshift. Both W02 and Zhao et al. (2003a) have shown that $c(z_{\rm f}) \simeq 4$, which is the value we adopt in what follows. As discussed in Section 2.5, the formation redshift $z_{\rm vmax}$ roughly separates the MAH of a halo into a fast- and a slow accretion phase, so that we may replace $z_{\rm f}$ in equation (2.14) with $z_{\rm vmax}$.

However, our conclusion that $z_{\rm vmax}$ is a suitable candidate which indicates the transition redshift during the halo MAH is based on the analysis of major merger events, in which the definition of a major merger can be arbitrary. Therefore, it is appropriate to perform a more direct check on the original assumption that it is the early fast accretion that mainly contributes the mass into the inner region within $r_{\rm s}$ of a final halo. We use our N-body simulation S1 and follow these steps to this end: (1) for a final halo at $z = 0$, we fit its density profile according to equation (1.15) and identify its central region characterized by $r_{\rm s}$, (2) we monitor the MAH of this halo and mark its corresponding $z_{\rm vmax}$, (3) we then identify each particle within $r_{\rm s}$ and determine how many of them have already been in a position, before $z_{\rm vmax}$, with a distance to the most bound particle of the halo shorter than $r_{\rm s}$. The result is shown in Fig. 2.15. Note that in this analysis, we only use halos with more than 1000 particles, with an equivalent mass of $5.5 \times 10^{11}\ h^{-1}{\rm M}_{\odot}$, in order to ensure an appropriate fit of the density profile at $z = 0$ as well as sufficient number of particles at $z_{\rm vmax}$. The vertical axis of Fig. 2.15 denotes the number fraction of particles that have already been accreted into the central region of a halo, characterized by $r_{\rm s}$, before $z_{\rm vmax}$.

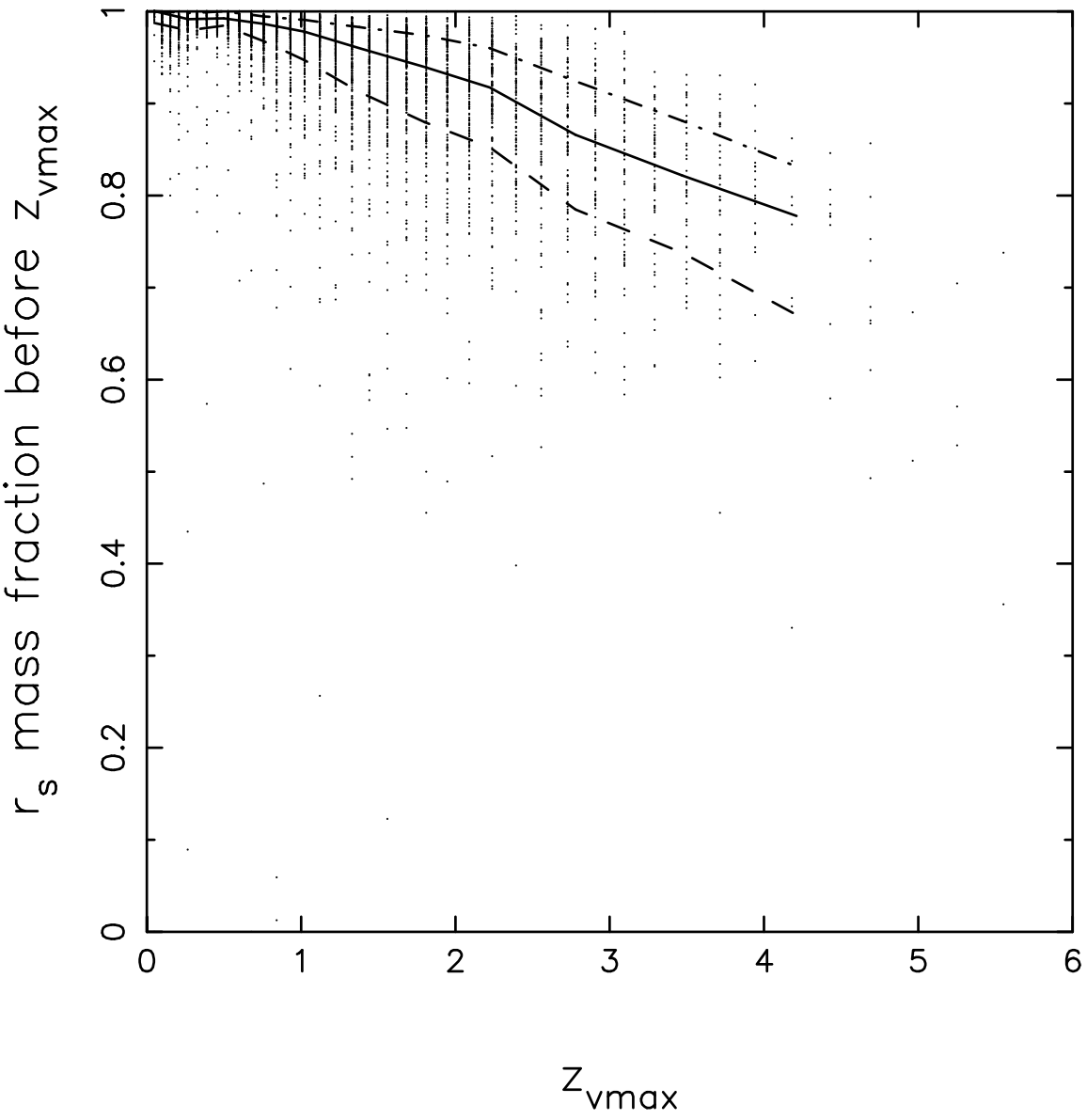

Figure 2.15. Fraction of the mass that enters $r_{\rm s}$ before $z_{\rm vmax}$. Each point represents the number fraction of particles that have already been accreted to the central region of a halo, characterized by $r_{\rm s}$, before $z_{\rm vmax}$. Solid line and the two dashed lines are the median, 20% and 80% percentiles, respectively, given redshift z.

Interestingly, for almost all halos, this fraction is higher than 80%, even though $z_{\rm vmax}$ spans a wide range ($z_{\rm vmax} \in [0, 5]$). There is a general decreasing trend as $z_{\rm vmax}$ increases, indicating that the fraction of mass within $r_{\rm s}$ contributed by the later slow accretion becomes larger if the fast accretion phase terminates earlier.

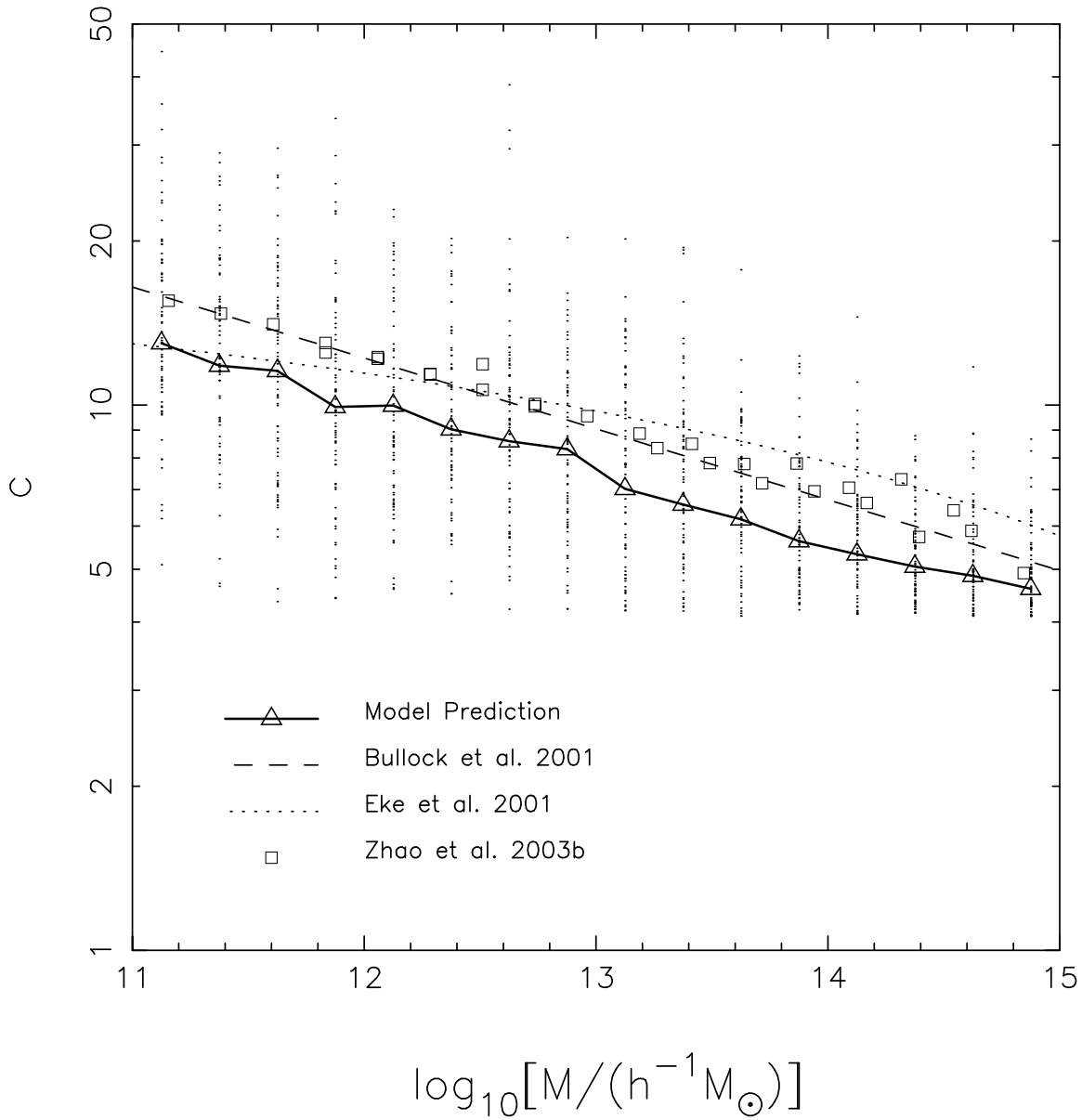

Figure 2.16. Model-predicted c v.s. halo mass in comparison with N-body simulations. The open triangles connected by a solid line show the halo concentrations as function of halo mass, predicted from the PINOCCHIO MAHs and equation (2.14) with $c(z_{\rm f}) = 4$. For each mass bin we show a random subset of 70 concentrations (small dots), which give a rough indication of the scatter as function of halo mass. For comparison, we also show the N-body simulation results from Zhao et al. (2003a,b, open squares), Bullock et al. (2001b, dashed line) and Eke, Navarro & Steinmetz (2001, dotted line).

The above results demonstrate that $z_{\rm vmax}$ is indeed a suitable candidate to replace $z_{\rm f}$ in equation (2.14). This allows us to compute, for each halo, a predicted value for

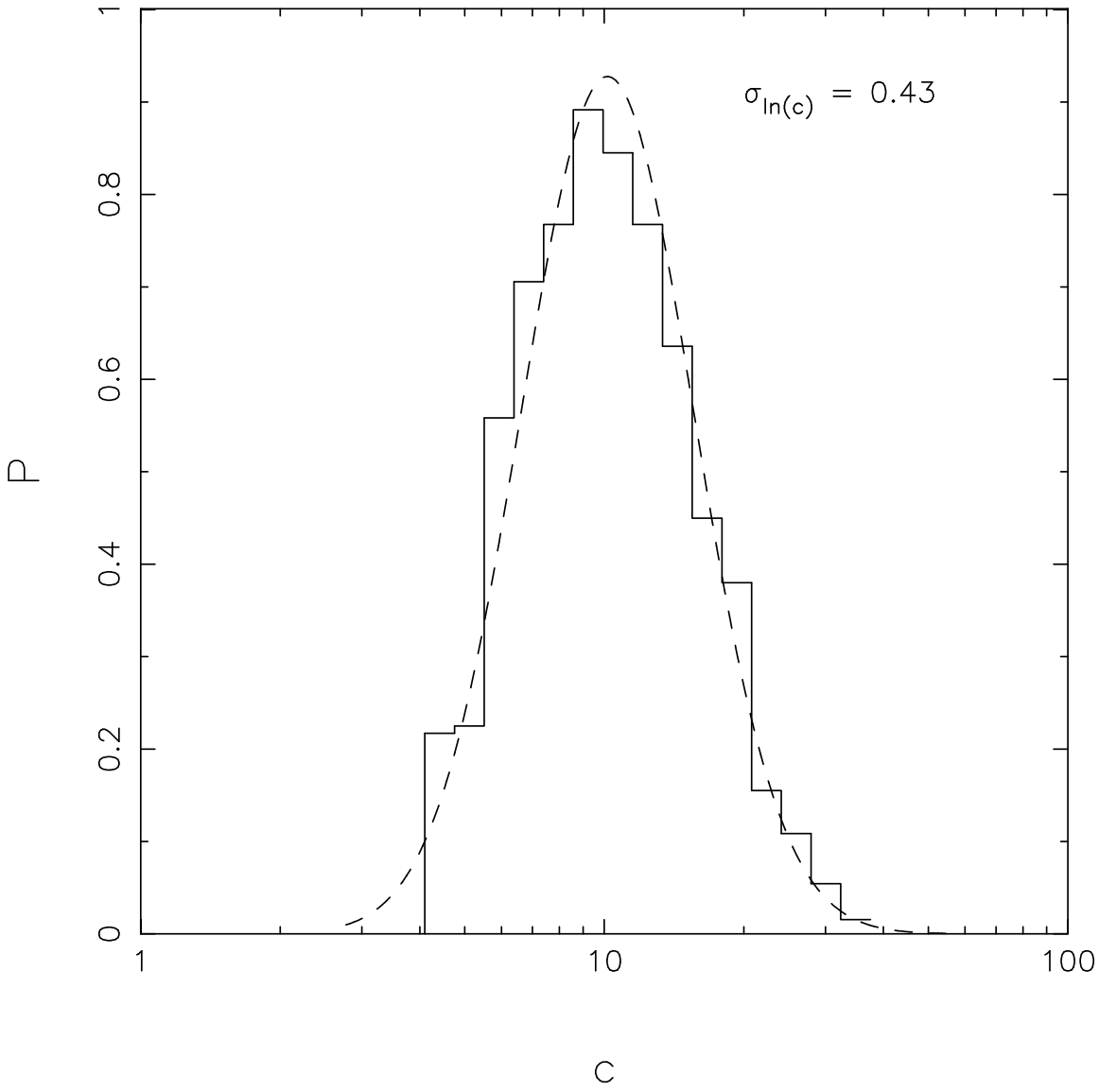

Figure 2.17. Scatter in the predicted c. The distribution of predicted halo concentration parameters, c, for halos with $M_0 = (1.35 \pm 0.35) \times 10^{12}\,\mathrm{M}_\odot$. The distribution is well fit by a log-normal distribution (dashed line) with a median c of 10.16 and a dispersion $\sigma_{\ln c} \approx 0.43$. This dispersion is significantly larger than what one obtains from N-body simulations. See text for a detailed discussion.

its halo concentration parameter c, even without the knowledge of the detailed mass distribution of a final halo. The prediction based on this simple toy model is shown in Fig. 2.16 as a function of the present day halo mass (open triangles connected by a solid line). For comparison, we also show the simulation results of Bullock et al.

(2001b, dashed line), Eke, Navarro & Steinmetz (2001, dotted line) and Zhao et al. (2003a,b, open squares). Except for a small offset of ~ 20 percent to somewhat lower values, our predictions are in good agreement with these numerical simulation results. In particular, the scaling with halo mass is nicely reproduced. This implies that one can use the MAHs extracted from PINOCCHIO to predict the halo's concentration. The offset is easily corrected for by setting $c(z_{\rm f})$ in equation (2.14) to 5, rather than 4.

If c is completely determined by the halo formation time, as assumed here, then the scatter in c simply reflects the scatter in $z_{\rm vmax}$. Fig. 2.17 plots the predicted distribution function of c for halos with masses $M_0 = 1 \sim 1.7 \times 10^{12} h^{-1}\,{\rm M}_\odot$. The distribution is well fit by a log-normal distribution (dashed curve), in good agreement with the results from N-body simulations (e.g., Jing, 2000; Bullock et al., 2001b). However, the predicted dispersion, $\sigma_{\ln c} \approx 0.43$, is significantly larger than the values obtained from simulations, which range from $\sigma_{\ln c} \approx 0.25$ (Jing, 2000) to $\sigma_{\ln c} \approx 0.32$ (Bullock et al., 2001b). In addition, as shown in W02, the smaller value obtained by Jing (2000) most likely owes to the fact that he only focused on halos that are well relaxed. Since W02 basically includes all halos, our predicted scatter in c, which amounts to 54 percent, should be compared to theirs (38 percent). The most likely explanation for our overestimate of the scatter is that the hierarchical assembly of individual dark matter halos is a noisy process. A more appropriate (less noisy) single parameter to characterize the MAH would be one that captures the overall shape, rather than a single characteristic event. W02 fitted each MAH with the functional form $M(z)/M_0 = \exp[-2z/(1+z_{\rm f})]$ [another form of equation (1.18) assuming $c = 4.1(1+z_{\rm f})$ as suggested by W02], and showed that the scatter in the formation redshift $z_{\rm f}$ thus defined is significantly smaller than the scatter in the more prevalent formation redshift $z_{\rm half}$, which, just like $z_{\rm vmax}$, is based on a single event during the halo's MAH. W02 have shown that the halo concentration parameter is tightly correlated with $z_{\rm f}$,

and that the scatter in c predicted from the scatter in $z_{\rm f}$ is in good agreement with the scatter found in numerical simulations.

However, the MAHs of individual dark matter halos are usually quite complicated, and in many cases cannot be well fit by a simple functional form. As shown in Lu et al. (2006), the correlation between halo concentration and mass, and the distribution of halo concentrations obtained from cosmological N-body simulations can all be reproduced in their models when using the *entire* merger histories of dark matter halos. However, when using the functional form suggested by W02 to represent individual merger histories, the mass-concentration correlation and the distribution of halo concentrations in cosmological N-body simulations are not well reproduced. This owes to the fact that the results depend sensitively on how the actual MAHs are fitted (see Lu et al. 2006 for details). Thus, although one can define a single formation time that correlates strongly with the halo concentration, more accurate predictions require information regarding the *entire* merger history (i.e., cannot be parameterized by a single parameter).

2.9 Conclusions

In the current paradigm, galaxies are thought to form in extended cold dark matter halos. A detailed understanding of galaxy formation, therefore, requires a detailed understanding of how these dark matter halos assemble. Halo formation histories are typically studied using either numerical simulations, which are time consuming, or using the extended Press-Schechter formalism, which has been shown to be of insufficient accuracy. In this Chapter, we have investigated the growth history of dark matter halos using the Lagrangian perturbation code PINOCCHIO , developed by Monaco et al. (2002a). We have demonstrated that the mass assembly histories (MAHs) obtained by PINOCCHIO are in good agreement with those obtained using N-body simulations. Since PINOCCHIO is very fast to run, does not require any

special hardware such as supercomputers or Beowulf clusters, and does not require any labor intensive analysis, it provides a unique and powerful tool to study the statistics and assembly histories of large samples of dark matter halos for different cosmologies.

Confirming earlier results based on N-body simulations (e.g. W02; Zhao et al., 2003a,b), we find that typical MAHs can be separated into two phases: an early, fast accretion phase dominated by major mergers, and a late, slow accretion phase during which the mass is mainly accreted from minor mergers. However, the MAHs of individual halos are complicated, and therefore difficult to parameterize uniquely by a single parameter. We therefore defined four different formation times: the time when a halo acquires half of its final mass, the time when the halo's potential well is established, the time when a halo transits from the fast accretion phase to the slow accretion phase, and the time when a halo experiences its last major merger. Using a large number of MAHs of halos spanning a wide range in masses, we studied the correlations between these four formation redshifts, as well as their halo mass dependence. Although all four formation times are correlated, each correlation reveals a larger amount of scatter.

For all four formation redshifts, it is found that more massive halos assemble later, expressing the hierarchical nature of structure formation. Halos with masses below the characteristic non-linear mass scale, M_*, establish their potential wells well before they have acquired half of their present day mass. The potential wells associated with more massive halos, however, continue to deepen even at the present time. The time when a halo reaches its maximum virial velocity roughly coincides with the time where the MAH transits from the fast to the slow accretion phase.

If we define major mergers as those with a progenitor mass ratio larger than 1/3, then on average each halo experiences about 3 major mergers after its main progenitor has acquired one percent of its present day mass. The distribution of the number of

major mergers a halo has experienced is virtually independent of its mass, and the ratio between the halo mass immediately after the last major merger and the final halo mass has a very broad distribution.

Assuming that the inner structure of a halo does not change during the slow accretion phase, one can predict the NFW concentration parameter, c, of the halo based on its MAH. The predicted relation between c and halo mass is in good agreement with numerical simulations, but the model predicts a distribution at fixed mass that is too broad. This owes to the noisy character of individual MAHs, which are only poorly described by a single parameter. More accurate predictions of halo concentrations require detailed information regarding the entire mass assembly histories.

CHAPTER 3

DARK HALO ASSEMBLY BIAS

3.1 Introduction

In the previous studies, this formation history of dark matter halos is usually characterized by a single parameter which is the time when a halo has acquired half of its final halo mass (e.g. Lacey & Cole, 1993; Lemson & Kauffmann, 1999; van den Bosch, 2002a; Gao et al., 2005). This definition of halo formation time is useful because it indicates when the main body of a halo is assembled. However, it is unclear if such definition is closely related to how galaxies form in a halo. For example, van den Bosch et al. (2003a) and Yang et al. (2003) both found that dark halos with masses around $10^{11.5}\,h^{-1}\mathrm{M}_{\odot}$ have the lowest mass-to-light ratio, which suggests that star formation is the most efficient in halos with a fixed mass around $10^{11-12}\,h^{-1}\mathrm{M}_{\odot}$. Thus, for halos with masses much larger than this mass, the half-mass assembly time may have little to do with how galaxies may have formed in such halos. Based on the half mass formation time, more massive halos are expected to form later due to hierarchical clustering. This is in contrast with the recent observations that the stellar population in more massive systems are generally older (e.g. Thomas et al., 2005; Nelan et al., 2005). This phenomenon, known as the "archaeological down-sizing", appears to be in contradiction with the "hierarchical" formation scenario, but may also indicate that the growth of galaxies in a halo does not follow the growth of the halo.

Recently Gao, Springel & White (2005, see also Wechsler et al., 2006; Harker et al., 2006; Jing, Suto & Mo, 2007; Gao et al., 2007) found that, the half-mass assembly

time of a halo is also correlated with halo clustering properties on large scales. Using N-body simulations, these authors find that, for halos of a given present mass that is smaller than M_*, the ones that assembled half of their final masses earlier are more strongly clustered in space. On the contrary, for halos more massive than M_*, the ones that assembled half of their final masses later are more strongly clustered. If the star formation history is somehow correlated with dark halo formation history, as is expected from current theory of galaxy formation, these results would indicate that galaxy systems, such as clusters and groups, of the same mass but containing different galaxy populations should also show different clustering properties. Observationally, there is evidence to support such connection, although discrepancies remain among the different results. The results of Wang et al. (2008) and Yang et al. (2006) suggest that redder groups are more strongly clustered than bluer ones for low-mass groups and becomes insignificant for groups with halo masses above $\sim 10^{13}\,h^{-1}\mathrm{M}_{\odot}$, but the results of Berlind et al. (2006) and Tinker et al. (2008) do not show such trend.

The dependence found by Wang et al. (2008) and Yang et al. (2006) has the same trend as the formation-time dependence of halo clustering, and it is tempting to link these two types of dependence. However, as mentioned above, the half-mass assembly time may not be a good indicator of the typical formation time of stars in a halo. Indeed, using a "shuffling" technique, Croton et al. (2007) found that, the dependence of halo bias on halo half-mass assembly time can only account for about half of the clustering bias seen in red halos in their semi-analytical catalogue. Clearly, in order to understand the observational results in terms of halo assembly bias, one needs to define halo formation times that are more closely related to the formation of galaxies in dark matter halos.

The main goal of this Chapter is to systematically study when various characteristic events take place in the halo assembly process and how they are correlated with halo mass and with the large-scale environments. To this end, we define a number

of formation times to characterize each halo formation history. We study in detail how each of these formation times is correlated with halo mass and how the halo correlation amplitude depends on these formation times. Our analysis is based on the"Millennium Simulation" (Springel et al., 2005a). The Chapter is organized as follows. In Section 3.2, we briefly describe the simulation and the techniques to identify halos and to construct merging trees. In Section 3.3, we describe our definitions of halo assembly times and how to estimate them from the simulation, and study how they are correlated with halo mass. In Section 3.4, we present the results on the formation-time (age) dependence of halo clustering. Finally, in Section 3.5, we summarize and discuss the implications of our results.

3.2 The Millennium Simulation

3.2.1 Basic facts of the simulation

In this work, we use the "Millennium Simulation" (MS) carried out by the Virgo Consortium (Springel et al., 2005a). The MS uses the GADGET-2 code which is based on the "TreePM" algorithm, a combination of the classical Fourier-transform particle-mesh method and the hierarchical multiple expansion "tree" method. This simulation follows the evolution of 2160^3 dark matter particles in a cubic box of $500\,h^{-1}$Mpc on a side. The particle mass is approximately $8.6 \times 10^8\,h^{-1}\mathrm{M}_\odot$, which enables us to study the assembly of halos more massive than $\sim 10^{11}\,h^{-1}\mathrm{M}_\odot$ with a reasonable mass resolution. The simulation adopts a flat ΛCDM model with $\Omega_\mathrm{M} = \Omega_\mathrm{dm} + \Omega_\mathrm{B,0} = 0.205 + 0.045 = 0.25$, where Ω_dm and $\Omega_\mathrm{B,0}$ stand for the current densities of dark matter and baryons respectively; the linear r.m.s. (root-mean-square) density fluctuation in a sphere of an $8\,h^{-1}$Mpc radius, σ_8, equals 0.9; and Hubble expansion parameter $h = 0.73$. This set of cosmological parameters is in agreement with the first-year WMAP data. The initial cosmic density field of the MS is generated with a realization of a Gaussian random field with the ΛCDM (parameters specified above)

linear power spectrum given by the Boltzmann code CMBFAST. The displacement field was then constructed using the Zel'dovich approximation. The gravitational force is softened on a co-moving scale of $5\,h^{-1}$Mpc (Plummer-equivalent).

The MS started at $z = 127$ and evolves the density field to the present with a leapfrog integration. Totally there are 63 snapshot outputs between $z = 0$ and $z = 80$, which are almost evenly placed in $\ln(1 + z)$ space. In the MS simulation, the characteristic collapsing mass, M_*, defined through $\sigma(M_*) = 1.69$, is about $6 \times 10^{12}\,h^{-1}\mathrm{M}_\odot$. In order to identify dark halos, the Friends-Of-Friends (FOF) algorithm with a linking length $b_\mathrm{l} = 0.2$ times the mean particle separation is used, so that the structures identified (we will call them FOF groups hereafter) have a density approximately 200 times the mean cosmic density. In addition, by smoothing the FOF groups outside-in, each FOF group is also assigned a corresponding "virial halo" with a "virial mass" M_v, so that the average density contrast between the "virial halo" and cosmic critical density ρ_c, Δ_v, is roughly described by equation (1.16). The radius at which the density contrast (when being smoothed outside-in), first reaches $\Delta_\mathrm{v}(z)$, defines the virial radius, R_v, of the halo. Despite the fact that M_v is slightly (typically 5%) smaller than the corresponding FOF group mass, there are no other significant differences when one studies the accretion history of dark halos. In what follows, we always use "virial halos" in our analysis. Same as in Chapter 2, given a cosmological model, we define the virial velocity $V_\mathrm{v}(z)$ of a growing halo at redshift z, according to equation (2.13). With these definitions, we can follow the growth of the virial velocity (which is a measure of the halo gravitational depth) using the growth of the halo mass.

3.2.2 Sub-halo based dark halo merging trees

The merging trees of dark halos in the MS, however, are constructed on the basis of sub-halos. In each FOF group, sub-halos are identified using SUBFIND (Springel

et al., 2001). A sub-halo selected by SUBFIND must meet two requirements: first, it is a localized overdense region; second, all particles within this sub-halo satisfy self-boundness. A sub-halo 1 at redshift z_1 is considered a progenitor of another sub-halo 2 at z_2 ($z_1 > z_2$) if its largest number of self-bound particles are settled in sub-halo 2, and sub-halo 2 is called the descendant of sub-halo 1 [see Fakhouri & Ma (2008) for a more elaborate description of the merging trees]. Although, in general, the particles in one progenitor sub-halo do not necessarily end up in the same descendant sub-halo, the procedure described above ensures that each progenitor sub-halo has and only has one single descendant. Connecting sub-halos across the 63 snapshot outputs in this way results in the merging history tree of each isolated dark halo identified at a given redshift. Note that in most simulations, standard merging trees of dark halos are constructed based on FOF groups rather than sub-halos. However, the basic criteria to build the kinship between halos at two adjacent snapshots are the same as in the MS sub-halo merging trees.

In addition to sub-halos, each FOF group contains one and only one "main virial halo", with mass $M_{\rm v}$. The "main virial halo" holds up the majority of the FOF group mass. In our analysis, we use $M_{\rm v}$ to construct the mass growth history of the final halo. Since in general $M_{\rm v}$ accounts for the central part of an FOF group, this treatment naturally avoids the ambiguous case where some accidentally linked sub-halos that do not belong to the halo also contribute to the halo mass.

3.3 Halo formation times in the Millennium Simulation

3.3.1 Definitions of halo formation times

As mentioned above, the formation of dark halos is a very complicated process. There are two ways to follow the mass growth of a halo with time. First, one can start with a halo at the present time, pick up the most massive progenitor in the *adjacent* snapshot at higher redshift, and repeat this procedure for the selected pro-

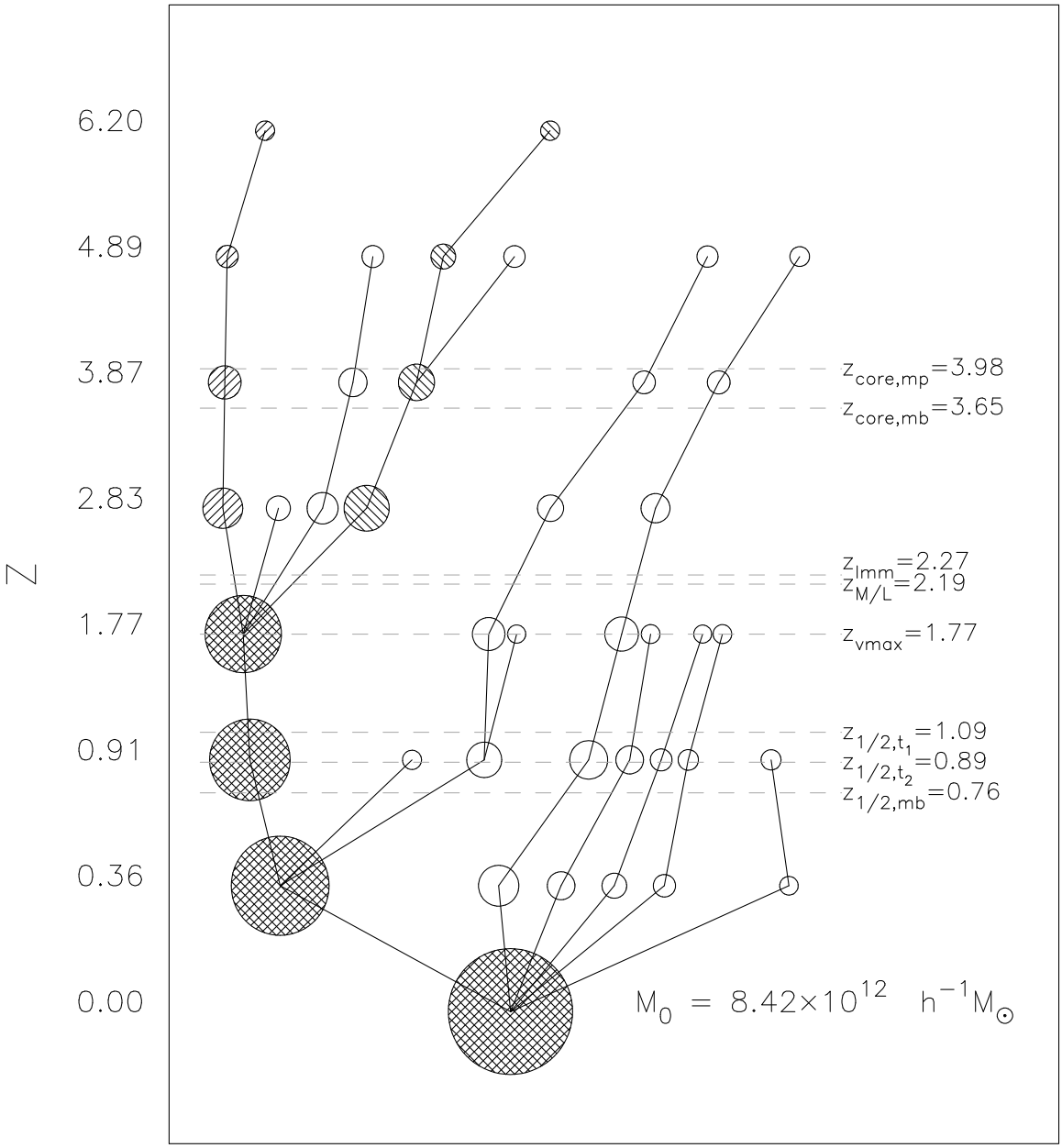

Figure 3.1. Merging history of a typical MS halo, with all the defined formation times marked. Progenitors greater than $4\times10^{10}h^{-1}\mathrm{M}_\odot$ are output at selected redshifts to avoid crowdedness. The radius of each circle is roughly proportional to $M^{1/3}$. Circles filled with hatch lines that are 45° clockwise to the vertical represent the main branch progenitors; while those filled with hatch lines that are 45° counter-clockwise to the vertical represent the maximum progenitors.

genitor until the progenitor mass is so small that it cannot be resolved anymore. The mass accretion history of the halo is then represented by the growth of the progenitor mass along the "main branch". Alternatively, one can always look up the most mas-

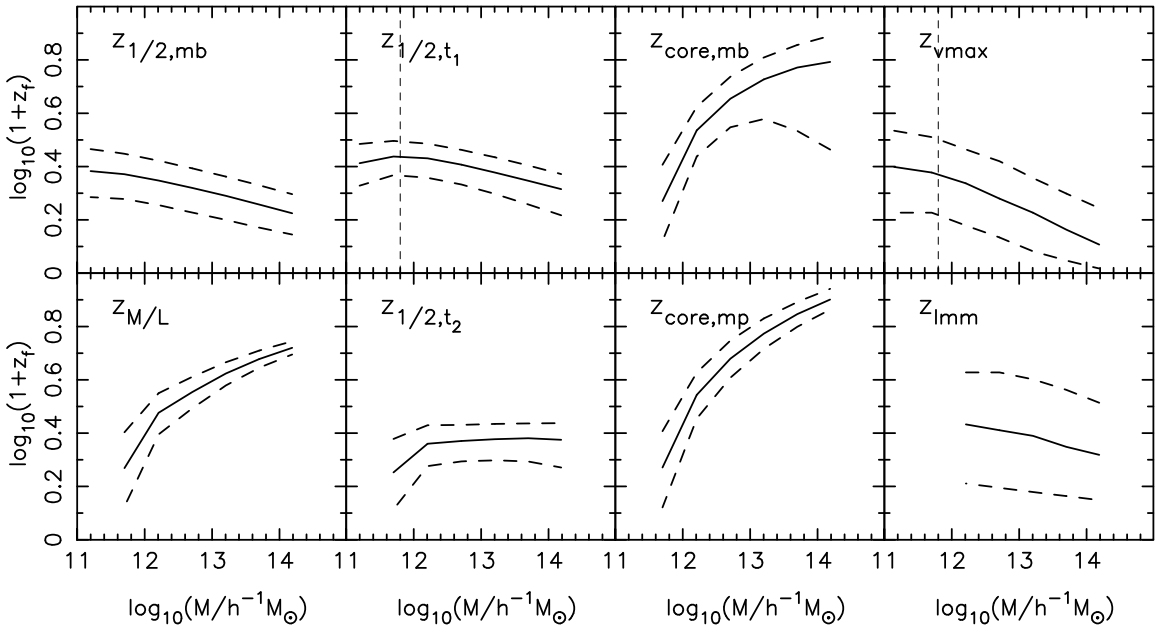

Figure 3.2. Formation time v.s. halo mass. Solid line represents the median of each mass bin, while dashed lines represent 20% and 80% quantiles, respectively. Note that in the panels for $z_{1/2,\mathrm{t_1}}$ and z_{vmax}, the slight drop at the low mass end (to the left of the vertical dashed line) is due to the finite mass resolution of the simulation, because small progenitors cannot all be resolved for halos that are too small.

sive progenitor at each redshift on the merging tree of a given halo, and concatenate on these progenitors chronologically. The mass accretion history so obtained reflects the growth of the "maximum progenitor". Note that the halo main branch does not always represent the maximum progenitor of a halo at each redshift, especially at the early stage of a growing halo (e.g. Gao et al., 2004b). Most of the previous studies have been concentrated on the "main branch" when studying the halo assembly histories (e.g. Lacey & Cole, 1993; van den Bosch, 2002a; Gao et al., 2005; Wechsler et al., 2006). In this Chapter, we use both definitions. We define the following set of parameters to characterize the assembly history of a halo:

1. $z_{1/2,\mathrm{mb}}$: This is the redshift at which the halo main branch has assembled half of its final mass, $M_{\mathrm{v}}(0)$. This formation time has been widely used in the literature, as mentioned before.

2. $z_{1/2,\mathrm{t}_1}$: This is the highest redshift at which half of the final halo mass is contained in progenitors with masses (M_p) greater than $0.02M_\mathrm{v}(0)$. The same kind of formation time has been used in Navarro, Frenk & White (1997) to characterize the formation time of a halo and to study how halo concentration is correlated with formation time.

3. $z_{1/2,\mathrm{t}_2}$: This is the highest redshift at which half of the final halo mass has assembled into progenitors more massive than a fixed mass, $M_\mathrm{c} = 10^{11.5}\,h^{-1}\mathrm{M}_\odot$. As shown by van den Bosch et al. (2003a) [see also Yang et al. (2003)], halos with masses $\sim M_\mathrm{c}$ have the minimum mass-to-light ratio, and thus are the most efficient in star formation. With $M_\mathrm{c} = 10^{11.5}\,h^{-1}\mathrm{M}_\odot$, $z_{1/2,\mathrm{t}_2}$ therefore indicates when star formation starts to prevail the halo assembly history. By definition, only halos more massive than M_c have a well-defined $z_{1/2,\mathrm{t}_2}$. This formation time is analogous to the formation time, z_N06, introduced by Neistein et al. (2006). According to Neistein et al. (2006), z_N06 is the time when the sum of the progenitors above a given minimum mass, reaches half of the present day halo mass.

4. $z_\mathrm{M/L}$: This is the redshift when the progenitors more massive than M_c have assembled a fraction f of $M_\mathrm{v}(0)$. Here the definition of f is based on the non-constant mass-to-light ratio of dark matter halos (Yang et al., 2003). For halos more massive than M_c, the mass-to-light ratio, $M_\mathrm{v}(0)/L$, follows a power law of $M_\mathrm{v}(0)$, with power-index $\gamma = 0.32$ (see Yang et al., 2003, table 1). We therefore have,

$$f = \alpha\frac{L}{M_\mathrm{v}(0)} = \frac{1}{2}\left(\frac{M_\mathrm{v}(0)}{M_\mathrm{c}}\right)^{-\gamma}, \tag{3.1}$$

where α is a constant, which is set so that $f = \frac{1}{2}$ for $M_\mathrm{v}(0) = M_\mathrm{c}$. Thus, $z_\mathrm{M/L}$ essentially reflects the time when a halo becomes capable of forming a

fraction of its total stellar mass. Note again that $z_{\rm M/L}$ can be defined only for $M_{\rm v}(0) > M_{\rm c}$.

5. $z_{\rm core,mb}$: This is the highest redshift at which the halo's main branch assembles a mass of $M_{\rm c}$. This formation time therefore indicates when a halo is able to host a relatively bright central galaxy.

6. $z_{\rm core,mp}$: This is the highest redshift at which the most massive progenitor has reached the mass $M_{\rm c}$. Note that for massive halos, $z_{\rm core,mp}$ may be different from $z_{\rm core,mb}$.

7. $z_{\rm vmax}$: This is the redshift at which the halo's virial velocity $V_{\rm v}(z)$ reaches its maximum value over the entire mass accretion history. According to equation (2.13), the value of $V_{\rm v}(z)$ is expected to increase (decrease) with time, if the time scale for mass accretion is shorter (longer) than the time scale of the Hubble expansion. Therefore, $z_{\rm vmax}$ indicates the time when the halo mass accretion transits from a fast accretion phase to a slow accretion phase (Zhao et al., 2003a; Li et al., 2007).

8. $z_{\rm lmm}$: Last major merger time. Here we define a major merger as the event when the mass ratio between the smaller halo and the main halo is no less than 1/3. The last major merger time is defined to be the one when the last major merger occurred on the main branch of an assembling halo.

Once the merging history of a halo is given, it is quite straightforward to determine the formation times defined above. The only exception is $z_{\rm lmm}$. Since the mass transfer from the merging halo to the main halo is a gradual process, a merger in general takes several snapshots to complete. Thus, if we used the halo mass increase in one time step, we would find only a small number of events in which the increase in the halo mass in a time step is large enough to be qualified as major mergers. In order

to circumvent this problem, we start from one snapshot, and trace the progenitors (including those of sub-halos) back to all the snapshots within a 1-Gyr interval. As long as there is a progenitor with mass exceeding 1/3 of the main-branch halo mass at the same time, a major merger event is identified. The choice of 1 Gyr is not crucial; our tests using 0.5 Gyr or 1.5 Gyr give almost the same results.

As illustration, we plot in Fig. 3.1 an actual merging history of a typical halo selected from the MS simulation, with all formation redshifts defined above marked. As one can see, the different definitions give very different values of the formation redshift, and they capture quite different aspects of the assembly history of a dark matter halo.

3.3.2 Formation time distribution in the MS

In Fig. 3.2 we show each of the formation redshifts as a function of halo mass. In each panel, the solid line represents the median in each mass bin, while the dashed lines represent 20% and 80% percentiles, respectively. As one can see, less massive halos generally have higher values of $z_{1/2,\rm mb}$, $z_{1/2,\rm t_1}$, $z_{\rm vmax}$ and $z_{\rm lmm}$ than massive ones, i.e. these formation redshifts have a negative correlation with halo mass. Since these formation times are defined in a self-similar manner, i.e., do not involve any particular mass scale, it is not surprising that they show a similar "bottom-up" trend, a consequence of hierarchical clustering. Nevertheless, $z_{1/2,\rm mb}$, $z_{1/2,\rm t_1}$, $z_{\rm vmax}$ and $z_{\rm lmm}$ still represent quite different epochs of halo formation history, which can be seen from their different values and scatter. For all halo masses, both $z_{\rm vmax}$ and $z_{\rm lmm}$ have scatter that is much larger than $z_{1/2,\rm mb}$, $z_{1/2,\rm t_1}$. This indicates that both $z_{\rm vmax}$ and $z_{\rm lmm}$ are more sensitive to the details of the halo assembly history.

On the other hand, the other four formation redshifts, $z_{\rm M/L}$, $z_{1/2,\rm t_2}$, $z_{\rm core,mb}$ and $z_{\rm core,mp}$, all show positive correlation with the halo mass, in the sense that more massive halos experience these events earlier. For massive halos, $z_{\rm core,mb}$ is lower than

$z_{\rm core,mp}$ and has larger scatter, which is due to the fact that for some massive halos, the most massive progenitors are not in the main branch. The trend is particularly strong for $z_{\rm M/L}$, $z_{\rm core,mp}$ and $z_{\rm core,mb}$. A halo of $10^{12}h^{-1}{\rm M}_{\odot}$ assembles a progenitor of mass $10^{11.5}h^{-1}{\rm M}_{\odot}$ typically at $z\sim 1$, while such a progenitor forms at $z\sim 5$ for halos with masses $\geq 10^{14}h^{-1}{\rm M}_{\odot}$. Since $z_{\rm M/L}$, $z_{\rm core,mb}$ and $z_{\rm core,mp}$ are the redshifts that characterize when a halo was able to host a relatively bright galaxy, the results shown here suggest that massive galaxies can form much earlier in massive halos than in low-mass halos. If star formation in these massive galaxies was eventually quenched as their stellar masses reach to some value, as is the case in the current AGN feedback model, or as they merge into a massive halo where radiative cooling becomes inefficient (e.g. Churazov et al., 2005; Croton et al., 2006; Cattaneo et al., 2008), one would expect that the star formation activity shifts with the passage of time from high-mass systems to the low-density field. This may be related to the observed "down-sizing" effect that massive galaxies in present-day clusters in general have old stellar populations with little star formation activities, and most star formation activities at the present time have shifted to low-mass systems. This shift is perfectly consistent with the hierarchical formation of dark matter halos, provided that there are some mechanisms that can quench star formation in massive galaxies. As we have shown, more massive halos indeed assemble their masses later, but the formation of massive galaxies can actually start earlier in their progenitors.

As mentioned before, the formation redshift $z_{1/2,{\rm t}_2}$ defined here is similar to the formation time $z_{\rm N06}$ introduced by Neistein et al. (2006). However, the halo mass-dependence we obtain here is quantitatively different from theirs. At the massive end, the results of Neistein et al. (2006) show continuous increase of the formation redshift with halo mass, while ours show a flattened relation. Note that Neistein et al. (2006) used the extended Press-Schechter formalism to generate halo merging trees, while

we obtain halo merging trees directly from N-body simulation. We suspect that the discrepancy may be due to the inaccuracy of the extended Press-Schechter formalism.

In Fig. 3.3 we show $z_{\rm core,mb}$ and $z_{\rm core,mp}$ versus $z_{1/2,\rm mb}$ for halos of different masses. For low-mass halos, $M_{\rm v} \sim 10^{12}h^{-1}{\rm M}_{\odot}$, $z_{\rm core,mb}$ and $z_{\rm core,mp}$ are very similar to $z_{1/2,\rm mb}$. However, for halos more massive than $10^{13}\,h^{-1}{\rm M}_{\odot}$, $z_{\rm core,mb}$ and $z_{\rm core,mp}$ are both higher than $z_{1/2,\rm mb}$. In particular, for halos with $M_{\rm v} \geq 10^{14}h^{-1}{\rm M}_{\odot}$, $z_{\rm core,mp} \sim 7$, without depending strongly on the half-mass formation redshift, $z_{1/2,\rm mb}$. This shows again that, for massive halos, the progenitors that can host massive galaxies can form much earlier than when the halos assemble most of their masses. Thus, although dark halos form hierarchically, star formation may appear "anti-hierarchical" at late epochs when many halos in which star formation was efficient have merged into massive systems.

3.4 Halo assembly bias scrutinized

3.4.1 The two-point correlation function

Autocorrelation (two-point correlation) function is often used to find the average excess probability of an object kind separated by distance r. Therefore, it is a useful tool to tell the clustering strength of the object ensemble on different scales. Define the dimensionless density fluctuation field at $\mathbf{x}$ as $\delta(x)$,

$$\delta(\mathbf{x}) = \frac{\rho(\mathbf{x}) - \bar{\rho}}{\bar{\rho}}, \tag{3.2}$$

where $\rho(\mathbf{x})$ is the density at $\mathbf{x}$ and $\bar{\rho}$ is the average density. The two-point correlation function of this density field can therefore be written as

$$\xi(\mathbf{r}) = \langle \delta(\mathbf{x})(\delta(\mathbf{x}+\mathbf{r})\rangle, \tag{3.3}$$

where the angle brackets mean it is an average over volume V. Since we can always express $\delta(\mathbf{x})$ as a sum over the wave modes,

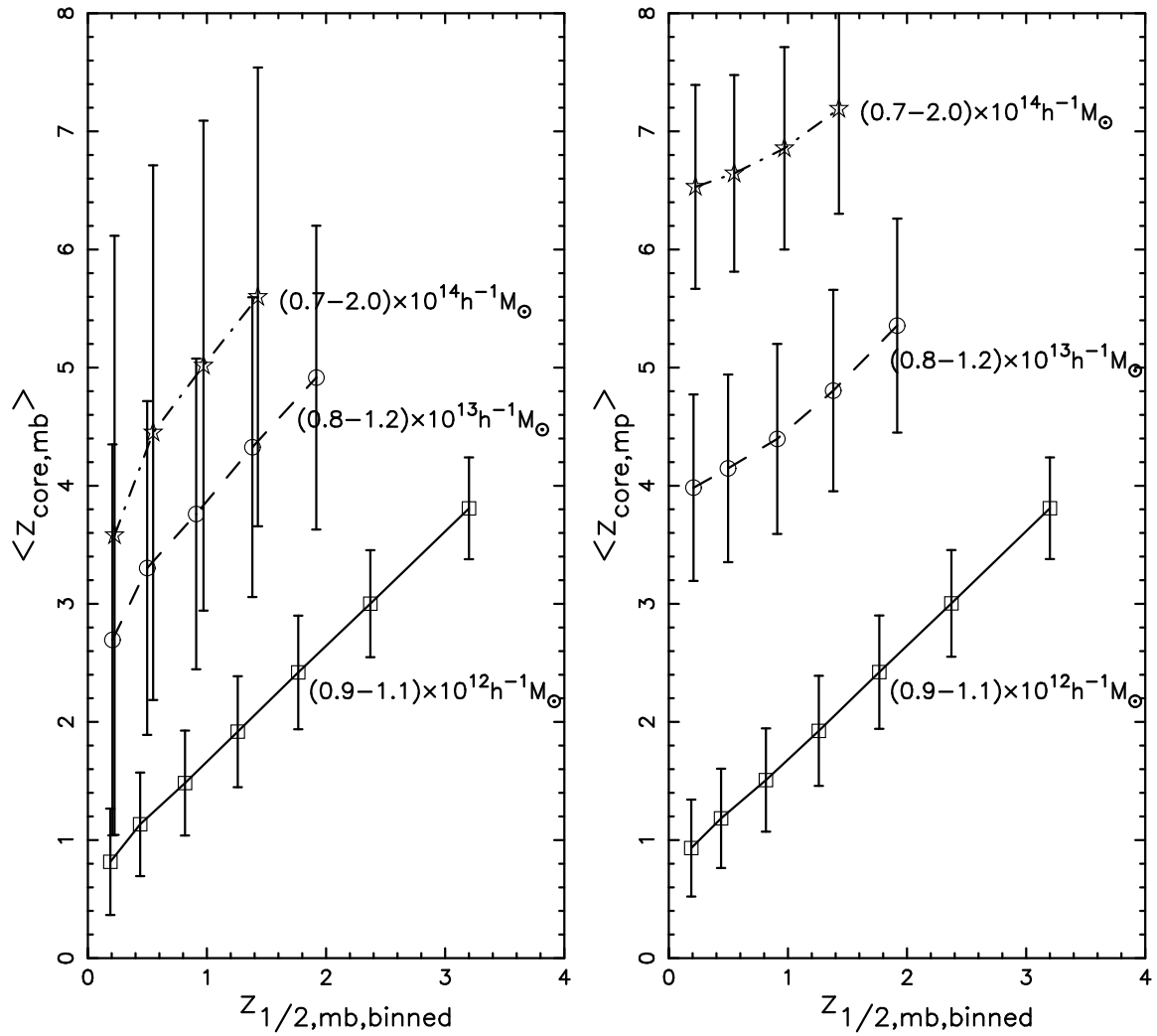

Figure 3.3. Compare $z_{\rm core,mb}$ and $z_{\rm core,mp}$ with $z_{1/2,\rm mb}$. Each line represents the result for halos with the mass marked aside. For each point, horizontal axis is the binned $z_{1/2,\rm mb}$, and vertical axis is the average $z_{\rm core,mb}$ or $z_{\rm core,mp}$ in the bin; error bars represent the standard deviation. More massive halos generally have lower $z_{1/2,\rm mb}$ but higher $z_{\rm core,mb}$ or $z_{\rm core,mp}$. Error bars in the right panel are generally smaller than in the left panel, indicating that the maximum progenitor could substantially deviate from the main branch, especially for massive halos at early time.

$$\delta(\mathbf{x}) = \sum \delta_{\mathbf{k}} e^{-i\mathbf{k}\cdot\mathbf{x}}, \tag{3.4}$$

and that $\delta(\mathbf{x})$ represents a real field, we then have

$$\xi(\mathbf{r}) = \left\langle \sum_{\mathbf{k}} \sum_{\mathbf{k}'} \delta_{\mathbf{k}} \delta^*_{\mathbf{k}'} e^{i(\mathbf{k}'-\mathbf{k})} e^{-i\mathbf{k}\cdot\mathbf{r}} \right\rangle. \tag{3.5}$$

Because of the periodic boundary condition, all the cross terms with $\mathbf{k} \neq \mathbf{k}'$ cancel out, subsequently we obtain

$$\xi(\mathbf{r}) = \frac{V}{8\pi^3} \int \left|\delta_{\mathbf{k}}\right|^2 e^{-i\mathbf{k}\cdot\mathbf{r}} \mathrm{d}^3k, \tag{3.6}$$

where $|\delta_{\mathbf{k}}|^2$ is the power spectrum. Under the condition of a sufficiently large volume and because the universe is isotropic, for which we have $P(k) = \langle|\delta_k|^2\rangle = |\delta_{\mathbf{k}}|^2$, the two-point correlation function reduces to

$$\xi(r) = \frac{V}{2\pi^2} \int k^3 P(k) \frac{\sin(kr)}{kr} \frac{\mathrm{d}k}{k}. \tag{3.7}$$

Therefore, the two-point correlation function of a density fluctuation field δ is the Fourier transform of the power spectrum $P(k)$.

In N-body simulations, once the spatial distribution of dark halos or galaxies is identified, one can either directly carry out pair-counting of the objects, or use Fourier transform of the fluctuation power spectrum to obtain the two-point correlation function.

3.4.2 Formation-time dependence of halo bias

Halos are biased tracer of the dark matter distribution. On large scales the two-point correlation function of dark halos, ξ_{hh}, is expected to be parallel to that of the mass, ξ_{mm}, so that one can write the bias factor b (equation 1.20) to indicate

the difference between the clustering strength of halos and that of the underlying dark matter. Analytical models and N-body simulations have shown that the halo bias factor depends strongly on halo mass. Halos more massive than M_* are more strongly clustered than the underlying mass (i.e. $b > 1$), while low-mass halos are less clustered than the mass (i.e. $b < 1$) (e.g. Mo & White, 1996; Jing, 1998; Sheth & Torman, 1999; Sheth, Mo & Torman, 2001; Mo & White, 2002). It has also been noted by Sheth & Torman (2004) that at fixed mass, halos in denser regions form slightly earlier. More recently, using very large N-body simulations, Gao et al. (2005) found that for halos with a fixed mass, the halo bias b actually depends strongly on the time when the halo first assembles half of its mass, i.e. on $z_{1/2,\rm mb}$, in the sense that halos with higher $z_{1/2,\rm mb}$ are more strongly clustered. This assembly bias is found to be stronger for halos of lower mass. Subsequent investigations using different simulations have confirmed this result (e.g. Wechsler et al., 2006; Harker et al., 2006; Zhu et al., 2006; Jing, Suto & Mo, 2007; Angulo et al., 2008a), and theoretical models have been proposed to understand the origin of such assembly bias (e.g. Wang, Mo & Jing, 2007; Sandvik et al., 2007; Hahn et al., 2007; Desjacques, 2008; Keselman & Nusser, 2007; Dalal et al., 2008).

Fig. 3.4 visually compares the relative spatial distributions of dark halos grouped in terms of the time, $z_{1/2,\rm mb}$, when the main progenitor of the halo acquires half of its final mass. Here we show the positions of the most-bound particle of each halo in the mass range $10^{11} - 10^{12}\,h^{-1}{\rm M}_\odot$, in a slice of $30\,h^{-1}$Mpc thickness through the MS. The top panel shows the positions of the 20% oldest halos, and the bottom panel shows the positions of the 20% youngest halos. It is clear that the oldest halos, which follow the cosmic web quite closely, are more strongly clustered than the youngest halos which show an almost uniform distribution.

In order to quantitatively study the formation-time dependence of halo clustering, we use a 3-dimensional Fast-Fourier-Transform (FFT) to derive the two-point corre-

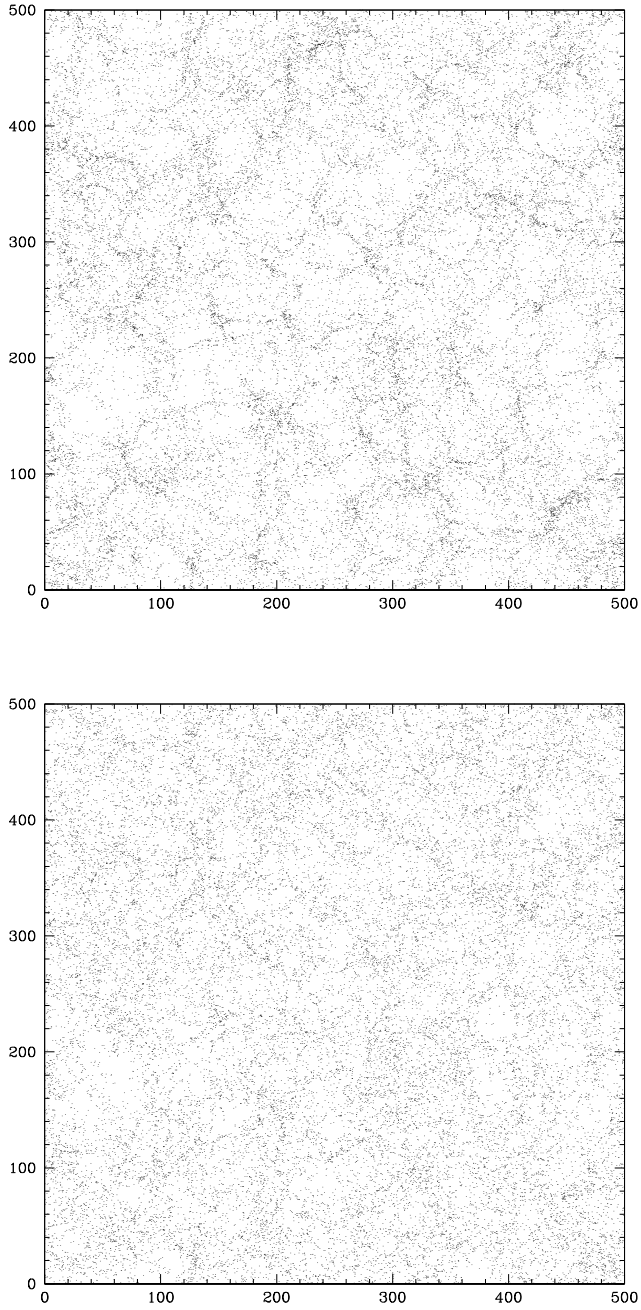

Figure 3.4. Spatial distribution of the oldest 20% and the youngest 20% halos randomly selected from the Millennium Simulation, according to the time when they assemble half of the final mass. Each side is marked in the unit of h^{-1}Mpc. All halos plotted here are in the mass range $10^{11} - 10^{12}\,h^{-1}\mathrm{M}_{\odot}$. Each panel represents a $30\,h^{-1}$Mpc slice through the Millennium Simulation . The upper panel shows the oldest 20% halos, while the lower panel shows the youngest 20% halos.

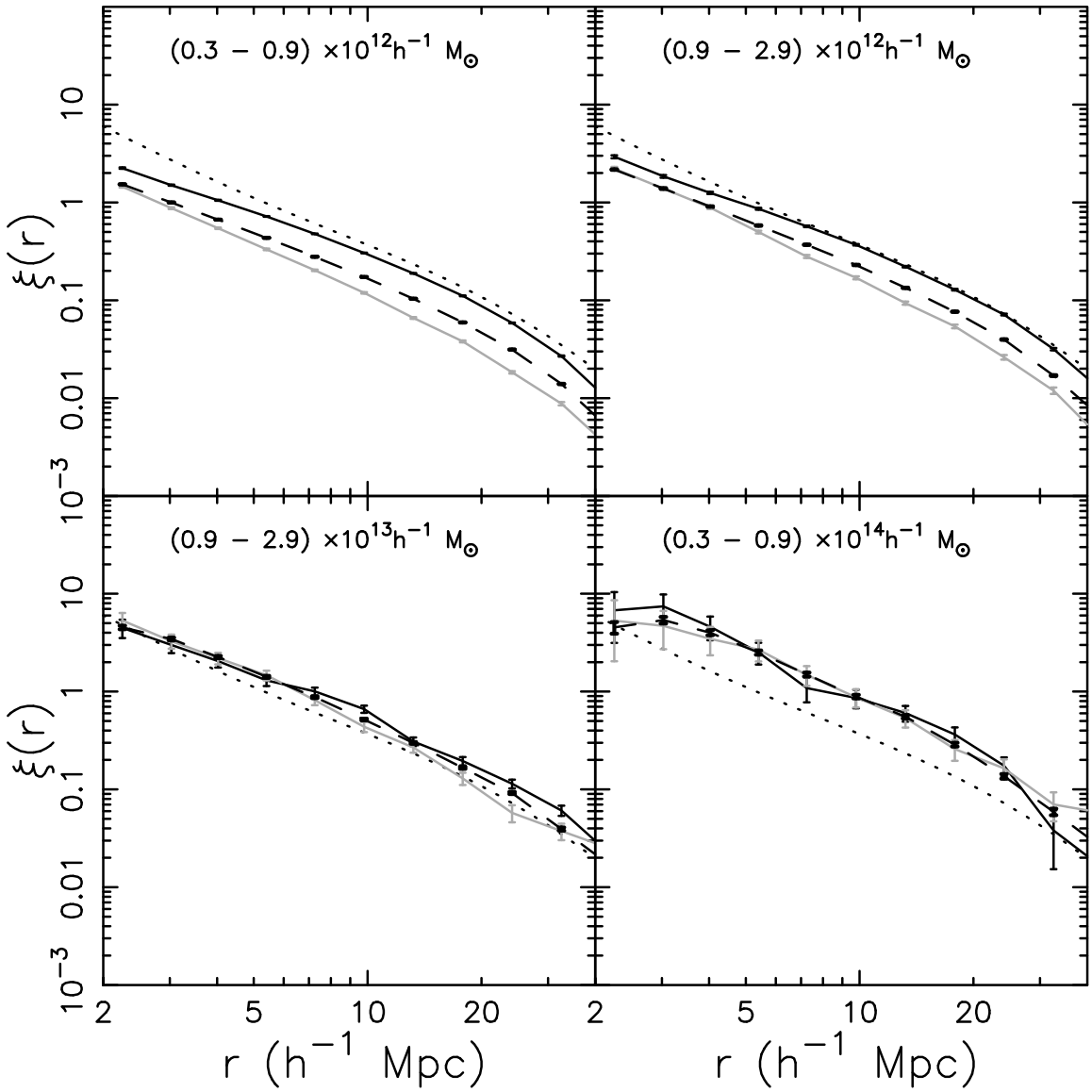

Figure 3.5. Two-point correlation function of halos with different $z_{1/2,\mathrm{mb}}$, with Poisson error bars. Each panel presents halos in different mass bins, as indicated. In each panel, dark solid line represents the two-point correlation function for halos with the highest 20% $z_{1/2,\mathrm{mb}}$, gray solid line represents the same function for halos with the lowest 20% $z_{1/2,\mathrm{mb}}$. The long-dashed line and the short-dashed line give the two-point correlation function of all halos in the given mass bin and that of the underlying dark matter, respectively.

lation function of dark matter halos as well as dark matter particles on large scales.

The procedure is as follows:

1. Use the Cloud-in-Cell method to distribute δ, the fluctuation in dark halo number density, on a cubic mesh with 512 grid points on each side.

2. Carry out the FFT to obtain the Fourier transform, $\delta_{\rm k}$, of such fluctuation, with *FFTW*.

3. Calculate the power spectrum of $\delta_{\rm k}$, $P(k)$.

4. Use inverse Fourier transform of $P(k)$ to obtain the two-point correlation function, $\xi(r)$.

Since our calculation only involves the halo two-point correlations on large scales (typically $r > 2\,h^{-1}$Mpc), we can safely ignore the small-scale inaccuracy of the FFT induced by the finite number of grids.

Fig. 3.5 shows the two-point correlation functions ξ for halos in different mass bins and with different $z_{1/2,\rm mb}$. Each panel compares the two-point correlation function for all the halos in the given mass range (as indicated) both with that of the underlying dark matter and with those for sub-samples made up of 20% oldest and 20% youngest halos. On large scales such as $r > 10\,h^{-1}$Mpc, the two-point correlation function of dark halos is parallel to that of the dark matter, regardless of halo mass. In general, dark halo two-point correlation function depends on halo mass, and its amplitude increases with halo mass. Since in the Millennium Simulation , $M_*(z = 0) \approx 6 \times 10^{12}\,h^{-1}{\rm M}_\odot$, we therefore confirm, from the long-dashed lines in Fig. 3.5, that, for halos with $M_{\rm v} < M_*$, they are less clustered than the dark matter, while for halos with $M_{\rm v} > M_*$, they are more clustered than the dark matter. Note that in the lower right panel, on small scale ($r < 3\,h^{-1}$Mpc), there is a slight drop in the amplitude of the halo two-point correlation function. This is caused by the exclusion effect of the positioning of massive halos. In addition, Fig. 3.5 also clearly demonstrates the formation time ($z_{1/2,\rm mb}$) dependence of halo clustering for fixed halo mass, as we have mentioned before. For halos with $M_{\rm v} = (0.3 - 0.9) \times 10^{12}\,h^{-1}{\rm M}_\odot$, the 20%

oldest (with highest $z_{1/2,\rm mb}$, dark solid line) halos are more strongly clustered than the 20% youngest (with lowest $z_{1/2,\rm mb}$, gray solid line) counterparts. For halos with $M_{\rm v} = (0.9 - 2.9) \times 10^{13}\, h^{-1}{\rm M}_{\odot}$, this difference becomes much smaller. For even more massive halos, such as those with $M_{\rm v} = (0.3 - 0.9) \times 10^{14}\, h^{-1}{\rm M}_{\odot}$, as shown in the right lower panel, there is no difference between these two lines. In fact, for such massive halos, Jing, Suto & Mo (2007) suggested that the youngest halos are more strongly clustered than the oldest ones, although the difference is small. However, due to the small box size of the Millennium Simulation ($500\, h^{-1}$Mpc), this trend is not observed in our work.

3.4.3 Halo assembly bias compared in terms of various formation times

In most of these earlier investigations, the assembly bias is analyzed in terms of the half-mass assembly time, $z_{1/2,\rm mb}$. However, as we discussed above, although $z_{1/2,\rm mb}$ may be a good quantity to characterize the formation of the main body of a halo, it does not characterize other aspects of the halo formation histories that may be more closely related to the formation of galaxies in halos. With the various formation times we have obtained, it is interesting to investigate how the clustering of halos depends on these different formation times.

Fig. 3.6 and Fig. 3.7 show, respectively, the age dependence of the two-point correlation functions for dark halos with $M_{\rm v} = (0.3 - 0.9) \times 10^{12}\, h^{-1}{\rm M}_{\odot}$ and $(0.9 - 2.9) \times 10^{13}\, h^{-1}{\rm M}_{\odot}$, in terms of the eight different formation times defined previously. Note that for given halo mass, some halos do not have all the eight formation times identified, due to the insufficient time resolution of the merging tree. To minimize the possible bias caused by this effect, before we further chronologically group dark halos according to a specific formation time, we require at least 80% of the halos within a given mass bin to have such formation time identified from their merging trees. For halos with $M_{\rm v} = (0.3 - 0.9) \times 10^{12}\, h^{-1}{\rm M}_{\odot}$, only 78% of them have a valid $z_{\rm lmm}$,

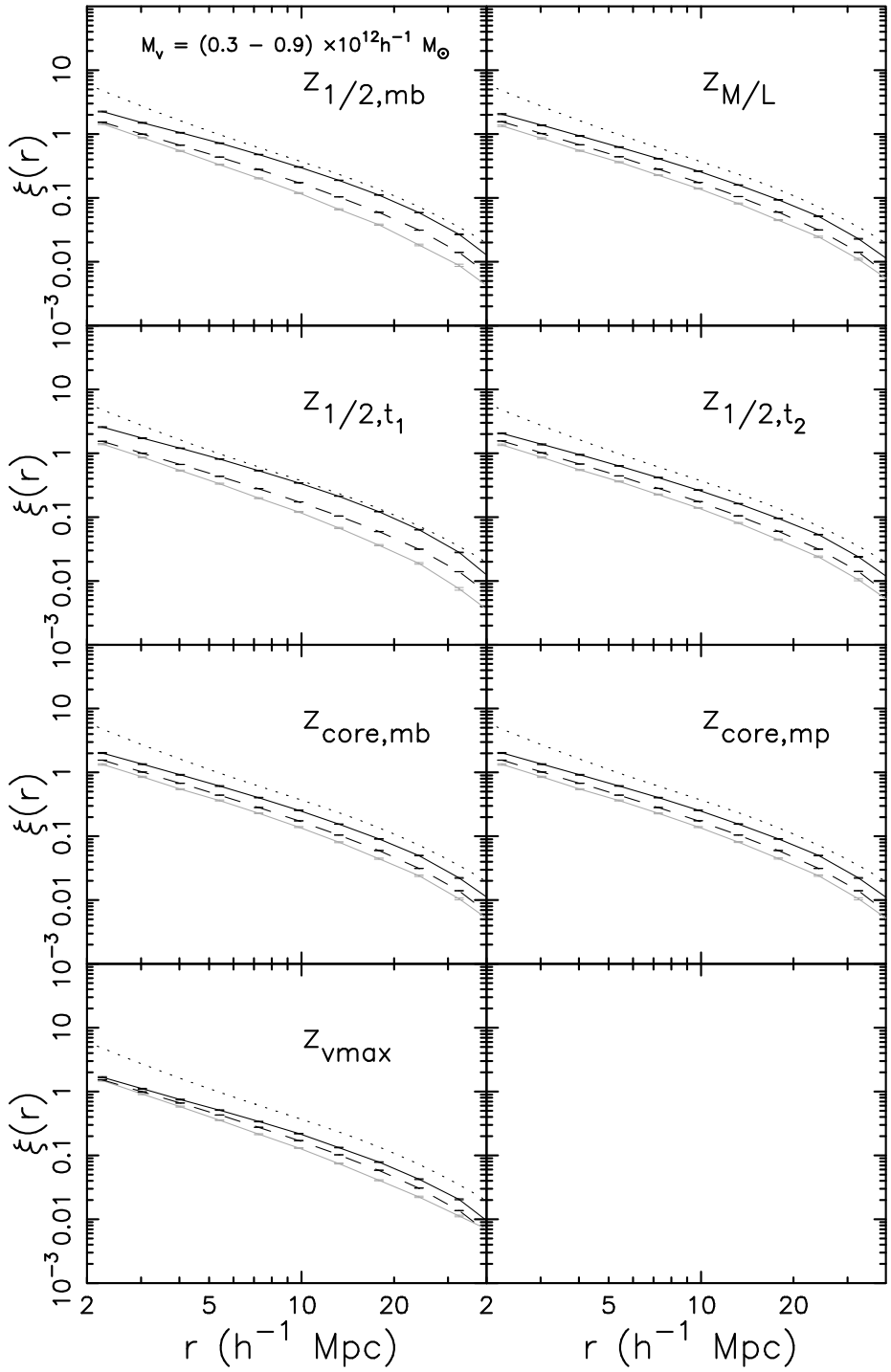

Figure 3.6. Age dependence of the two-point correlation functions for halos with $M_{\rm v} = (0.3 - 0.9) \times 10^{12}\ h^{-1}{\rm M}_{\odot}$, in terms of various formation times defined in the previous Section. All the lines are plotted in the same way as in Fig. 3.5. Note that there is no data for $z_{\rm lmm}$ because of the insufficient detection rate of this definition for halos with such relatively small mass.

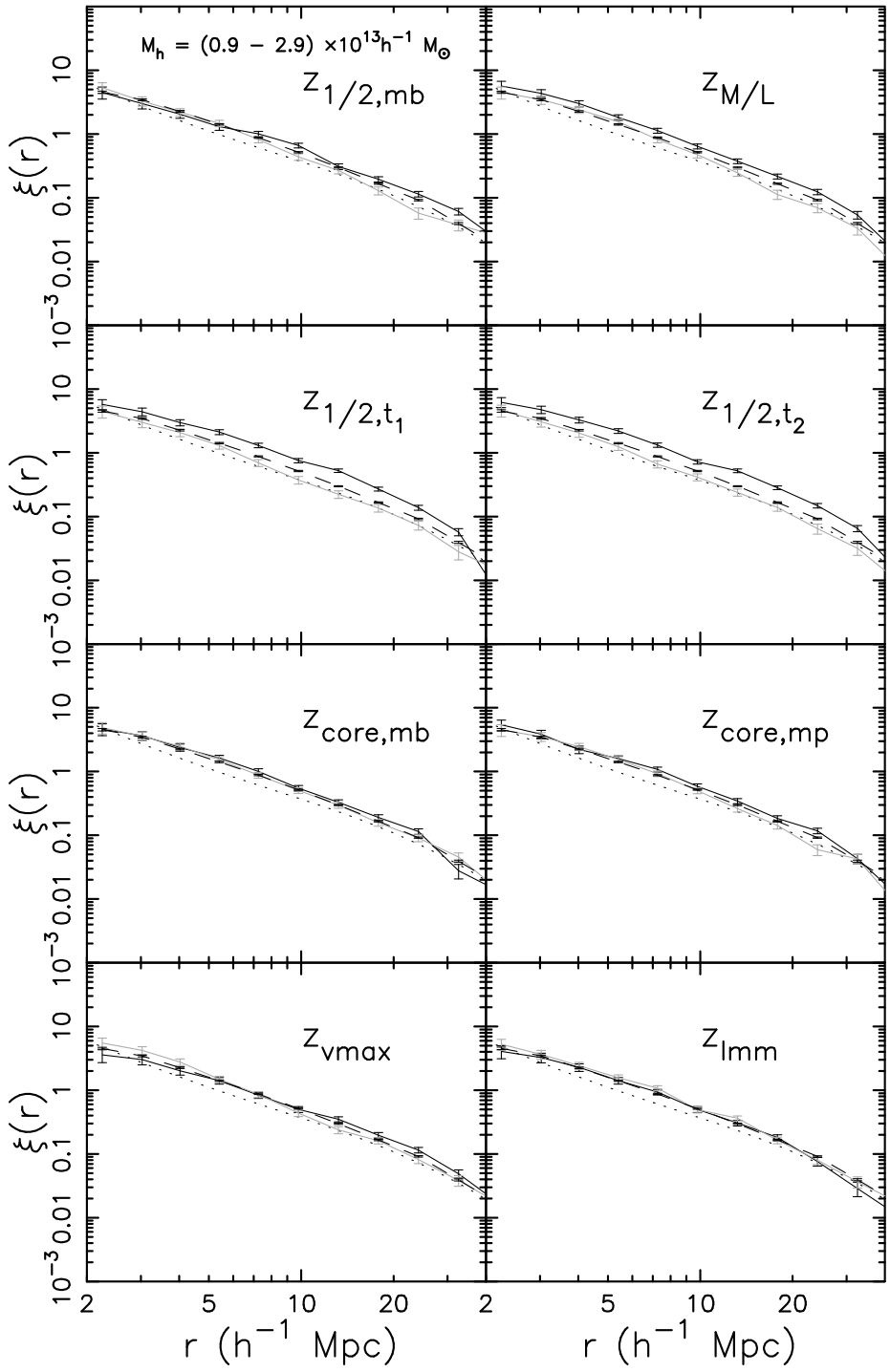

Figure 3.7. Same as Fig. 3.6, but for halos with $M_{\rm v} = (0.9 - 2.9) \times 10^{13}\, h^{-1}{\rm M}_{\odot}$.

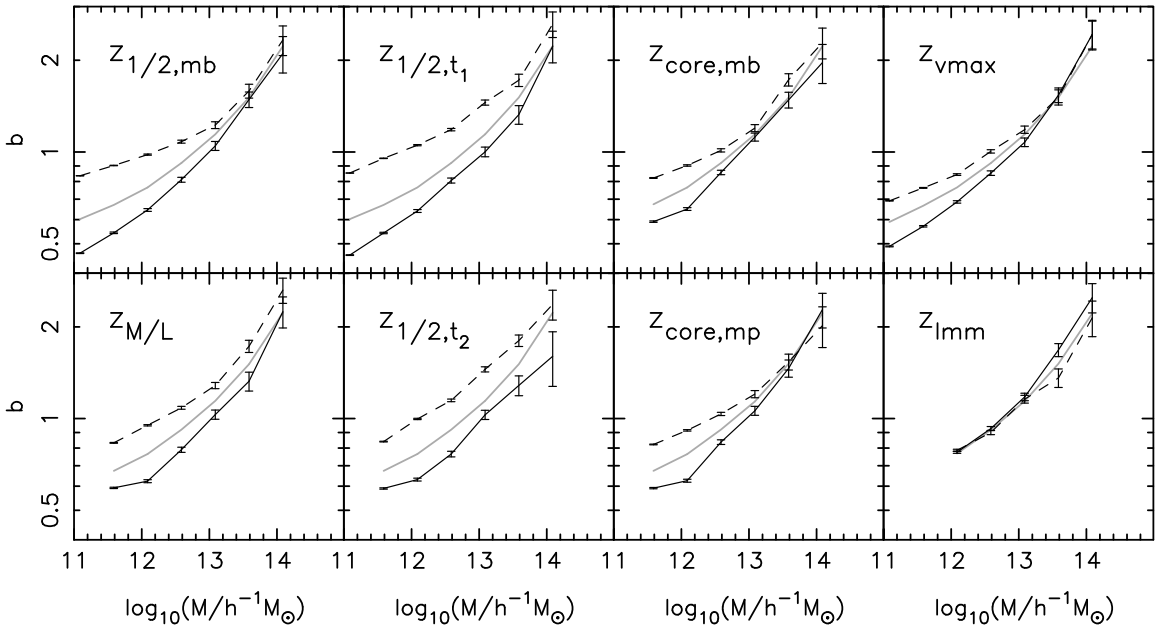

Figure 3.8. Age dependence of halo bias. Formation time used is indicated in each panel. Dashed lines are for oldest 20% halos while solid lines are for youngest 20% halos; the thick gray lines represent the bias of all the halos regardless of their ages. Error bars show the Poisson error.

therefore we did not plot the dependence of their two-point correlation functions on $z_{\rm lmm}$. A quick examination of Fig. 3.6 and Fig. 3.7 reveal the fact that for all the formation times defined, the age dependence of halo clustering weakens when halo mass increases. For a fixed halo mass, the strength of such dependence on different formation times also differs. To clearly demonstrate the difference, we investigate the bias factor, b (defined in equation [1.20]), of halos grouped according to their mass as well as formation times.

We estimate the halo bias b for a given halo mass, using the square root of the ratio of the two-point correlation function of halos and that of dark matter, averaged over data points in $8\,h^{-1}{\rm Mpc} \leq r \leq 30\,h^{-1}{\rm Mpc}$. This interval of r is chosen to ensure that the clustering is still in the quasi-linear regime where the linear bias relation (1.20) is a good approximation. In Fig. 3.8 we show how halo bias depends on the formation times we have defined for halos of different masses. The dashed line in each panel shows the bias factor of the oldest 20% population among all halos as a function

of halo mass, while the solid line shows the corresponding result of the youngest 20%. For comparison, we also show, as the grey line, the results for the total population without separation according to formation time. The error bar on each data point is estimated through the error propagation function based on the Poisson noise of each data point of the halo two-point correlation in $8\,h^{-1}\mathrm{Mpc} \leq r \leq 30\,h^{-1}\mathrm{Mpc}$.

As one can see, the bias factor of the total population increases with halo mass, and the increase is more rapid at the massive end. This result of mass-dependence of the halo bias factor is in good agreement with the results obtained in earlier investigations. In addition, for halos of a given mass, the bias factor also depends on the formation redshifts, although the strength of the dependence is not always the same for different definitions. The result based on $z_{1/2,\mathrm{mb}}$ is very similar to that obtained by Gao et al. (2005), even though the result here is based on "virial" halos while Gao et al. used FOF groups. With the exception of the case with z_{lmm}, where no significant age dependence is found for any halo masses, the strength of the age dependence in general decreases with increasing halo mass. For halos more massive than $10M_*$, we do not see any significant difference between halos of different ages. However, the noise here is too large due to the small number of systems available from the simulation, and so our data is not able to reveal the weak reversed trend, namely that the youngest halos are more strongly clustered, at the very massive end seen in some simulations (e.g. Wechsler et al., 2006; Jing, Suto & Mo, 2007; Wetzel et al., 2007; Angulo et al., 2008a). Note that Wechsler et al. (2006) were able to use relatively small simulations (with a box size around $100\,h^{-1}\mathrm{Mpc}$) to find a significant assembly bias for halos greater than M_*. However, their results were based on halos selected at different redshifts and on comparisons of halos with different masses (M_{v}) but the same M_{v}/M_*. Because M_* decreases with increasing redshift, their method dramatically increases the number of halos more massive than M_*. However, as shown in Jing, Suto & Mo (2007), the dependence of halo bias on halo assembly is weak for

massive halos identified at the same time. Our results for halos more massive than $10M_*$ are consistent with the results of Jing, Suto & Mo (2007).

In Fig. 3.8, the strongest age-dependence is seen in the cases of $z_{1/2,\rm mb}$, $z_{1/2,\rm t_1}$ and $z_{1/2,\rm t_2}$. Note that all these three formation redshifts are based on the properties of half of the final halo masses. This suggests that the assembly of the main parts of halos, especially the low-mass ones, may be affected significantly by large-scale environments. On the other hand, for the definitions that are based on the formation of a progenitor of a fixed mass, such as $z_{\rm core,mb}$ and $z_{\rm core,mp}$, the age dependence is weaker, particularly for halos with masses much higher than the progenitor mass, $M_{\rm c}$, used in the definition. As shown earlier, such progenitors in massive halos usually form at high redshifts where the large-scale environmental effects may not yet have time to develop. The age dependence based on $z_{\rm vmax}$ is also weaker than that based on $z_{1/2,\rm mb}$, presumably because the halo density involved in defining $z_{\rm vmax}$ is relatively high and so the mass assembly before $z_{\rm vmax}$ is less affected by the large-scale environment than that before $z_{1/2,\rm mb}$. Fig. 3.8 also shows that there is almost no dependence of the bias factor on $z_{\rm lmm}$, especially for halos smaller than M_*. This is consistent with the result of Percival et al. (2003), who found that, for halos with very recent major mergers (within the past 10^8 years), there is no detectable difference in the halo bias compared with all the halos of similar mass. Note that their simulations cannot provide very good statistics on massive halos because of the box sizes, which are no more than $200\,h^{-1}$Mpc. In our work, at the very massive end, there appears to be a hint that halos with recent major mergers are slightly more clustered. Wetzel et al. (2007) used the integrated correlation function to demonstrate that, for massive systems ($M_{\rm v} > M_*$), those with recent major mergers on average show a 5%-10% increase in bias, which is consistent with our result. However, in our work, the signal is still weak (based on the error bars) and we cannot rule out the possibility that it is due to statistical fluctuations. Our result suggests that major mergers may be controlled

Table 3.1. The relative bias, b', for halos of $10^{11.6}\,h^{-1}\mathrm{M}_\odot$ and $10^{13.1}\,h^{-1}\mathrm{M}_\odot$, respectively.

z_f	b'_old	b'_young	b'_old	b'_young
	($M_\mathrm{v} = 10^{11.6}\,h^{-1}\mathrm{M}_\odot$)		($M_\mathrm{v} = 10^{13.1}\,h^{-1}\mathrm{M}_\odot$)	
$z_{1/2,\mathrm{mb}}$	1.341 ± 0.008	0.809 ± 0.010	1.078 ± 0.027	0.925 ± 0.029
$z_\mathrm{M/L}$	1.231 ± 0.005	0.876 ± 0.005	1.134 ± 0.027	0.913 ± 0.029
$z_{1/2,\mathrm{t}_1}$	1.437 ± 0.008	0.819 ± 0.010	1.271 ± 0.024	0.883 ± 0.033
$z_{1/2,\mathrm{t}_2}$	1.247 ± 0.005	0.876 ± 0.005	1.261 ± 0.024	0.893 ± 0.034
$z_\mathrm{core,mb}$	1.214 ± 0.006	0.877 ± 0.006	1.051 ± 0.027	0.984 ± 0.030
$z_\mathrm{core,mp}$	1.231 ± 0.006	0.887 ± 0.006	1.065 ± 0.026	0.936 ± 0.029
z_vmax	1.140 ± 0.006	0.866 ± 0.005	1.038 ± 0.026	0.949 ± 0.029
z_lmm	n/a		1.010 ± 0.030	1.026 ± 0.030

by the properties of the local density field, without being strongly modulated by large-scale environments.

To better quantify the dependence of halo bias on the formation time, z_f, shown in Fig. 3.8, we define the relative bias for a sub-sample of halos with respect to all halos with the same mass M_v, as follows:

$$b'_{\mathrm{old/young},z_\mathrm{f}}(M_\mathrm{v}) = \frac{b_{\mathrm{old/young},z_\mathrm{f}}(M_\mathrm{v})}{b_\mathrm{all}(M_\mathrm{v})}, \tag{3.8}$$

where $b_{\mathrm{old/young},z_\mathrm{f}}(M_\mathrm{v})$ represents the bias derived from the sub-sample of the oldest/youngest 20% halos, and b_all represents the bias derived from all halos. The subscript "z_f" indicates the definition of the halo formation time. So defined, $b'_{\mathrm{old},z_\mathrm{f}}$ represents the relative halo bias for the oldest 20% halos and $b'_{\mathrm{young},z_\mathrm{f}}$ represents that for the youngest 20% halos, respectively. In Table 1 we list $b'_{\mathrm{old},z_\mathrm{f}}$ and $b'_{\mathrm{young},z_\mathrm{f}}$ for halos in two representative mass bins, centered at $10^{11.6}\,h^{-1}\mathrm{M}_\odot$ and $10^{13.1}\,h^{-1}\mathrm{M}_\odot$, respectively. Clearly, the level of assembly bias is significantly different for different definitions of the halo formation time.

The formation-time dependence of the halo bias presented above may have important implications. Previous studies suggest that the halo assembly bias may introduce observable effects in the large-scale clustering of galaxies (e.g. Neistein et al., 2006;

Croton et al., 2007). Using a large group catalogue constructed from the SDSS, Wang et al. (2008) found that groups with a redder central galaxy or a redder average color of member galaxies show stronger clustering (see also Yang et al., 2006). Because of the complexity of halo assembly, it is unclear which aspects of the halo formation history are more closely related to the colors of the galaxies that form in halos. By "shuffling" galaxies contained in halos of similar mass or formation time $z_{1/2,\rm mb}$, Croton et al. (2007) found, in their semi-analytical model, that the $z_{1/2,\rm mb}$-dependence of halo clustering can account at most half of the clustering bias of red galaxies. This implies that the difference in $z_{1/2,\rm mb}$ alone may not be sufficient to account for the colors of galaxies. This result is not surprising, because the assembly history of a halo is quite complicated and it is not expected that $z_{1/2,\rm mb}$ can provide a full characterization of such history. As demonstrated above, each of the eight formation times defined in this Chapter catches a different aspect of the halo formation history. It would be interesting to if see some combinations of these formation times are better correlated with the properties of galaxies. As we have shown, the assembly bias becomes insignificant for halos more massive than $10^{13}h^{-1}\,{\rm M}_\odot$ for most of the definitions of the assembly times. This may be the reason why the color-dependence of galaxy group clustering is significant only for groups less massive than $\sim 10^{13}h^{-1}\,{\rm M}_\odot$ (Wang et al., 2008).

Our results show that there is virtually no dependence of halo bias on $z_{\rm lmm}$, the redshift of last major merger. In the literature, it has been suggested that major merger may effectively shut off the star formation in a galaxy (e.g., Hernquist, 1989; Mihos & Hernquist, 1996; Springel, Di Matteo & Hernquist , 2005b; Kang et al., 2006), and hence $z_{\rm lmm}$ should be correlated with the current color of the central galaxy. However, if major mergers were the main reason to make a galaxy red, there would be no color-dependence of the clustering amplitude of galaxy groups, contrary to the observational results of Wang et al. (2008). This suggests that major mergers

alone cannot explain the red color of central galaxies. It is possible that the reddening of a central galaxy is the accumulative effect of a series of events triggered by, say, minor mergers, rather than a dominant major merger (e.g. Georgakakis et al., 2008).

Previous investigations have also shown that halo bias depends on on other halo properties, such as concentration and spin (Wechsler et al., 2006; Jing, Suto & Mo, 2007; Gao et al., 2007; Angulo et al., 2008a). Wechsler et al. (2006) found that for small halos ($M_{\rm v} \sim 10^{11.5}\,h^{-1}{\rm M}_{\odot}$), the halo bias depends more sensitively on the halo concentration parameter, c, in the sense that halos with fixed mass but with higher c are more strongly clustered. Since halo concentration is known to be correlated with halo accretion history (e.g. Wechsler et al., 2002; Zhao et al., 2003a; Lu et al., 2006), the concentration-dependence of halo bias is not surprising. If halo concentration is correlated with the time when a halo makes transition from the fast accretion regime to the slow accretion regime, we would expect a strong dependence of halo bias on $z_{\rm vmax}$, which roughly indicates this transition epoch (Li et al., 2007). However, such correlation is not perfect because halo concentration is not expected to be determined by a single formation time.

3.5 Discussion and Conclusions

In this Chapter we examine the complexity of dark halo mass assembly history using the MS and using different formation times to characterize the various aspects of halo formation histories. We find that, formation times defined according to the assembly of a fixed fraction of the halo final mass characterize the hierarchical clustering, in the sense that halos of higher masses on average have later formation time. On the other hand, formation times defined by the formation of progenitors of a fixed mass where star formation is expected to be efficient, clearly show "anti-hierarchical" behavior, in the sense that halos of higher masses have earlier formation time. If some feedback processes can terminate the star formation in these progenitors, we

would expect that galaxies in massive halos are redder, consistent with observation. We would also expect that the star-formation activities should shift with time from high-mass to low-mass halos, and so the observed "down-sizing" in star formation is not in conflict with hierarchical clustering.

As mentioned before, it has been long speculated that the color of a dark halo central galaxy is somewhat correlated with its merging history. If this is true then one might expect a strong correlation between the color of central galaxies and the host halo formation time, in particular, the last major merger time $z_{\rm lmm}$. To check whether this speculation is true, we use the publicly available semi-analytical galaxy catalogue based on the MS (Lemson et al., 2006) to explore the relationship between the color of central galaxies and the formation time of the host halos. The semi-analytical galaxy formation model has been thoroughly described in the paper by De Lucia et al. (2006). This model is one of the recent efforts that successfully explain why the massive systems should have the oldest stellar components. Fig. 3.9 plots the color-*halo-formation-time* relationship for 2000 randomly selected central galaxies. Vertical axis denotes the $B-V$ color of the central galaxies of dark halos with $M_{\rm v} \approx 10^{12}\ h^{-1}{\rm M}_{\odot}$, and the horizontal axis denotes the formation times of the corresponding host halos. The apparent two distinct groups of galaxies are the so-called red-sequence galaxies and blue-sequence galaxies, indicating the bimodality in galaxy color distribution. For each group of galaxies, although the host halos of redder ones do appear to form earlier in terms of most definitions of the halo formation time, the formation times of host halos are clearly not the deterministic factor that causes the color bimodality. In particular, it seems the color of central galaxies has nothing to do with the last major merger time of the host halos. Note that the results shown here should depend strongly on the galaxy formation model considered. Further investigation reveals that, in the galaxy formation model used here, the color of central galaxies is almost completely determined by the strength of

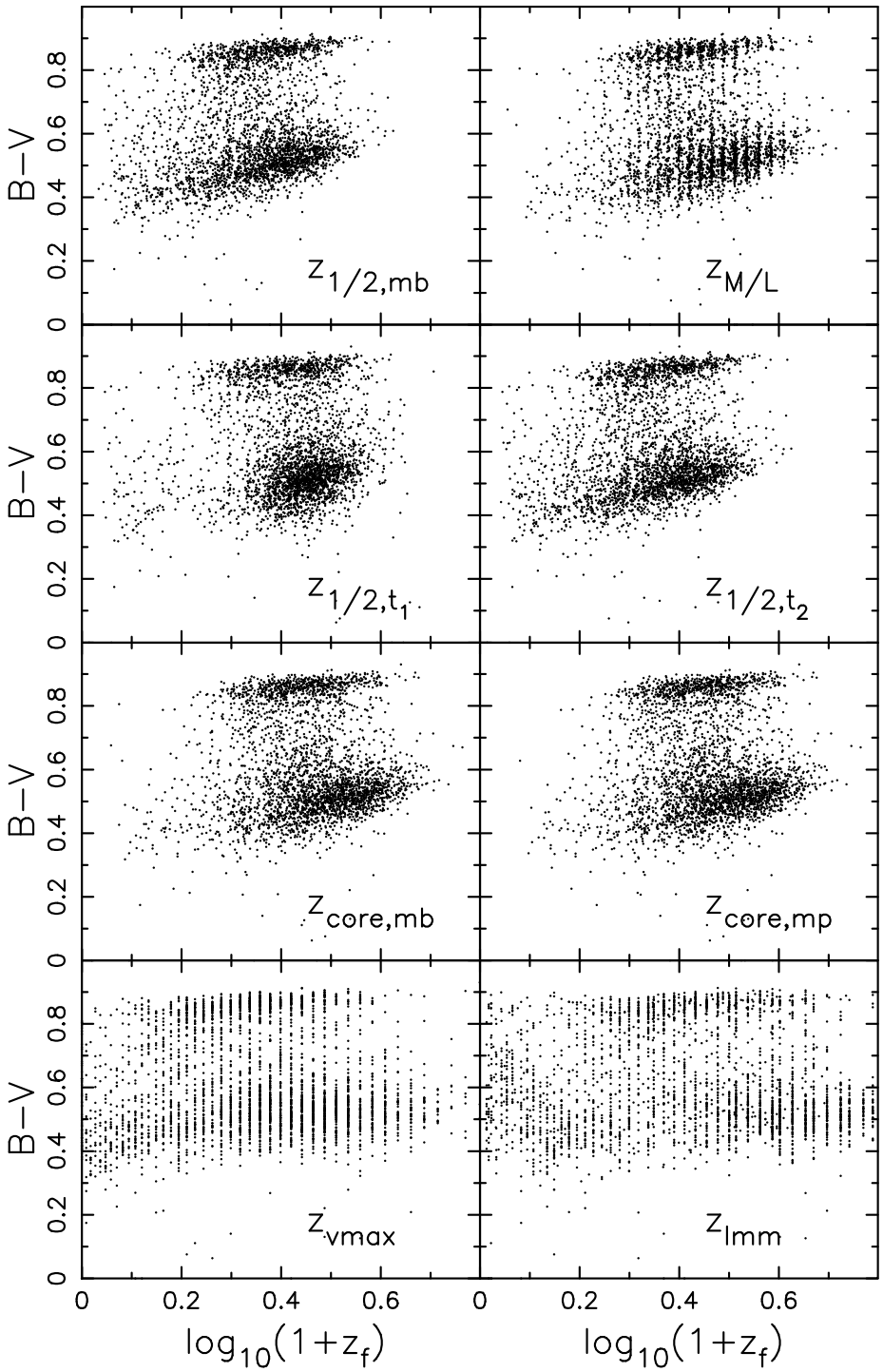

Figure 3.9. B-V color of dark halo central galaxies v.s. the formation times of the host halos, for halos with $M_{\rm v} = (0.9 - 1.1) \times 10^{12}\, h^{-1}{\rm M}_{\odot}$. The plot is partially based on the semi-analytical model by De Lucia et al. (2006). Points are from 5% randomly selected central galaxies satisfying the above criteria.

the AGN feedback from the massive central black holes, which gradually accumulates the mass throughout the whole merging history, rather than during a single event characterized by one halo formation time.

We also study how the clustering of dark matter halos depends on the various formation times defined. We find that halo bias shows a strong positive correlation with halo mass, in good agreement with earlier results. For fixed halo mass, our results confirm a positive correlation between halo formation time, $z_{1/2,\mathrm{mb}}$, and halo clustering strength. The strength of this dependence increases with decreasing halo mass. For halos more massive than $10^{14}\ h^{-1}\mathrm{M}_{\odot}$, we do not find a clear reversal of the assembly bias. In general, for halos less massive than $10^{14}\ h^{-1}\mathrm{M}_{\odot}$, there is a positive correlation between the various formation times defined and halo clustering strength, with the correlation being stronger for lower halo masses. However, the correlation amplitude is quite different when different formation time is considered. The strongest age dependence of halo clustering is seen on $z_{1/2,\mathrm{mb}}$, $z_{1/2,\mathrm{t}_1}$ and $z_{1/2,\mathrm{t}_2}$. There is virtually no age dependence of halo clustering on halo last major merger time, z_{lmm}, and the dependence on $z_{\mathrm{M/L}}$, $z_{\mathrm{core,mb}}$, $z_{\mathrm{core,mp}}$, z_{vmax} is moderate. If the typical age of stars in a halo is correlated with halo assembly history in some way, then halos with fixed mass but containing redder member galaxies are expected to be more strongly clustered, and this color-dependence is expected to be weaker for more massive systems. This is consistent with recent observations. However, since there is virtually no dependence of halo clustering on z_{lmm}, the typical color of galaxies in a halo is not expected to be determined by the last major merger time of its host halo.

CHAPTER 4

MASS DISTRIBUTION AND ACCRETION OF SUB-HALOS

4.1 Introduction

Besides the properties we have studied previously, halo-halo mergers and the subsequent evolution of resultant sub-halos have been of great interests recently, in both analytical models and N-body simulations (Sheth, 2003; Gao et al., 2004a; De Lucia et al., 2004; van den Bosch et al., 2005; Giocoli et al., 2008a,b; Angulo et al., 2008b; Wetzel et al., 2008). Since galaxies are believed to initially reside at the center of and merge along with dark halos, these events are therefore highly correlated with galaxy evolution. In this scenario, mergers play a transitional role in converting central galaxies into satellite galaxies in the post-merger halos. They may also trigger the evolution of various galactic properties, such as the morphology, luminosity, color and spatial distribution (Barnes & Hernquist, 1996; Naab & Burkert, 2003; Hopkins et al., 2006; Maller et al., 2006; De Lucia & Blaizot, 2007; McIntosh et al., 2008).

Although, from a phenomenological point of view, some observational statistics based on current sub-halo mass model matches well with the observations (Mandelbaum et al., 2006; Kim et al., 2008), our understanding of galaxy formation still needs improvements due to the insufficient modeling of various physical processes, such as cooling, feedback, and merging history. It is also ambiguous how exactly post-merger galaxies are linked with pre-merger dark halos, because once a merger happens, the subsequent tidal forces and dynamical friction will cause the sub-halo, formerly a host halo, to loose mass and possibly become completely destroyed. This process gives rise

to several possible fates of the stellar components of the galaxies that merge along with the sub-halos (Yang et al., 2009).

Despite the details of how a satellite galaxy evolves in a denser environment, it is always important to quantify the mass function of the associated sub-halos at the time of merging, for several reasons. First, previous studies have suggested that mass is a key factor of various properties of dark halos, such as density profile (Navarro, Frenk & White, 1997), sub-halo population (Gao et al., 2004a), clustering property (Mo & White, 1996). Secondly, and more importantly perhaps, different approaches such as the halo occupation distribution (HOD) or similar models (e.g. Berlind & Weinberg, 2002; Zheng et al., 2005; Tinker et al., 2005; Wang et al., 2006) and conditional luminosity function (CLF) model (Yang et al., 2003; van den Bosch, 2007), which base their galaxy statistics on host halo mass, have resulted in reliable descriptions of the distribution of galaxies. Therefore, to better understand the link between sub-halo mergers and post-merger galaxies, some important issues need to be addressed. For example, based on extended Press-Schechter formalism and direct N-body simulations, van den Bosch et al. (2005) and Giocoli et al. (2008a) found that the unevolved sub-halo mass function (USMF) of the progenitors that merged into halo main branch follows a universal form. Their findings are useful because the results can be linked to the number of central galaxies that may have turned into satellite galaxies through *direct* merger into a final halo. However, this information is insufficient to account for *all* incidences of mergers during the entire galaxy assembly history, because the hierarchical nature of CDM model suggests that sub-halos were independent host halos before the time of accretion, and it is likely they inherit the generic sub-halo population by the time when they became sub-halos. Thus, to investigate the possible effects on the statistics of galaxy properties from the angle of sub-halos, one needs to further clarify two questions. First, is the USMF really generic (i.e., does it depend on other quantities such as redshift than halo mass)? Second, what

may be the difference if one takes into account the inherited sub-halo statistics of a sub-halo itself? Today, high resolution N-body simulations provide a direct way to measure the merger statistics of dark halos to relatively high redshift with a good mass resolution.

In this Chapter, we take advantage of a large N-body simulation and its distinguished sub-halo statistics to answer the questions mentioned above. This Chapter is organized as follows. In section 4.2 we give a brief overview of the simulation and the algorithm used to construct the halo merging tree. In section 4.3 we describe in detail how to use the merging tree to identify halo-halo mergers during the halo accretion history, and further derive the unevolved mass function of the sub-halos characterized in several different ways. In section 4.4 we study the accretion time of sub-halos and mass function of sub-halos accreted at given redshift. Lastly in section 4.5 we summarize our results and discuss the implications.

4.2 The Data

In this Chapter we again use the "Millennium Simulation" (MS) carried out by the Virgo Consortium (Springel et al., 2005a). We have used the same simulation data in Chapter 2 to study the age dependence of dark halo spatial distribution. We refer the reader to that chapter for details of this simulation. In what follows, we always use "virial mass" (introduced previously), as the halo mass. Since our study in this Chapter does not involve any specific formation time that depends on the virial velocity and/or virial radius, we therefore adopt the notation $M_{\rm h}$ instead of $M_{\rm v}$ to avoid confusion. In order to ensure robustness and completeness of our sub-halo analysis, we only use sub-halos with masses above a mass limit $M_{\rm lim} = 2\times10^{10}h^{-1}{\rm M}_{\odot}$. This mass limit is slightly higher than the re-simulated halos used by Giocoli et al. (2008a), but the simulation volume of the MS allows us to use many more halos to gain better statistics.

As we have mentioned before, the halo merging trees in the MS are constructed on the basis of sub-halos. In the literature, merging history trees based directly on FOF halos are widely employed to study the mass accretion history of dark halos. The "sub-halo"-based linking algorithm used in the MS, however, has special advantages over the FOF merging tree in the study of the evolution of sub-halos. By definition, this algorithm enables a more clear-cut history tracer of sub-halos (see e.g., Fakhouri & Ma, 2008).

4.3 Unevolved Sub-halo Mass Functions

Mergers are important events during the lifetime of a galaxy. If there exists a one-to-one correspondence between a central galaxy and a host halo, then all galaxies are initially central galaxies at some high redshift in the hierarchical scenario of structure formation. Subsequent halo mergers play an crucial role in galaxy evolution, in the sense that a central galaxy will be formally transferred into a satellite galaxy and perhaps evolve passively afterwards without a significant amount of star formation. As mentioned before, galaxy properties may be highly correlated with their host halo mass. Understanding the mass function of the progenitors of the sub-halos at the time of accretion is a key step in understanding the formation and evolution of satellite galaxies. In what follows we will refer the mass function of sub-halos at accretion as the unevolved sub-halo mass function (USMF), which reflects the fact that the sub-halos at the times of accretion have not yet been processed by dynamical effects, such as tidal stripping. In the rest of this section, we will discuss the USMF of sub-halos in the following three categories:

1. In Sub-section 4.3.1, we focus on sub-halos on the main branch of the merging tree, i.e., progenitors that directly merge with the main progenitors of dark halos. The same case has been studied by Giocoli et al. (2008a).

2. In Sub-section 4.3.2, we include all sub-halos that have merged into the entire merging tree of a dark halo.

3. Finally in Sub-section 4.3.3, we focus on sub-halos that are directly identifiable in the present-day halos, the so-called "survived sub-halos".

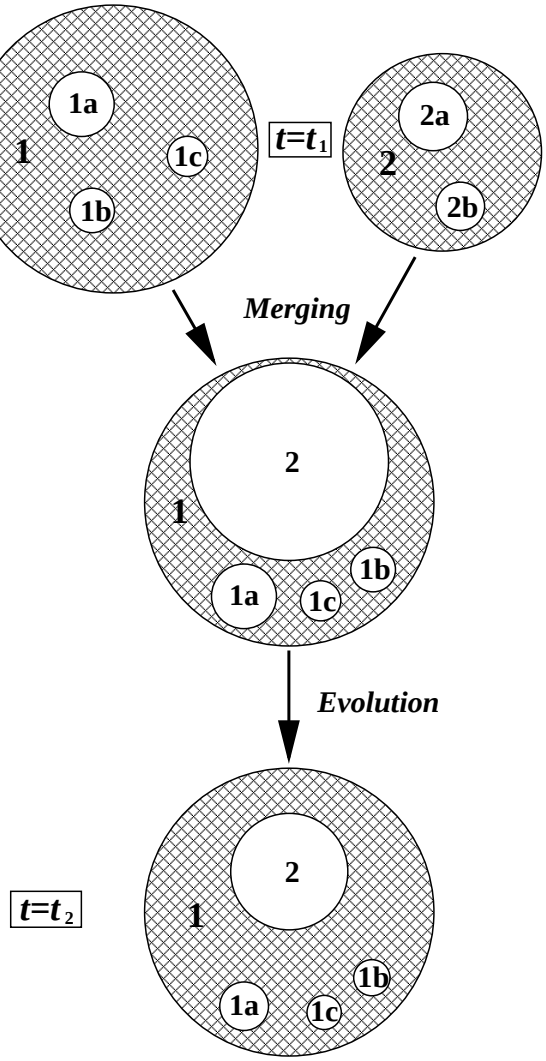

Figure 4.1. A schematic demonstration of the difference between main branch sub-halos and all sub-halos (figure courtesy van den Bosch et al. (2005)).

Fig. 4.1 graphically illustrates the difference between the sub-halos in these three categories: main branch sub-halos (category 1), all sub-halos in the merging tree (category 2), and survived sub-halos (category 3). At $t = t_1$ (or equivalently $z = z_1$),

halo 1 (with three sub-halos) and halo 2 (with 2 sub-halos) merge. Since $M_1 > M_2$, we consider halo 1 as the main progenitor, and halo 2 as the main branch sub-halo. Subsequently we count one incidence of main branch sub-halo merger (at $t = t_1$). Since we know that sub-halo, say, 2a, of the five sub-halos (1a, 1b, 1c, 2a and 2b) at $t = t_1$, merged with halo 2 at an earlier time t_{2a} ($t_{2a} < t_1$), we will count the sub-halo merger that happened at t_{2a} toward category 2. Apparently, for the five sub-halos at $t = t_1$, we will have up to five more incidences in category 2 than in category 1. At the present time ($t = t_2$), sub-halos 2a and 2b were tidally destroyed, and the remaining sub-halos in host halo 1 are sub-halos 2, 1a, 1b and 1c, with mass smaller than their mass at time of merging. For these four sub-halos, we refer to them as "survived" sub-halos.

4.3.1 Main branch sub-halos

To construct the halo main branch, we start with the final halo at a given redshift $z_{\rm h}$ (in this Chapter, $z_{\rm h} = 0$ unless otherwise mentioned), and trace its most massive progenitor (the main progenitor) in the adjacent snapshot at higher redshift. We then repeat this procedure for the main progenitor till the progenitor mass is too small to be resolved. During this procedure, we also search the indices of all other progenitors that have directly merged into the main progenitor. If a progenitor was an independent halo before merger, we register its mass as well as the redshift at which it was accreted (the redshift information will be used later to study the mass function of sub-halos at given accretion time). This method eliminates cases where progenitors were already sub-halos of other more massive progenitors at the time of merging. With the information collected in this way, we are able to construct the USMF of main branch sub-halos. The results are plotted in Fig. 4.2 for host halos of different masses (as indicated).

We adopt the same functional form proposed by Giocoli et al. (2008a) to fit the simulation results. Given a final halo (host halo) mass $M_{\rm h}$ and a sub-halo mass *at accretion*, $M_{\rm acc}$, the USMF, F, is written as

$$\begin{aligned} F\left(\frac{M_{\rm acc}}{M_{\rm h}}\right) &= \frac{{\rm d}N}{{\rm d}\ln(M_{\rm acc}/M_{\rm h})} \\ &= a\left(\frac{M_{\rm acc}}{M_{\rm h}}\right)^{b} \exp\left[-c\left(\frac{M_{\rm acc}}{M_{\rm h}}\right)^{d}\right], \end{aligned} \tag{4.1}$$

where N stands for the number of sub-halos that were accreted and a, b, c, d are fitting parameters. At the low-mass end ($M_{\rm acc}/M_{\rm h} \to 0$), this is a power-law, while at high-mass end ($M_{\rm acc}/M_{\rm h} \to 1$), the function decreases exponentially with $(M_{\rm acc}/M_{\rm h})^d$. If the other parameters are fixed, a represents the overall amplitude, b indicates the low-mass end power-index, c indicates the transitional point where the curve changes its shape, and d determines the steepness of the exponential decline. However, different combinations of parameters can result in F with similar shapes within the mass range probed here ($\log_{10}[M_{\rm acc}/M_{\rm h}] \in [-4, 0]$). Therefore we do not intend to fit the result for each host-halo mass bin separately. Instead, we use all the mass bins to obtain an overall fit, which is shown as the solid line in the last panel. For comparison the best-fit USMF obtained from Giocoli et al. (2008a) is shown in each panel of Fig. 4.2 as the dashed curve.

Our results show an overall excellent agreement with the result by Giocoli et al. (2008a). The values of the fitting parameters we obtain are very close to what were proposed by Giocoli et al. (2008a), with only slight difference. For instance, we find the low-mass end power-law index $b = -0.76$, which is a slightly shallower than their -0.8. Our slope is chosen so as to reconcile the slightly higher "shoulder" found in the mass range $\log_{10}(M_{\rm acc}/M_{\rm h}) \in [-1.5, -0.5]$. Note that for halos with $M_{\rm h} = 10^{12.1}\,h^{-1}{\rm M}_{\odot}$, we do not have data points that cover far enough into the power-law part.

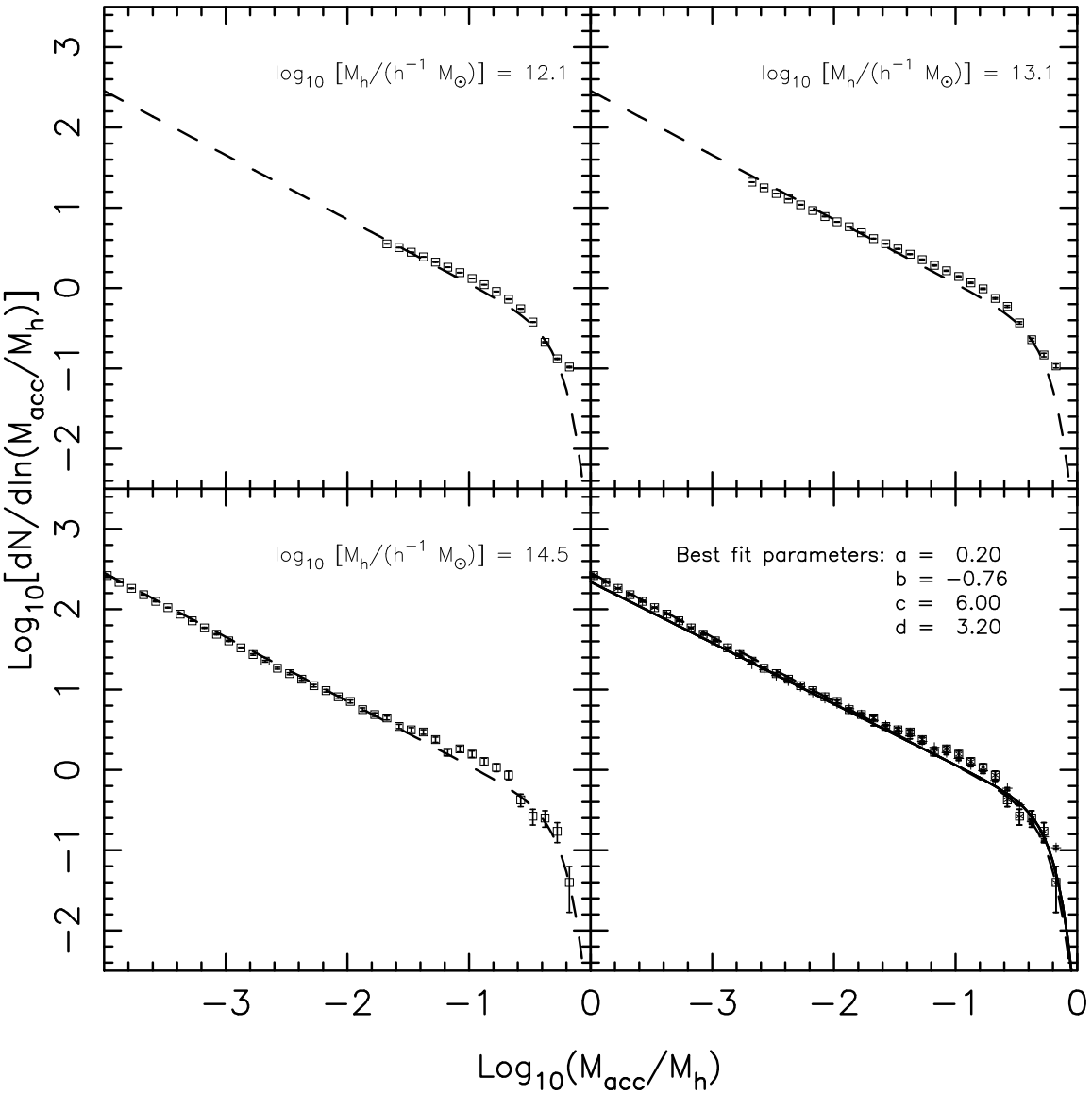

Figure 4.2. The USMF of main branch sub-halos. The *upper two panels and the lower left panel* show the USMF of $z_{\rm h} = 0$ halos with $M_{\rm h} = 10^{12.1}, 10^{13.1}, 10^{14.5}\,h^{-1}{\rm M}_{\odot}$, respectively. Data points are the average over all halos with mass $M_{\rm h}$, error bars represent the standard error of the average. For reference, in each panel we also plot, with identical dashed lines, the best-fit USMF from Giocoli et al. (2008a). In the *lower right panel*, we summarize all the data from previous panels, and plot equation (4.1) (in thick solid line) with an empirical set of parameters (as indicated in the panel) which provides a universal fit to all of our data.

We also estimate the USMF for host halos identified at redshift $z_{\rm h} = 1$, and the result is shown in Fig. 4.3. Although the cosmic density field has evolved significantly during the time interval from $z_{\rm h} = 1$ to $z_{\rm h} = 0$, the USMF at $z_{\rm h} = 1$ has the same

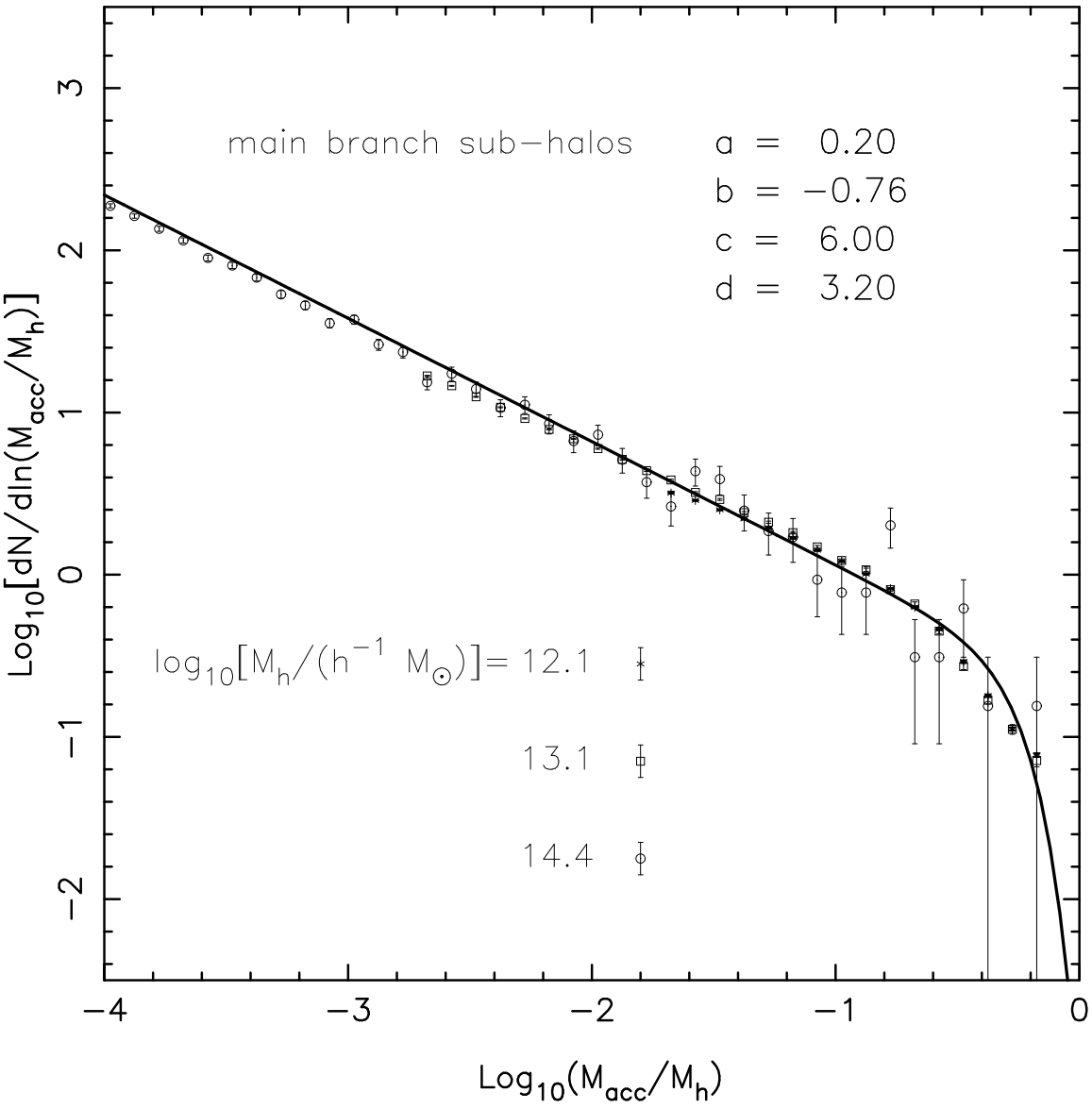

Figure 4.3. The USMF of main branch sub-halos for host halos at $z_{\rm h} = 1$. Different symbols represent the data points for host halos with different masses (as indicated), and the solid line is the universal fits we have obtained from $z_{\rm h} = 0$ halos.

form as that for $z_{\rm h} = 0$ halos. All these suggest that the USMF of the main branch sub-halos has a universal form, independent of host halo mass and the redshift at which the host halo is identified.

4.3.2 All sub-halos on the merging tree

The merging history of a dark halo is in general quite complex. At lower redshifts, after a halo has assembled its main body, mergers may primarily happen on the main branch. However, at higher redshift, when a large fraction of the final halo mass was still part of smaller progenitors, mergers that take place on the sub-branches of the merging tree can no longer be neglected. In addition, the sub-halos that merge into the sub-branches may still present at the time when their host halos merge into larger halos. Although it is likely that most sub-halos that merge at high redshift may have already been dissolved by dynamical friction and tidal stripping by the time when the final halo assembles, the satellite galaxies that merged along with them may be more resistant to these dynamical effects. Therefore, it is interesting to investigate the statistical properties of these merging events.

In order to quantify the USMF of all sub-halos in the entire merging tree of a halo, we start from the final host halo and trace back to all its progenitors that have ever merged as a sub-halo, regardless whether the merger takes place on the main branch or sub-branches. Once we found a merger between two independent halos, we register the mass of the sub-halo and the time of merger.

Fig. 4.4 shows the USMF of all sub-halos in the halo merging tree, in the same way as Fig. 4.2 for sub-halos in the main branch. Interestingly, equation (4.1) still provides a good description of the USMF in this case, although the fitting parameters are different from those for the sub-halos in the main branch (see the solid line in the lower right panel and the values of the fitting parameters listed in the panel). Comparing the results here with those shown in Fig. 4.2, we see that the overall amplitude here is higher, due to the fact that sub-halos on sub-branches are also included. In addition, the increase in the amplitude is much larger for low-mass sub-halos than for massive ones, giving rise to a steeper power-law slope in the low-mass end – compare the data points in each panel with the dashed curve that shows the fitting result of the USMF

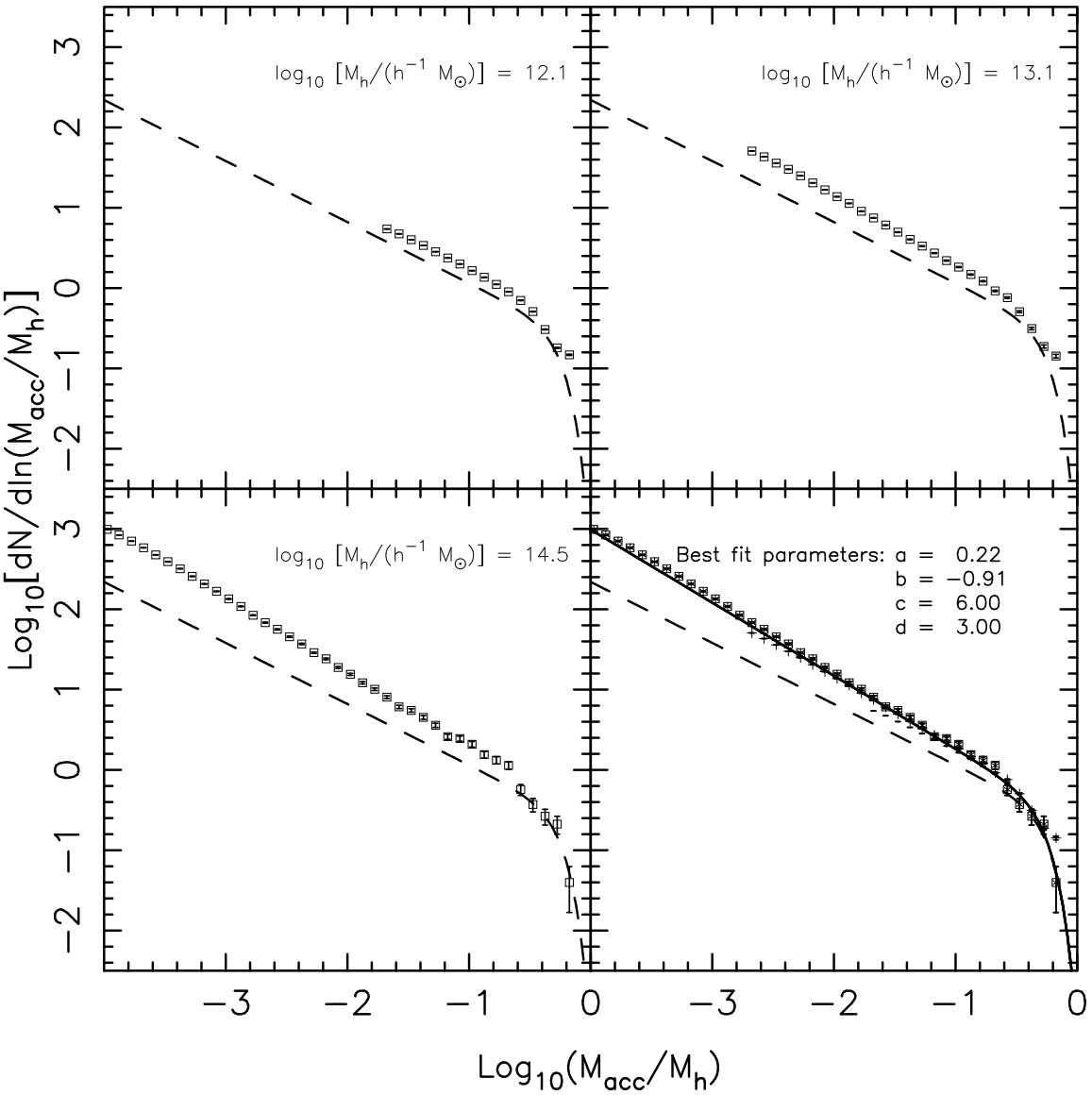

Figure 4.4. The USMF of all sub-halos that merged on the entire halo merging tree, plotted in the same way as in Fig. 4.2. Here, for reference purpose, the dashed lines in each panel represent our "universal" fit of the USMF of the main branch sub-halos (the same as the thick solid line in the lower right panel of Fig. 4.2). Similar to Fig. 4.2, in the *lower right panel* we choose an empirical set of parameters (values as indicated in the panel) for equation (4.1) and plot in thick solid line, so that it simultaneously fits all data points from the previous three panels.

for sub-halos in the main branch. This is not difficult to understand. When we trace back in time to all branches on the merging tree, the number of sub-branches on the halo merging tree increases significantly with redshift due to bifurcation. Meanwhile,

the average mass of progenitors drops dramatically because of mass conservation. Since our mass function is based on the unevolved merger progenitors, more mergers of low-mass sub-halos are expected at higher redshift.

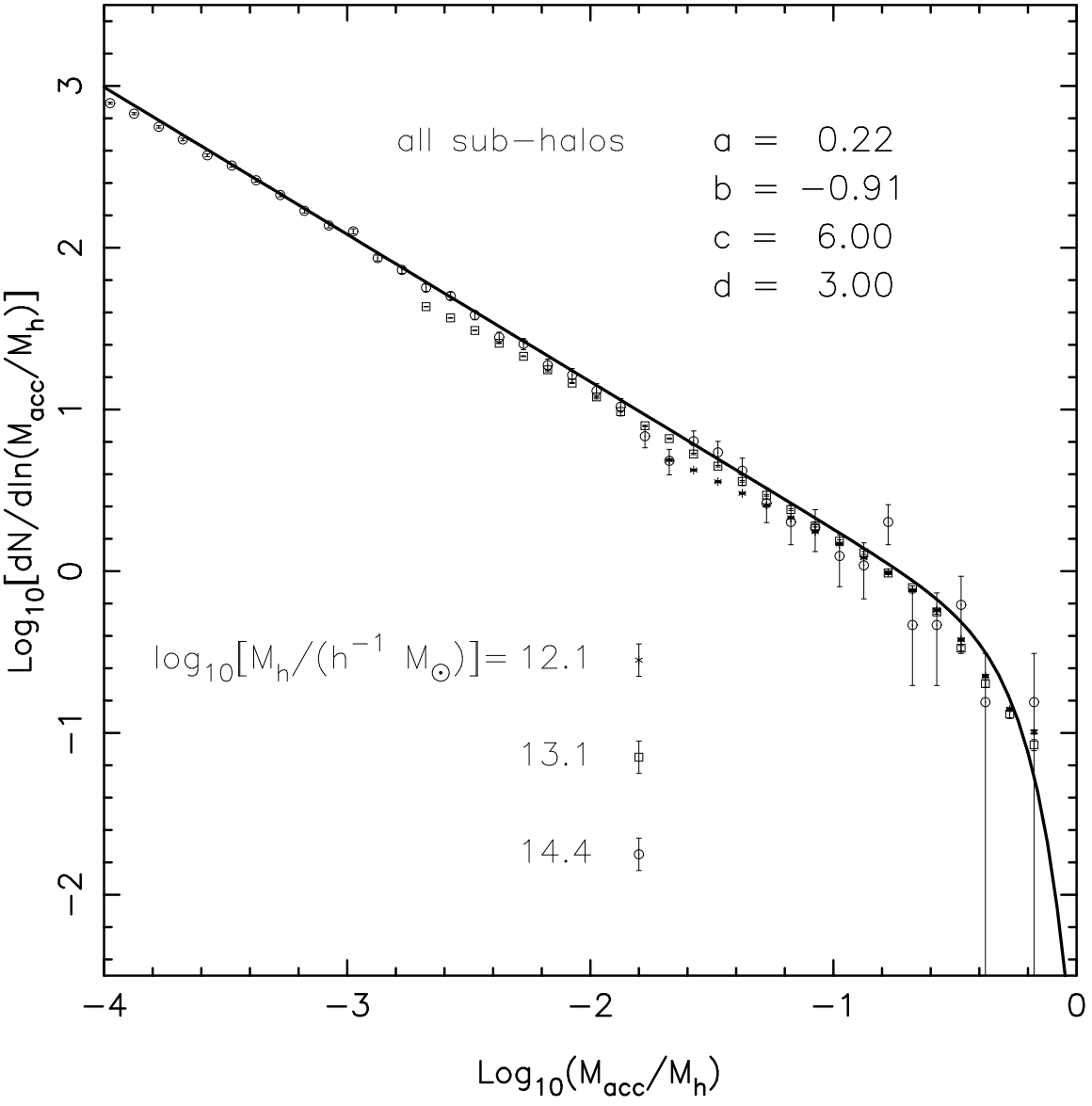

Figure 4.5. The USMF of all sub-halos for host halos at $z_{\rm h} = 1$. Same as in Fig. 4.3, different symbols represent the data points for host halos with different masses (as indicated), and the solid line is the universal fit we have obtained from $z_{\rm h} = 0$ halos.

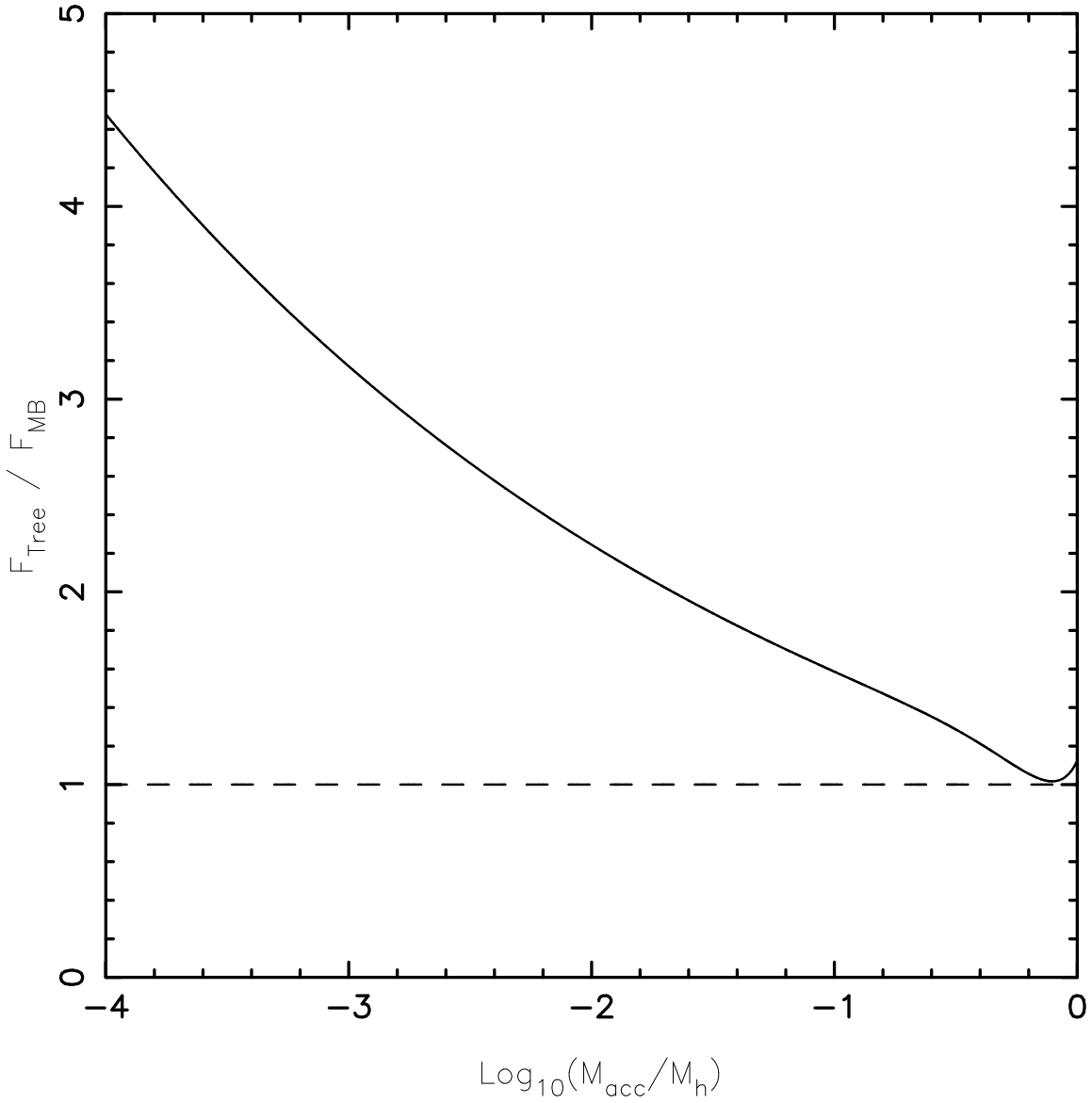

Figure 4.6. Comparison between the USMFs of main-branch sub-halos and all sub-halos. The solid line shows the USMF of all sub-halos divided by the USMF of main branch sub-halos, based on the two fitting results we have obtained. Dashed line is a reference line of $y = 1$.

In Fig. 4.5 we show the USMF of all sub-halos for host halos identified at $z_{\rm h} = 1$. Clearly, this USMF shows remarkable agreement with that for $z_{\rm h} = 0$ host halos, indicating that the USMF of sub-halos in the entire merging tree also has a universal form.

Let $F_{\rm Tree}$ and $F_{\rm MB}$ represent our universal fits to the USMFs of all sub-halos and the main branch sub-halos, respectively. Fig. 4.6 shows the ratio of these two functions as a function of $M_{\rm acc}/M_{\rm h}$. At the low-mass end $F_{\rm Tree}$ is about four times $F_{\rm MB}$, while at the high-mass end they are nearly equal. The significant excessive rate of mergers at low-mass end seen in the ratio indicates the abundance of sub-halos that were accreted by the sub-branches of the merging tree (we will discuss in details later). These sub-halos may end up as the so-called sub-subhalos when they finally settle in the main progenitor (Yang et al., 2009).

As we have seen, the USMF of the main branch sub-halos is universal, independent of the mass and redshift of host halos. This proposition has been adopted by some authors when modeling the population of satellite galaxies in dark matter halos (e.g. Yang et al., 2009). Yang et al. (2009) assumed that the USMF of main branch sub-halos is self-similar, and sub-halos can be divided into different "levels". Since sub-halos can themselves be considered as host halos at the time of accretion, their sub-halos (referred to sub-sub-halos, or sub^1-halos) are also expected to obey the universal USMF. Similarly, all levels of sub-halos (sub^i-halos, $i = 0, 1, 2, 3, \cdots$, where superscript '0' stands for the main branch sub-halos) should have the same form of USMF. The summation of the USMFs at all levels should be equal to the USMF of sub-halos in the whole tree. To test this, we rewrite equation (4.1) as

$$\begin{aligned} n_{\rm un,0}(M_{\rm acc}|M_{\rm h}) &= \frac{{\rm d}N}{{\rm d}M_{\rm acc}} \\ &= \frac{a}{M_{\rm h}}\left(\frac{M_{\rm acc}}{M_{\rm h}}\right)^{b-1}\exp\left[-c\left(\frac{M_{\rm acc}}{M_{\rm h}}\right)^{d}\right]. \end{aligned} \tag{4.2}$$

Since equation (4.2) is universal, it should apply to all sub^i-halos ($i = 0, 1, 2, 3, \cdots$). This allows us to calculate the conditional USMF of sub^i-halos given the host halo mass $M_{\rm h}$,

$$n_{\rm un,i}(M_{\rm acc,}{}_i|M_{\rm h}) =$$

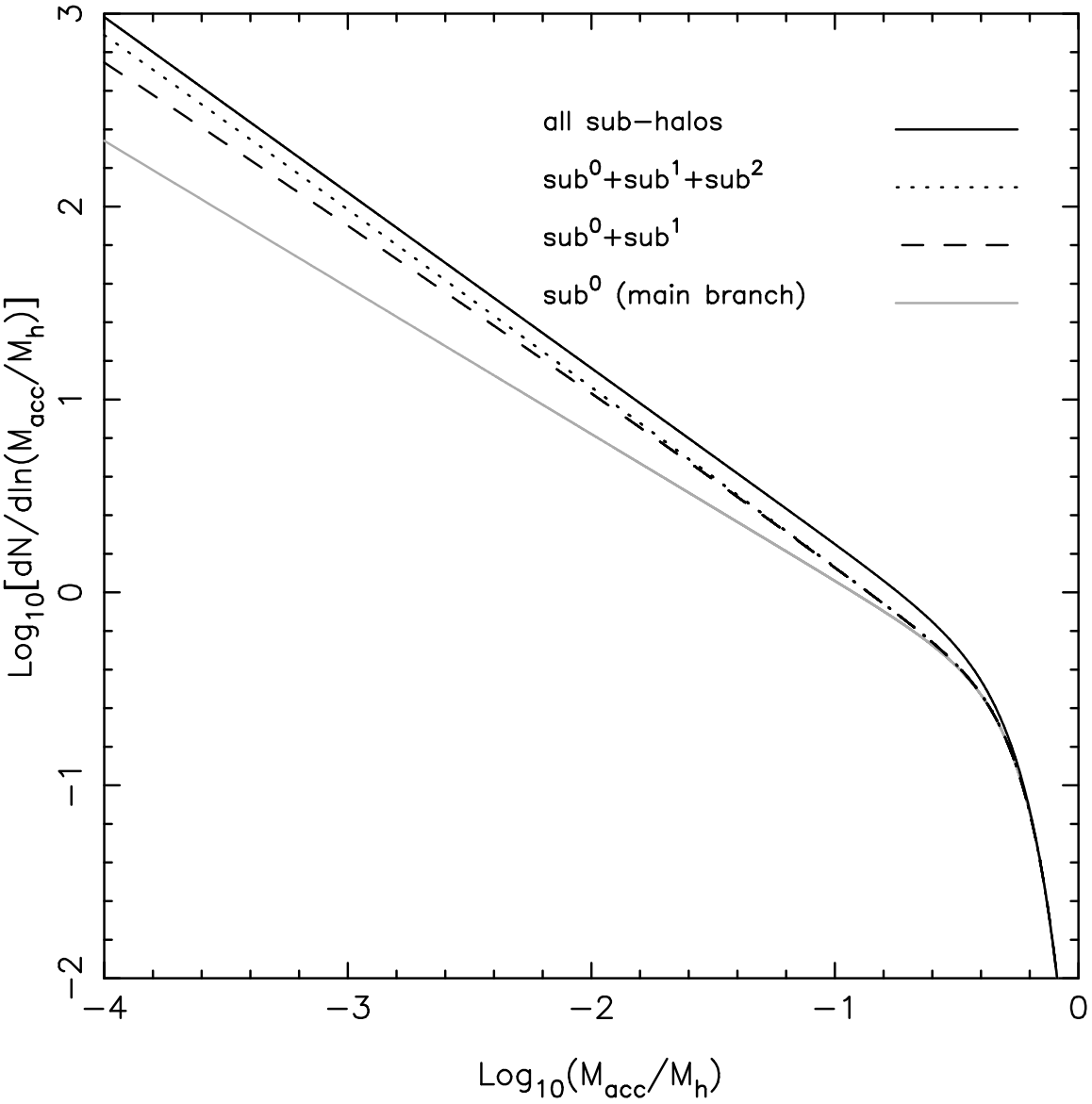

Figure 4.7. Model prediction of sub^i-halos and empirical fittings. Comparison between the USMFs of main branch sub-halos (gray solid line, which is same as the solid line in the lower right panel of Fig. 4.2), all sub-halos (dark solid line, the same as the solid line in the lower right panel of Fig. 4.4), the sum of sub^0 and sub^1-halos (dashed line), as well as the sum of sub^0, sub^1 and sub^2 -halos (short-dashed line) from the model prediction (equation [4.3]).

$$\int_0^{M_{\rm h}} n_{\rm un,0}(M_{{\rm acc},i}|M_{\rm acc}) n_{\rm un,i-1}(M_{\rm acc}|M_{\rm h}) {\rm d}M_{\rm acc}. \tag{4.3}$$

Fig. 4.7 shows the comparison between the USMF of main branch sub-halos, all sub-halos, the sum of sub^0 and sub^1-halos, as well as the sum of sub^0, sub^1 and sub^2

-halos predicted by equation (4.3). The best-fit parameters used in the calculation are indicated in the lower-right panels of Figs. 4.2 and 4.4, respectively. Clearly, as we include more levels of sub-halos, the summation of their USMF approaches asymptotically to that of all sub-halos. It is also interesting that sub^1-halos contribute the largest fraction of small sub-halos that are not included in the USMF of the main branch sub-halos. Note that in the mass range $M_{\rm acc}/M_{\rm h} \in [-2, -0.3]$, the difference between the dark solid line and the short-dashed line in Fig. 4.7 is more significant. It is unclear if this difference is real, or it is due to the limited statistics of the simulation data.

4.3.3 Survived sub-halos

In the two cases discussed above, the USMFs do not seem to depend on the final halo mass or redshift, and appear to be "universal". However, once a sub-halo merges into a host halo, it will undergo a number of non-linear processes such as dynamical friction, which causes the sub-halo to merge into the center of the host, and tidal stripping, which causes it to lose mass or to be completely destroyed. Therefore, the number of *survived* sub-halos may be significantly lower than the sub-halo abundance described by the USMF. Note that there are two kinds of survived sub-halos: those that directly merged into the main branch, and those that were already a sub-halo of a larger progenitor when being accreted by the main progenitor. Throughout this Chapter, we refer to the former as sub^A-halos, and the latter as sub^B-halos, which are also known as sub-subhalos.

After removing the sub^B-halos from our survived sub-halo catalogue, we construct the "unevolved" mass function of the sub^A-halos. The quotation marks are used to indicate that a certain fraction of the main branch sub-halos have been completely destroyed, although the sub-halo mass used here is the mass at the time of accretion, $M_{\rm acc}$. Since the destroyed sub-halos are not included, we use $F'_{\rm sub^A}$ to distinguish this

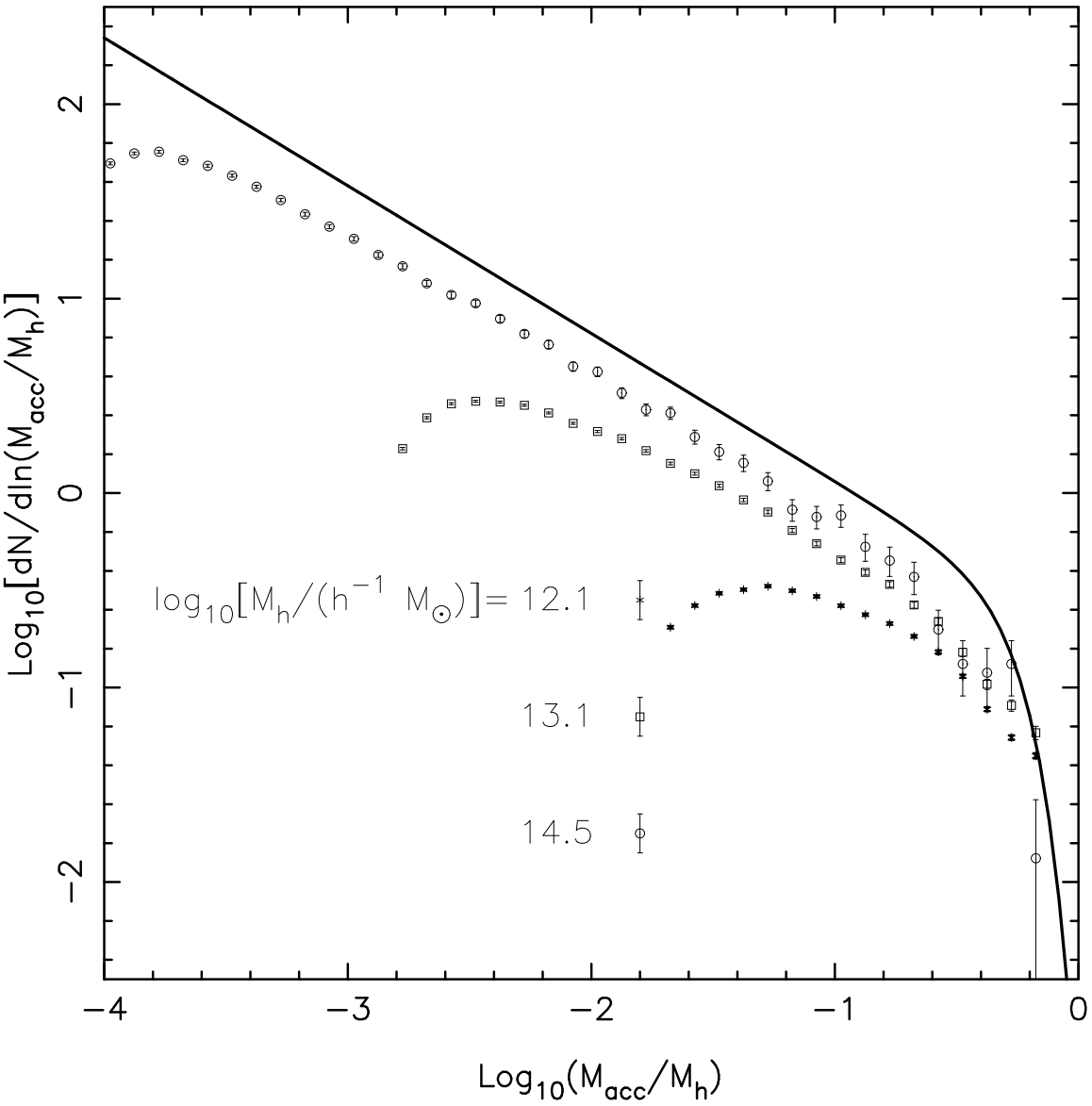

Figure 4.8. The "unevolved" mass function of sub^A-halos, $F'_{\rm sub^A}$. Different symbols represent different final host halo mass. The thick solid line is the universal form of the USMF of main branch sub-halos.

"unevolved" sub-halo mass function from the USMF discussed previously. Fig. 4.8 shows the "unevolved" sub-halo mass function so defined for host halos with $M_{\rm h} = 10^{12.1}$, $10^{13.1}$, and $10^{14.5}\,h^{-1}{\rm M}_\odot$, respectively. Apparently the shape of $F'_{\rm sub^A}$ depends strongly on host halo mass. Unlike the USMFs discussed previously, for given host halo mass $M_{\rm h}$, $F'_{\rm sub^A}$ is not a monotonic decreasing function of sub-halo mass, but rather, its amplitude lowers when the sub-halo mass becomes very small. This is

caused by the dynamical processes after the accretion of sub-halo. Note, however, that the value of $M_{\rm acc}/M_{\rm h}$ at which $F'_{\rm sub^A}$ peaks depends on the mass limit $M_{\rm lim}$ adopted. There is a high probability that a sub-halo initially accreted with mass $M_{\rm acc}$ slightly above $M_{\rm lim}$ to become smaller than $M_{\rm lim}$ during the post-accretion phase and thus to be marked as "destroyed". In addition, smaller sub-halos are more difficult to survive, because on average they were accreted into their hosts earlier.

Fig. 4.8 may be used to estimate the number fraction of sub-halos that survive the mass-loss process. For example, for halos with $M_{\rm h} \sim 10^{14.5}\,h^{-1}{\rm M}_{\odot}$, about 62% of the accreted main branch sub-halos above the mass limit $M_{\rm lim}$ have been completely destroyed, this fraction increases to $\sim$ 78% and $\sim$ 84% for $M_{\rm h} = 10^{13}\,h^{-1}{\rm M}_{\odot}$ and $M_{\rm h} = 10^{12}\,h^{-1}{\rm M}_{\odot}$ halos, respectively. This trend may be understood since small systems start to accrete progenitors earlier, and so their main branch sub-halos are subject to mass loss and destruction for a longer time. The shape of $F'_{\rm sub^A}$ for host halos at $z_{\rm h} = 1$ is similar to that at $z_{\rm h} = 0$. However, the similarity here is less meaningful, because the shape of F' is highly affected by the non-linear effects during sub-halo mergers, which is a very stochastic process (Angulo et al., 2008b).

The result presented here is consistent with that of Giocoli et al. (2008a, their Fig. 4), although their result is based on the *evolved* sub-halo mass function. They found that for small host halos, there are less sub-halos with the same fractional mass, $M_{\rm sub}/M_{\rm h}$ (where $M_{\rm sub}$ is the *current* mass of survived sub-halos), than more massive host halos. In Fig. 4.8, we have showed that for smaller host halo mass, the amplitude of the "unevolved" sub^A-halo mass function, $F'_{\rm sub^A}$, is also lower. In addition, according to Giocoli et al. (2008a, and reference therein), for evolved sub-halos mass function, the low-mass end is always higher than the high-mass end. Combining their results and our results of $F'_{\rm sub^A}$, we see that the majority of the smallest survived sub-halos are not the descendants of the smallest sub-halos initially accreted, but rather, the descendants of those that are several times more massive.

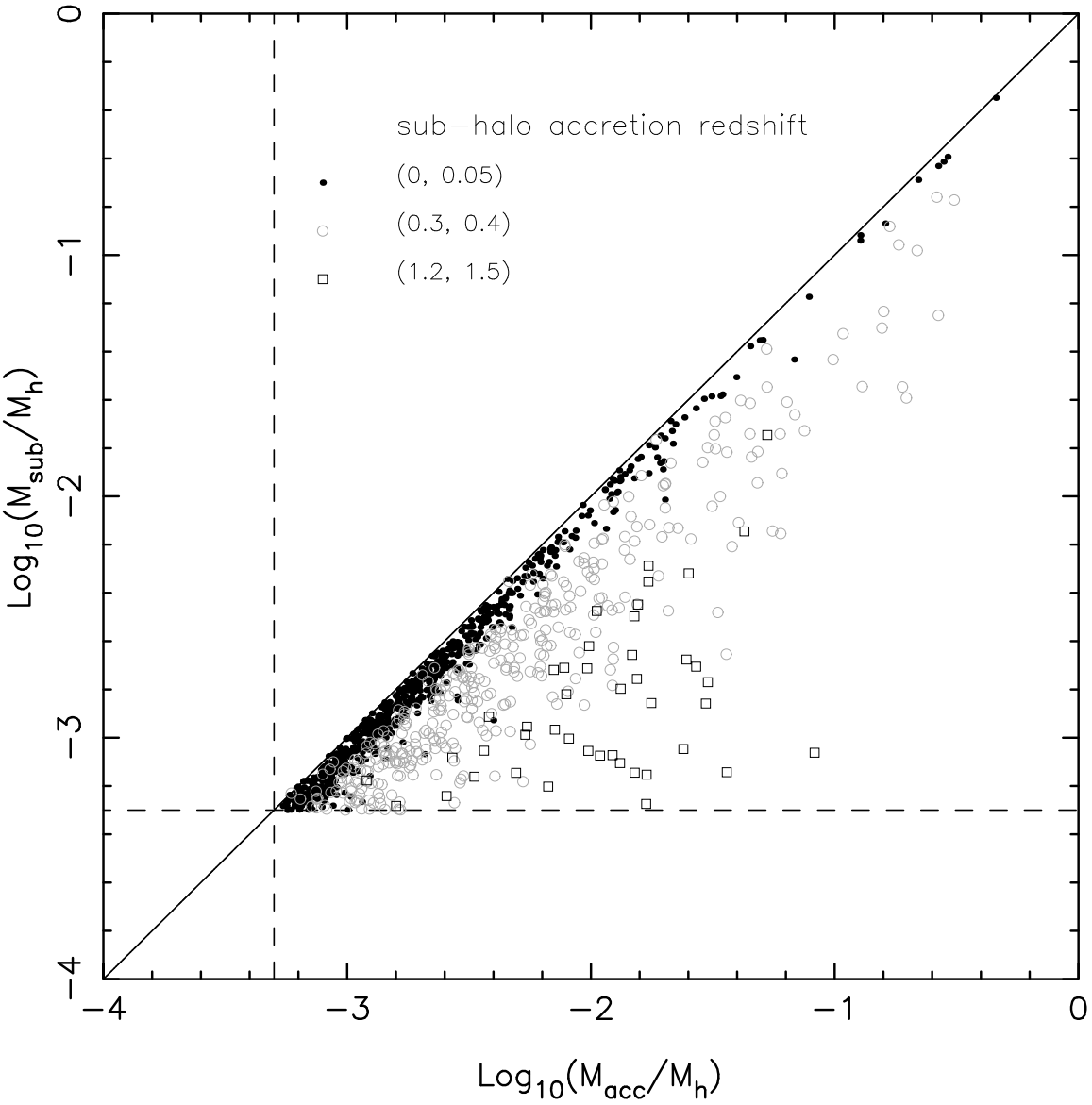

Figure 4.9. $M_{\rm acc}$ against $M_{\rm sub}$, given final host halo mass $M_{\rm h}$. Points are from 200 randomly selected host halos with $M_{\rm h} \approx 10^{13.6}\,h^{-1}{\rm M}_{\odot}$. Different symbols denote different redshift intervals during which the sub-halos enter the main progenitor of the host halo. Dashed lines indicate the mass limitation in our analysis, $M_{\rm lim}$.

Fig. 4.9 plots $M_{\rm acc}$, the mass at accretion, against current mass, $M_{\rm sub}$ of sub-halos, in 200 host halos with $M_{\rm h} \approx 10^{13.6}\,h^{-1}{\rm M}_{\odot}$. Three different symbols denote different sub-halo accretion redshifts. It is clear that given $M_{\rm sub}$, sub-halos accreted earlier generally have higher $M_{\rm acc}$. At low redshift ($z \in [0, 0.05]$), sub-halos with a wide range of mass ($\log_{10}[M_{\rm acc}/M_{\rm h}] \in [-3.3, -0.5]$) were accreted by the main progenitor, and

they barely suffered from the mass loss (with the resultant $M_{\rm sub} \approx M_{\rm acc}$). However, for sub-halos that were accreted at high redshift ($z \in [1.2, 1.5]$), their $M_{\rm acc}$ needs to several times higher than the mass limitation in our analysis, $M_{\rm lim}$, in order to survive at the present time, with $M_{\rm sub}$ close to $M_{\rm lim}$. Note that these results actually depend on the resolution limit of simulation. If the resolution limit of a simulation is infinite, then one would expect that all accreted sub-halos should survive at the present time, and $F'_{\rm sub^A}$ should be the same as the USMF of main branch sub-halos. However, our results reveal how the survived halos were accreted during the assembly history of dark matter halos above our resolution limit, as we will discuss in more details later.

Besides $F'_{\rm sub^A}$, we also construct the "unevolved" mass function for the sub^B-halo population, $F'_{\rm sub^B}$, in the same way as $F'_{\rm sub^A}$. Fig. 4.10 shows the ratio of $F'_{\rm sub^B}$ to $F'_{\rm sub^A}$, for host halos with the same masses as in Fig. 4.8. We would like to remind the reader, once again, that the sub-halo mass used here is measured at the time when they were last found as isolated halos. Given a sub-halo mass, the vertical axis in Fig. 4.10 is the ratio of the number of survived sub-halos initially accreted by sub-branches to the number of survived sub-halos initially accreted by the main branch. In general, $F'_{\rm sub^B}/F'_{\rm sub^A}$ is higher for massive host halos. For a given host halo mass, though, this ratio is always low (~ 0.05) at the high-mass end ($\log_{10}[M_{\rm acc}/M_{\rm h}] > -0.7$), because mergers involving sub-halos with mass comparable to that of the final host halo can only happen on the main progenitor at very late time. There also appears to be a generally increasing trend in this ratio as sub-halo mass decreases down to a certain point. This may be due to two reasons. First, some small sub-halos that merge to sub-branches of the merging tree may survive if the time scale for disruption is long. Second, as the redshift increases, the number of mergers that happen on sub-branches is not negligible. The increasing trend changes its sign when sub-halo mass becomes very small. The reason is that small sub-halos that are able to survive were most

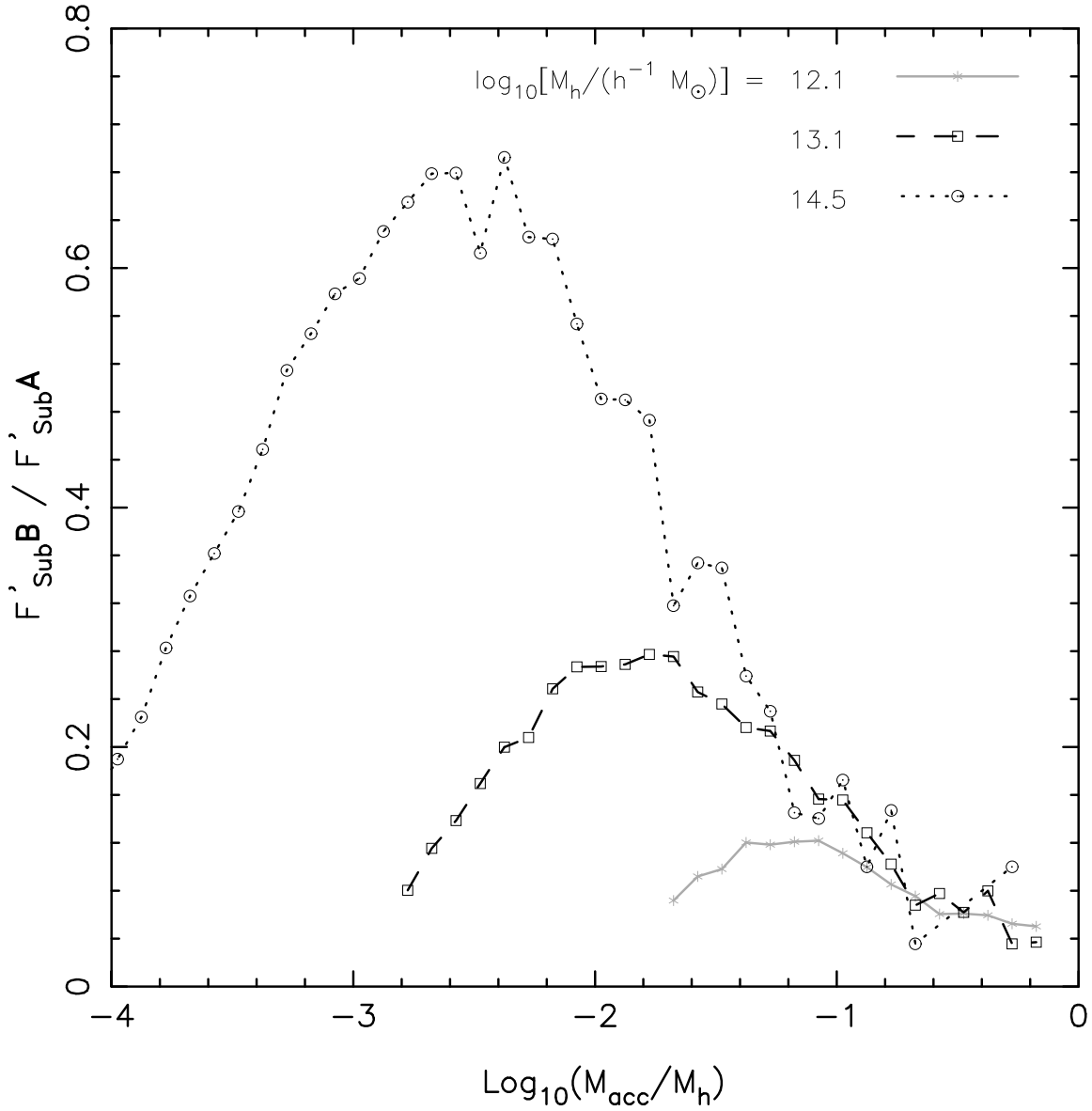

Figure 4.10. The ratio of $F'_{\rm sub^B}$ to $F'_{\rm sub^A}$ (see text for details). Different symbols indicate different host halo mass.

likely accreted in the recent past, when main branch already dominates the merger incidences.

We can estimate the number fraction of sub^B-halos among the whole survived sub-halo population, based on Fig. 4.10. This fraction is 9%, 17% and 28%, for host halo with $M_{\rm h} = 10^{12.1}$, $10^{13.1}$, and $10^{14.5}\,h^{-1}{\rm M}_\odot$, respectively. Clearly, a significant fraction of sub-structures were sub-subhalos.

4.4 Accretion time of sub-halos

Although the USMFs give a quantitative description on the abundance of accreted sub-halos in the halo assembly history, it does not include the time (redshift) when the accretion happens. In galaxy formation models, the epoch when central galaxies became satellites is crucial as the physical processes relevant to galaxy evolution after the merger are expected to be different. It is therefore important to incorporate the sub-halo abundance at different redshift into our analysis.

4.4.1 Sub-halo mass function at given accretion time

4.4.1.1 Main branch sub-halos and all sub-halos

We define the mass function of sub-halos at given accretion time (redshift) as follows,

$$f(z) = \frac{\mathrm{d}F}{\mathrm{d}z} = \frac{\mathrm{d}N(z)}{\mathrm{d}\ln(M_{\rm acc}/M_{\rm h})\mathrm{d}z}, \tag{4.4}$$

where F is the USMF, $M_{\rm acc}$ and $M_{\rm h}$ stand for the mass of sub-halos at the time of accretion and the mass of final host halo, respectively. To obtain $f(z)$, we choose a redshift interval Δz around a given z, and only count the number, $N(z)$, of sub-halos accreted during Δz. Within the redshift range of interest, we found $\Delta z \sim 0.1$ effectively eliminates the noise and result in a relatively smooth shape of f.

Fig. 4.11 and 4.12 shows f of main branch sub-halos and all sub-halos for host halos with $M_{\rm h} = 10^{13.6}\,h^{-1}\mathrm{M}_{\odot}$. Interestingly, in each case, f can still be described by equation (4.1) reasonably well. In addition, we found that the low-mass end power-index b of f are virtually independent of z, and is quite similar to the power-index we have obtained from the corresponding USMF. Since $F = \int f\mathrm{d}z$, it is expected that the integration of f over z reproduces the low-mass end power-index of F. The exponential shape of f (described by d) at the high mass end also shows no obvious dependence on z. On the other hand, the amplitude of f and the transitional point where f deviates from the power-law clearly depend on the redshift. By keeping b

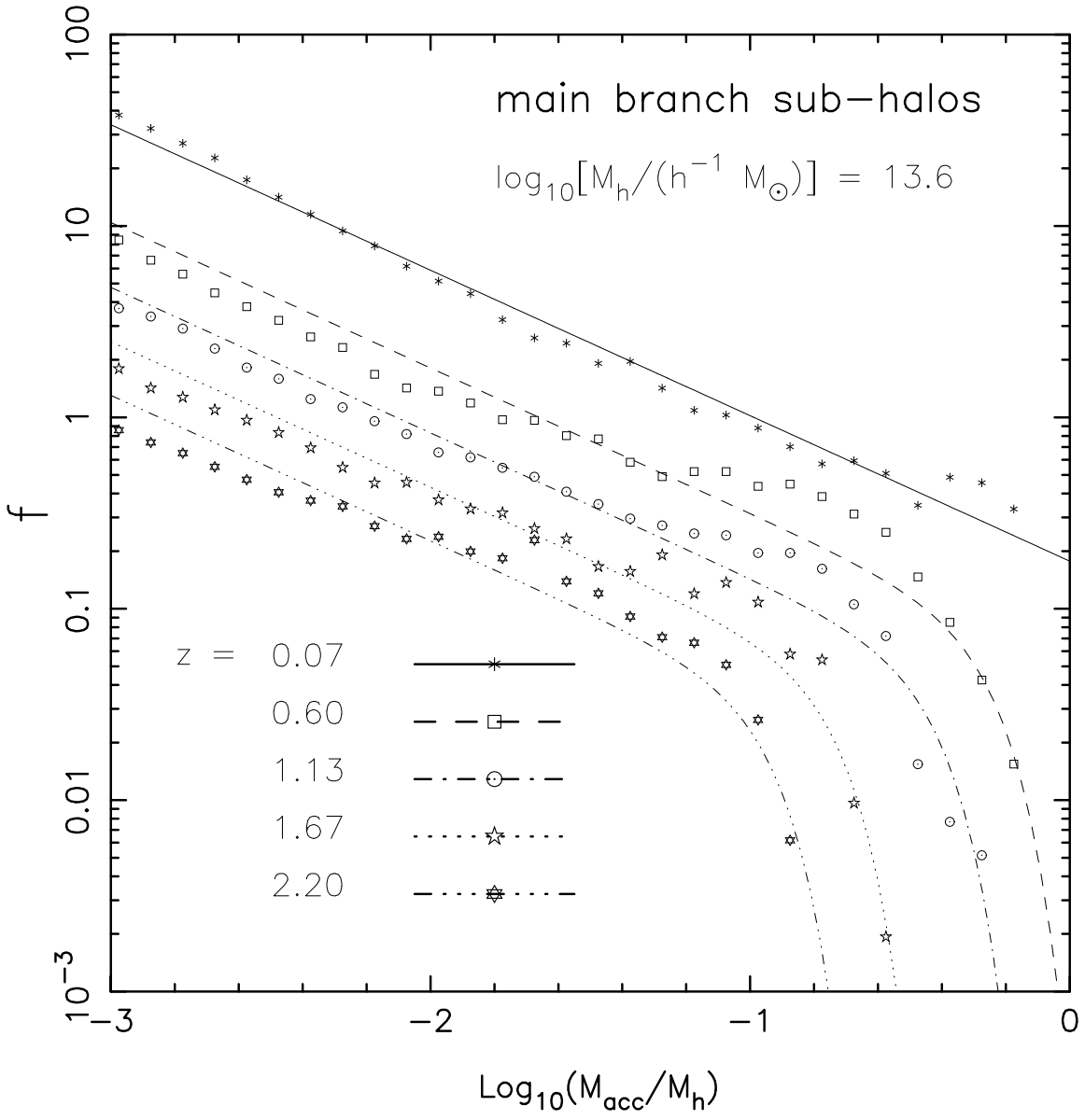

Figure 4.11. The mass function at accretion, f, of main branch sub-halos, given accretion redshift z and host halo mass $10^{13.6}\ h^{-1}\mathrm{M}_{\odot}$. Different symbols and lines represent the data points and their best fits according to equation (4.1) (with fixed b and d, see text for details), at different redshifts.

and d fixed at the values obtained from the USMFs ($b = -0.76$, $d = 3.2$ for main branch sub-halos, and $b = -0.91$, $d = 3.0$ for all sub-halos), we fit f according to

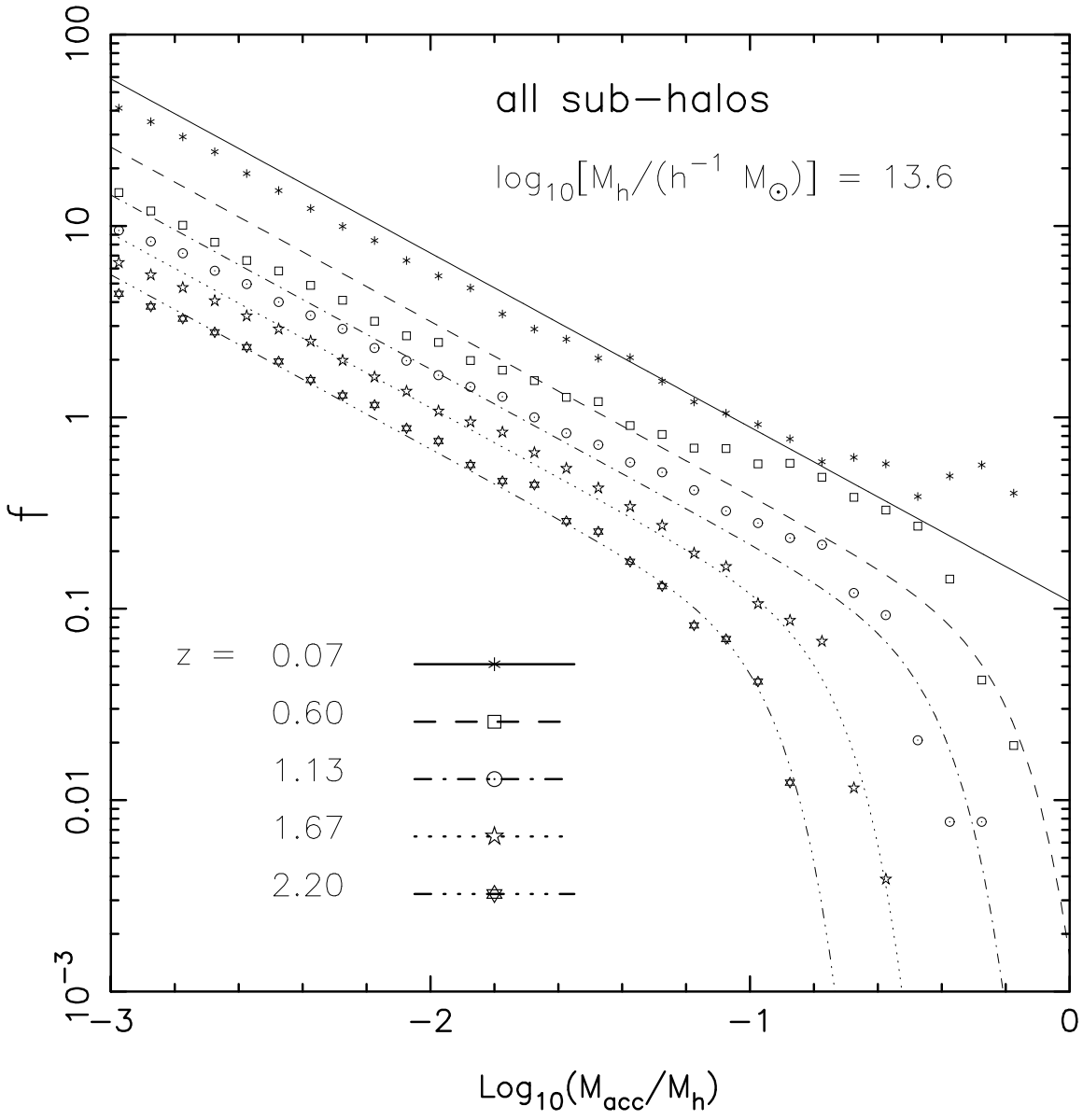

Figure 4.12. The mass function at accretion, f, of all sub-halos, given accretion redshift z and host halo mass $10^{13.6}\,h^{-1}\mathrm{M}_{\odot}$. Different symbols and lines represent the data points and their best fits according to equation (4.1) (with fixed b and d, see text for details), at different redshifts.

equation (4.1). Styled lines in Fig. 4.11 and 4.12 are the best-fits of f so obtained at the corresponding redshift.

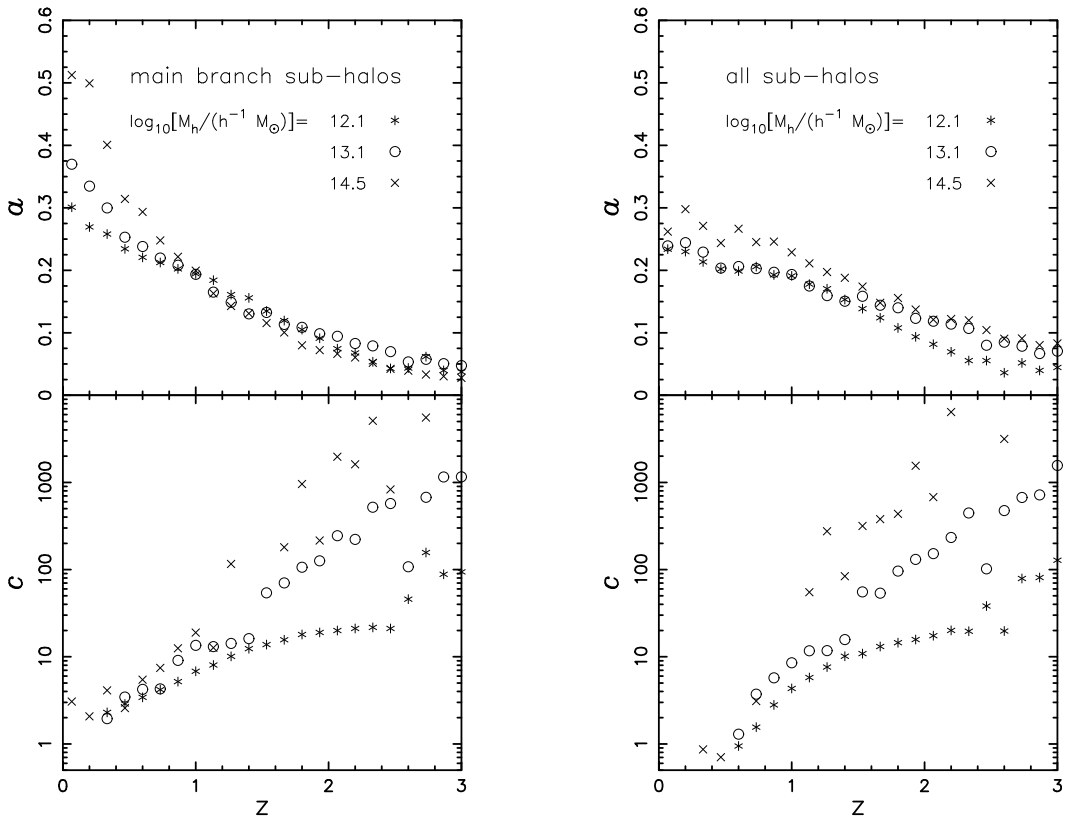

Figure 4.13. Best fit parameters a and c, given fixed b and d, of f, against redshift z. *Panels on the left* shows the result for main branch sub-halos, *panels on the right* shows the result for all sub-halos. Different symbols represent different host halo masses, as indicated in the figure.

In Fig. 4.13, we show the best-fit a and c against the redshift z, for host halo with different masses. Panels on the left are best-fit a and c for main branch sub-halos, while panels on the right are best-fit a and c for all sub-halos. In general, a always decreases monotonically as z increases, which implies that more sub-halos are accreted at lower redshift, especially for massive halos. Meanwhile, c shows positive correlation with z, which means that, compared with small sub-halos, the number of massive sub-halos drops more quickly as redshift increases. This disagrees with the result of Giocoli et al. (2008a). Their Fig. 1 shows that the USMF of the main branch sub-halos accreted before the halo formation time $z_{\rm f}$ is identical to the USMF of the

sub-halos accreted after $z_{\rm f}$, with proper adjustment in the amplitude a only. However, as we just mentioned, the number of massive sub-halos drops more quickly at higher redshift, and therefore simply offsetting the USMF of high-redshift sub-halos along the vertical direction cannot reconcile the lack of massive sub-halos and reproduce the shape at high-mass end of the USMF. Our results suggest that the relative abundance of massive sub-halos becomes higher at low redshift, consistent with the hierarchical formation of dark halos in a CDM model.

4.4.1.2 Survived sub-halos accreted by the main progenitor

Given the time of merging, let us look at the mass function of sub-halos that survive as sub-structures in the final halo. We focus on sub^A-halos, as the results for sub^B-halos are similar. Based on the sub^A-halo catalogue, we can register the time when they first became satellites of the main progenitor. We use $f'_{\rm sub^A}(z)$ to indicate the same sub^A-halo mass function at given accretion time defined in equation (4.4).

Fig. 4.14 shows $f'_{\rm sub^A}$ at different redshifts, for host halo mass $M_{\rm h} = 10^{13.6}\,h^{-1}{\rm M}_\odot$. Note that the redshifts we used to plot $f'_{\rm sub^A}(z)$ is, on average, lower than the redshifts used in Fig. 4.11 and 4.12, because at higher redshift such as $z > 1$, $f'_{\rm sub^A}$ becomes extremely small. Comparing Fig. 4.14 with Fig. 4.11, one can find both similarity and difference. At very low redshift ($z = 0.07$), $f'_{\rm sub^A}$ and f are similar, due to the fact that sub-halos accreted by the main progenitor recently have a high survival rate. However, at higher redshift ($z = 0.6$), $f'_{\rm sub^A}$ becomes much lower than f, owing to the dynamical effects that can effectively destroy the sub-halos accreted at early time.

As we have shown in Fig. 4.8, the "unevolved" mass function of sub^A-halos, $F'_{\rm sub^A}$, is not universal. Besides, the overall amplitude of $F'_{\rm sub^A}$, also deviates substantially from the original USMF of main branch sub-halos, $F_{\rm mb}$, especially at the low-mass end. The reason is clearly demonstrated in Fig. 4.14. When redshift increases, $f'_{\rm sub^A}$ becomes increasingly lower, especially for small sub-halos. Since F' is the integration

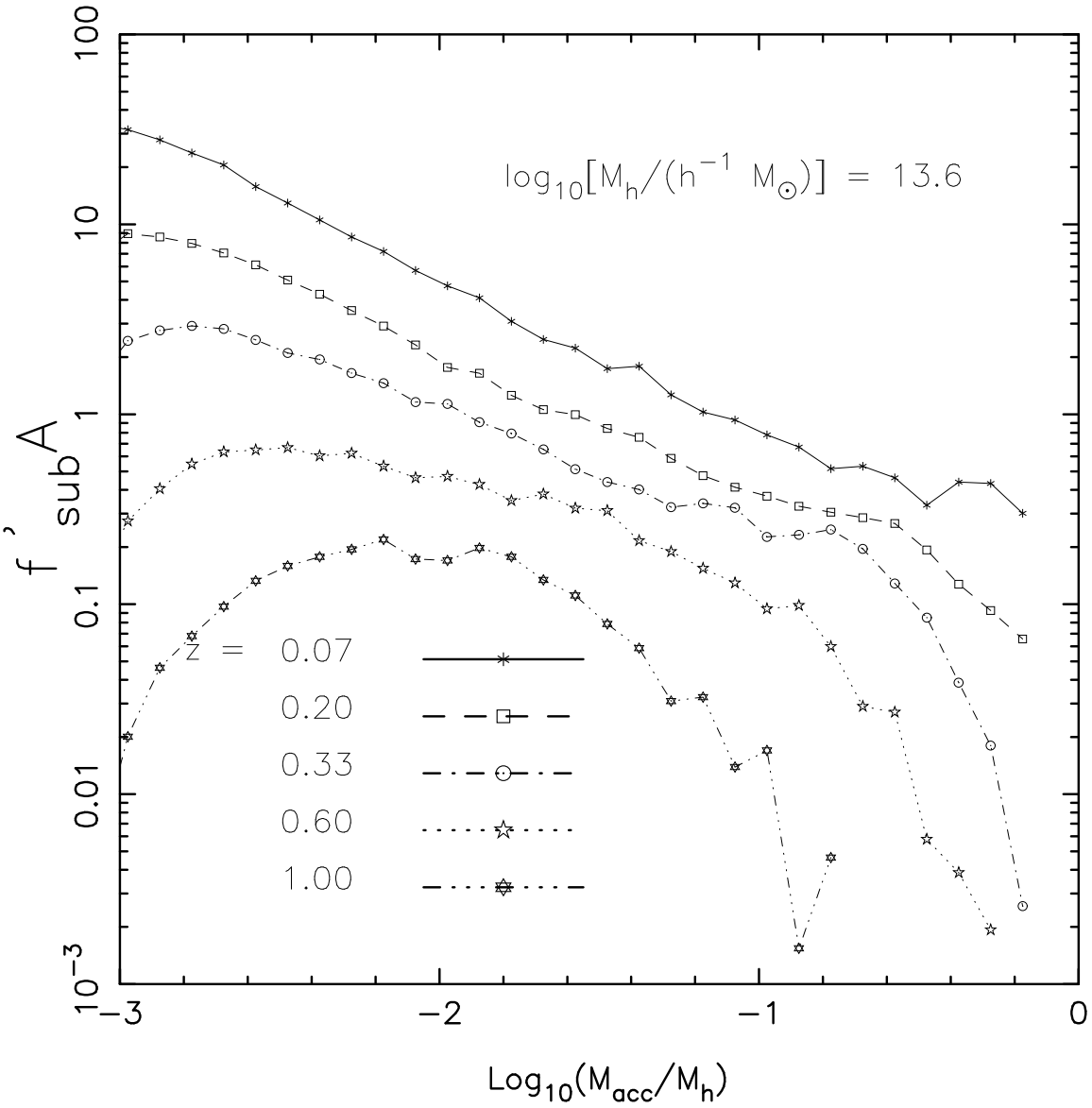

Figure 4.14. The sub^A-halo mass function at accretion, $f'_{\rm sub^A}$, given accretion redshift z and host halo with $M_{\rm h} = 10^{13.6}\,h^{-1}{\rm M}_\odot$. Different symbols connected with styled lines represent results at different redshifts.

of f' over z, it is therefore expected that $F'_{\rm sub^A}$ would have the behavior shown in Fig. 4.8.

4.4.2 Distribution of sub-halo accretion time

In the previous sub-section, we have discussed the sub-halo mass function at accretion for given redshift. It clearly shows that the abundance of sub-halo accretion

varies with redshift. In general, more sub-halos were accreted at lower redshift. It also seems that sub-halos with different masses may be accreted at different time.

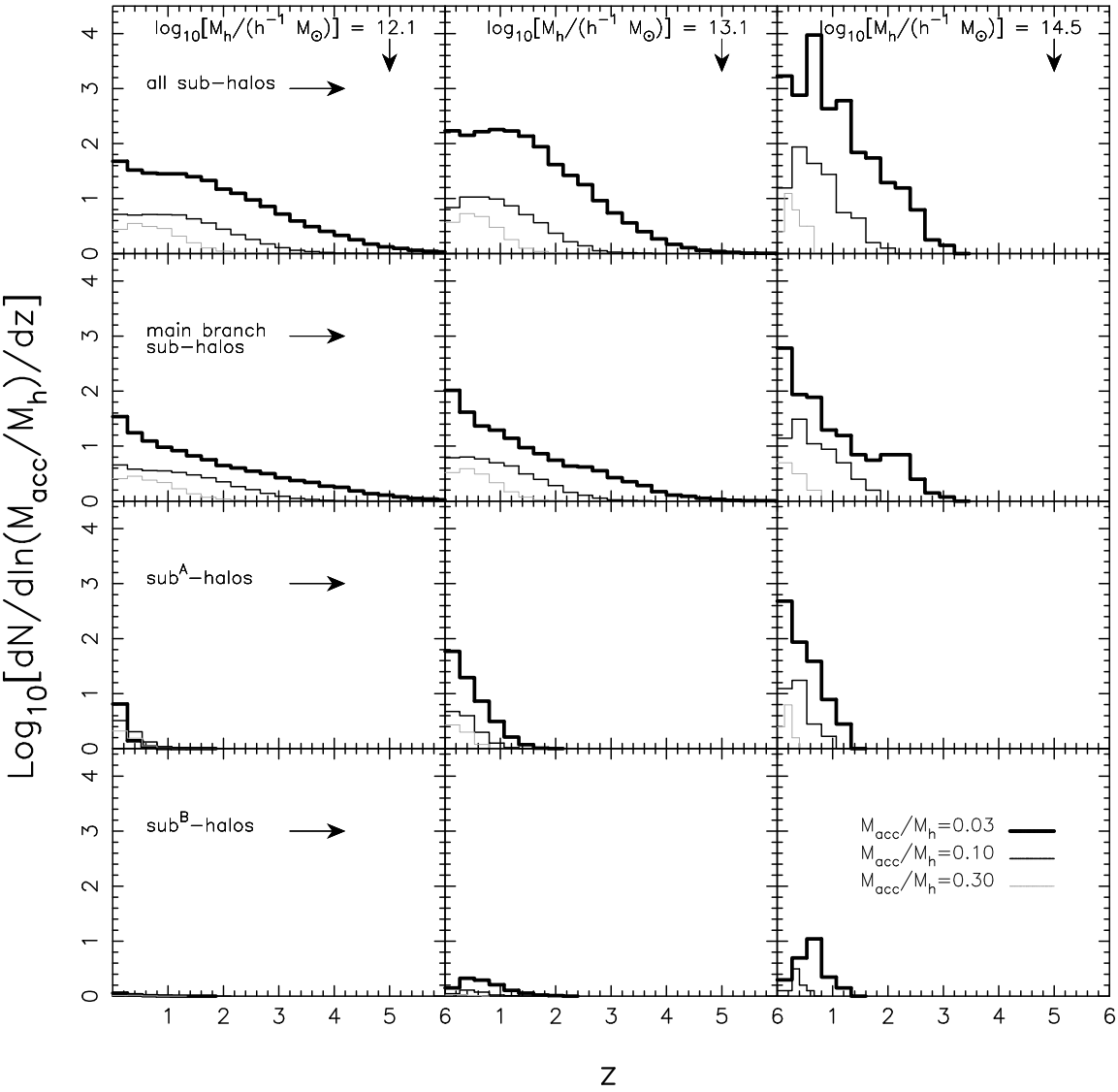

Figure 4.15. Sub-halo mass function at the time of accretion against redshift z, given sub-halos mass $M_{\rm acc}$ and final host halo mass $M_{\rm h}$. Each row represents one definition of sub-halo, and different columns represent different host halo masses, as indicated by the arrows. There are three lines in every panel. Think solid line is for sub-halo with $M_{\rm acc} = 0.03M_{\rm h}$, light solid line is for sub-halo with $M_{\rm acc} = 0.1M_{\rm h}$ and gray solid line is for sub-halo with $M_{\rm acc} = 0.3M_{\rm h}$.

Given sub-halo mass fraction $M_{\rm acc}/M_{\rm h}$ and host halo mass $M_{\rm h}$, Fig. 4.15 shows the number of sub-halo at the time of accretion as a function of redshift. Clearly, for fixed $M_{\rm acc}/M_{\rm h}$, small systems start to accrete sub-halo earlier. For instance, dark

halos with $10^{12.1}\,h^{-1}\mathrm{M}_{\odot}$ begin to acquire sub-halos with $M_{\rm acc} = 0.03M_{\rm h}$ at $z = 5 \sim 6$, while for halos with $10^{14.5}\,h^{-1}\mathrm{M}_{\odot}$, this happens at $z \sim 3$. Compared with small sub-halos, large sub-halos enter the system fairly late. Nearly all sub-halos with mass $M_{\rm acc} = 0.3M_{\rm h}$ enter their host at redshift $z < 1.5$.

For fixed host halo mass, large fraction of small sub-halos enter the system through sub-branches, especially at high redshift such as $z > 1$, while massive sub-halos (i.e., $M_{\rm acc}/M_{\rm h} = 0.3$) enter the systems only through the main branch, at relatively lower redshift. In addition, as discussed in Section 4.3, almost all survived sub-halos (sub^{A,B}-halos) were accreted at redshift $z < 1$, and more sub^{A,B}-halos are likely to survive in massive systems.

On average, sub-halo accretion of dark halos is determined by the initial CDM density power-spectrum and shows hierarchical signature. The sub-halo accretion for individual dark halos, however, can be very stochastic. Let $P_{1/2,M_{\rm acc}/M_{\rm h}}(z)$ denotes the probability distribution function (PDF) of the redshift z by which the host halo has acquired 1/2 of the total number of the *main branch* sub-halos with fixed mass $M_{\rm acc}/M_{\rm h}$. Fig. 4.16 shows $P_{1/2,M_{\rm acc}/M_{\rm h}}$ as a function of z, for sub-halos with mass $M_{\rm acc} = (2-5)\%M_{\rm h}$. We choose $M_{\rm acc} \sim 3\%$ of $M_{\rm h}$ to ensure that the majority ($> 75\%$) of our catalogued halos would have more than one sub-halo mergers with such sub-halo mass. Clearly, the redshift covers a wide range: $z \in (0,6),(0,5),(0,3)$ for halos with $M_{\rm h} = 10^{12.1}$, $10^{13.1}$, and $10^{14.5}\,h^{-1}\mathrm{M}_{\odot}$, respectively. This indicates that, even for the same sub-halo mass and host halo mass, sub-halo merger is a highly stochastic process.

4.5 Conclusions

Halo-halo merger is the basis of galaxy merger. The time of merger and the sub-halo mass at the time of merger are two important halo properties relevant for modeling galaxy formation. In this paper, we study the mass function and other

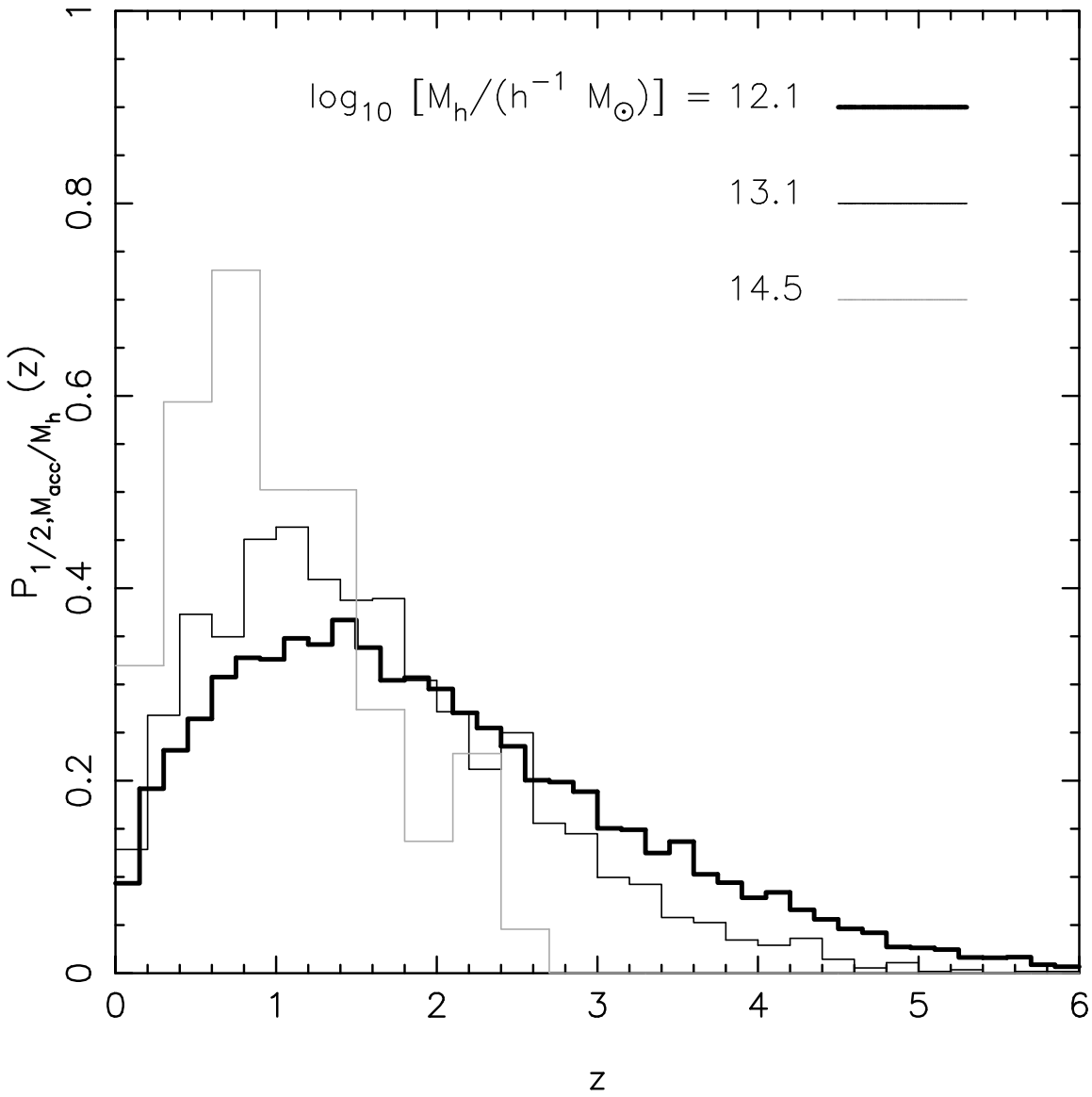

Figure 4.16. $P_{1/2,M_{\rm acc}/M_{\rm h}}(z)$, given main branch sub-halo mass $M_{\rm acc} = (2-5)\%M_{\rm h}$. Different lines represent different host halo masses.

properties of sub-halo mergers during the dark halo assembly history. We studied three kinds of sub-halos: main branch sub-halos, all sub-halos, and sub-halos that survived the dynamical disruption after merger. We also studied the redshift dependence and evolution of sub-halo mass function, as well as the distribution of the redshift at which a sub-halo is accreted. Our main findings can be summarized as follows:

1. We confirmed the previous result that the average unevolved mass function of main branch sub-halos follows a universal functional form, regardless of host halo mass (Giocoli et al., 2008a). In addition, we found that this function is also independent of the redshift of the host halo.

2. The unevolved mass function of all sub-halos that have been accreted during the entire halo assembly history is also a universal function that shows no host-halo-mass or redshift dependence.

3. There are roughly the same or double number of sub-halos, with mass 1% or 0.1% of the final host halo mass, that were accreted by progenitors other than the main progenitor. The amount is significant considering the central galaxies that merge along with such sub-halos may be more resistant to dynamical disruption that destroy the sub-halos.

4. The mass function of survived sub-halos at the time of merging is not universal, due to the fact that large fraction of sub-halos that merged at early time are destroyed by dynamical friction and tidal stripping. The fraction of sub-subhalos can account for up to 30% of the whole survived sub-halo catalogue in cluster-sized dark halos, and decreases with host halo mass.

5. In general, more sub-halos are accreted at lower redshift. However, for given host halo and sub-halo mass, the accretion time has very broad distribution. Survived sub-halos are accreted late and therefore represent a very special subset of the total sub-halo population accreted into host halos.

CHAPTER 5

SUMMARY AND CONCLUSIONS

In this dissertation, I study the mass accretion history, clustering property as well as the sub-halo mass distribution of dark matter halos. The study of the dark halo assembly history not only reveals the connections between assembly history itself and various halo properties, but also, is crucial to understand the galaxy formation, since dark halos are the hosts of galaxies. In this Chapter, I summarize our findings and discuss the implications.

Dark halos form in a hierarchical manner, in the sense that massive halos form later than small halos. The growth history of a dark matter halo can be generally characterized by two phases: an early fast phase and a later slow phase. The fast phase is dominated by major mergers, while the slow phase features gentle mass inflow. These two phases are separated by the time when the virial velocity of a halo reaches its maximum. On average, each dark halo experiences 3-5 major mergers after its main progenitor acquired 1% of final mass, regardless of halo mass. The time when these major mergers happen, however, strongly depends on the halo mass. It appears that the mass acquired during the fast accretion phase effectively reconfigures the gravitational potential well and causes the collisionless dark matter particles to undergo dynamical relaxation and isotropization, therefore the system grows a definite structure for its inner core. On the other hand, the mass acquired during the slow accretion phase is mainly accreted on to the outskirt of the halo, little affecting the inner structure but quiescently rescaling the mass of the system upwards. The

concentration parameter predicted based on this assumption shows a good agreement with numerical simulations.

The two mass accretion phases we have found in our research may significantly affect the main physical processes regulating the evolution of the baryonic matter within dark halos, therefore may be in close connection with the broad observational conclusion that galaxies of late type, which are less massive on average, form their stars at later time - a phenomenon knows as "archaeological downsizing". As suggested by Cook et al. (2009), the violent early phase may be associated with the formation of a spheroid amid with a black hole, which causes strong QSO feedback in massive systems and ends star formation on a short time-scale, while the gentle late phase is more favorable for the stable growth of a disky structure around the pre-existing spheroid.

It also appears to be a correlation between the dark halo assembly history and halo clustering property. Given the mass of dark halos, we confirmed the earlier results that for halos smaller than M_*, their clustering strength is positively correlated with the time when dark halo assemble half of its final mass. Some authors (Jing, Suto & Mo, 2007) also suggest that for halos more massive than M_*, this trend is reversed. The formation-time dependence of halo clustering is different for different definitions of halo formation time. The strongest dependence is seen if we define the halo formation time to be the epoch when half of the final halo mass has been assembled into the whole merging tree. Interestingly, there is no clustering difference for halos with different last major merger time. If the observed dependence of galactic clustering strength on the color is true, then our result implies that the color of a central galaxy should not be correlated with the last major merger time of its host halo.

Recently, some authors (e.g., Wang et al., 2008) have successfully detected the difference in the clustering strength of galaxies categorized according to certain properties such as the color which they associate with group age. There also have been

other attempts to study the environmental dependence of galaxy properties in the SDSS or similar galaxy catalogues. However, directly relating the dark halo assembly history with the observational properties of galaxies can be difficult, because of two reasons. First, current galaxy formation model is still known to be affected by the poor modeling of cooling and feedbacks. Secondly, halo clustering shows different dependence on various definitions of halo formation time, which can be hard to interpret in terms of galaxy formation. Our results presented in Chapter 3 suggest that a halo age related to the formation history of its member galaxies, indicated by $z_{1/2,\mathrm{t}_1}$ and $z_{1/2,\mathrm{t}_2}$, may be the most appropriate for detecting the assembly effects on the halo bias parameter. Base on this proposition, Zapata et al. (2009) used the mean stellar-mass-weighted age of member galaxies in a given group as an indicator of the age of the group itself, and explore its possible connection with several other observational quantities. They found two suitable candidates that are most closely correlated with the group age: (1) the isolation of the group defined in terms of the distance to its nearest neighbour, and (2) the concentration, measured as the density calculated using the fifth closet bright galaxy to the group center. They further suggest that these two properties can be used to study the halo assembly effect on galaxy clustering properties.

The previous two works mainly focus on the assembly of the main progenitor (the main branch) of a dark halo. Besides the assembly of the main progenitor, the merger statistics of other progenitors (called sub-halos after the merger) is also important for galaxy evolution, since all galaxies were central galaxies at some high redshift in the scenario of hierarchical structure formation. Thus, the sub-halo accretion history is the basis of the galaxy merging history. Our studies of the mass function of sub-halos at accretion (often referred to as the USMF) suggest that the USMF follows a universal functional form, in the sense that it does not depend on the mass of the host halo or the redshift at which the host halo is identified. This conclusion applies

to the two cases we have studied: sub-halos accreted by the main progenitor of a host halo, and sub-halos that were accreted by all branches on the entire host halo merging history tree. It appears that the USMF is truly a generic property of dark matter halos. In addition, sub-branches of the merging tree accreted the majority of sub-halos with mass smaller than 1% of the final host halo mass. However, due to the tidal disruption, only less than 30% of the accreted halos were able to survive the post-accretion phase, and most of them were accreted by the main progenitors quite recently.

BIBLIOGRAPHY

Alam S. M. K., Bullock J. S., Weinberg D. H., 2002, ApJ, 572, 34

Angulo R. E., Baugh C. M., Lacey C. .G, 2008a, MNRAS, 387, 921

Angulo R. E., Lacey C. G., Baugh C. M., Frenk C. S., 2008b, preprint (astro-ph/0810.2177)

Audit E., Teyssier R., Alimi J.-M., 1997, A&A, 325, 439

Avila-Reese V., Firmani C., 2000, RevMexAA, 36, 23

Bardeen J. M., Bond J. R., Kaiser N., Szalay A. S., 1986, ApJ, 304, 15

Barnes J., Efstathiou G., 1987, ApJ, 319, 575

Barnes J., Hernquist L., 1996, ApJ, 471, 115

Berlind A. A., Kazin E., Blanton M. R., Pueblas S., Scoccimarro R., Hogg D. W., 2006, preprint (astro-ph/0610524)

Berlind A. A., Weinberg D. H., 2002, ApJ, 575, 587

Birnboim Y., Dekel A., 2003, MNRAS, 345, 349

Bertschinger E., Jain B., 1994, ApJ, 431, 486

Bond J.R., Cole S., Efstathiou G., Kaiser N., 1991, ApJ,379, 440

Bond J.R., Myers S., 1996a, ApJS, 103, 1

Bond J.R., Myers S., 1996b, ApJS, 103, 41

Borgani S., Coles P., Moscardini L., 1994, MNRAS, 271, 223

Bower R., 1991, MNRAS, 248, 332

Bryan G., Norman M., 1998, ApJ, 555, 240

Buchert T., Ehlers J., 1993, MNRAS, 264, 375

Bullock J. S., Dekel A., Kolatt T. S., Kravtsov A. V., Klypin A. A., Porciani C., Primack J. R., 2001a, ApJ, 555, 240

Bullock J.S., Kolatt T.S., Sigad Y., Somerville R.S., Kravtsov A.V., Klypin A.A., Primack J.R., Dekel A., 2001b, MNRAS, 321, 559

Carroll S. M., Press W. H., Turner E. L., 1992, ARA&A, 30, 499

Catelan P., 1995, MNRAS, 276, 115

Catelan P., Lucchin F., Matarrese S., Porciani C., 1998, MNRAS, 297, 692

Cattaneo A., Dekel A., Faber S. M., Guiderdoni B., 2008, MNRAS, 389, 567

Chen D. N., Jing Y. P., 2002, MNRAS, 336, 55

Chiueh T., Lee J., 2001, ApJ, 555, 83

Churazov E., Sazonov S., Sunyaev R., Forman W., Jones C., Böhringer, H., 2005, MNRAS, 363, 91

Cohn J.D., Bagla J.S., White M., 2001, MNRAS, 325, 1053

Cohn J.D., White M., 2005, preprint (astro-ph/0506213)

Cole S., Lacey C., 1996, MNRAS, 281, 716

Cole S., Lacey C.G., Baugh C.M., Frenk C.S., 2000, MNRAS, 319, 168

Conroy C., Wechsler R. H., Kravtsov A. V., 2006, ApJ, 647, 201

Cook M., Lapi A., Granato G. L., 2009, MNRAS, 397, 534

Croton D. J., Gao L., White S. D. M., 2007, MNRAS, 374, 1303

Croton D. J. et al., 2006, MNRAS, 365, 11

Dalal N., White M., Bond J. R., Shirokov A., 2008, ApJ, 867, 12

De Lucia G., Blaizot J., 2007, MNRAS, 375, 2

De Lucia G., Kauffmann G., Springel V., White, S. D. M., Lanzoni B., Stoehr F., Tormen G., Yoshida N., 2004, MNRAS, 348, 333

De Lucia G., Springel V., White, S. D. M., Croton D., Kauffmann G., 2006, MNRAS, 366, 499

Desjacques V., 2008, MNRAS, 388, 638

Diemand J., Kuhlen M., Madau P., 2007, ApJ, 667, 859

Eisenstein D.J., Loeb A., 1996, ApJ, 459, 432

Eke V.R., Navarro J.F., Steinmetz M., 2001, ApJ, 554, 114

Fakhouri O., Ma C. P., 2008, MNRAS, 386, 577

Firmani C., Avila-Reese V., 2000, MNRAS, 315, 457

Gao L., Loeb A., Peebles P. J. E., White S. D. M., Jenkins A., 2004b, ApJ, 614, 17

Gao L., Springel V., White S. D. M., 2005, MNRAS, 363, 66

Gao L., White S. D. M., 2007, MNRAS, 377, 5

Gao L., White S. D. M., Jenkins A., Stoehr F., Springel V., 2004a, MNRAS, 355, 819

Georgakakis A. et al., 2008, MNRAS, 385, 2049

Ghigna S., Moore B., Governato F., Lake G., Quinn T., Stadel J., 2000, ApJ, 544, 616

Giocoli C., Torman G., van den Bosch F. C., 2008a, MNRAS, 386, 2135

Giocoli C., Pieri L., Tormen G., MNRAS, 2008b, 387, 689

Governato F., Babul A., Quinn T., Tozzi P., Baugh C.M., Katz N., Lake G., 1999, MNRAS, 307, 949

Gross M.A.K., Somerville R.S., Primack J.R., Holtzman J., Klypin A.A., 1998, MNRAS, 301, 81

Harker G., Cole S., Helly J., Frenk C., Jenkins A., 2006, MNRAS, 367, 1039

Hahn O., Porciani C., Carollo C. M., Dekel A., 2007, MNRAS, 375, 489

Hernquist L., 1989, Nat., 340, 687

Hopkins P. F., Hernquist L., Cox T. J., Di Matteo T., Robertson B., Springel V., 2006, ApJS, 163, 1

Jain B., Bertschinger E., 1994, ApJ, 431, 495

Jenkins A., Frenk C.S., White S.D.M., Colberg J.M., Cole S., Evrard A.E., Couchman H.M.P., Yoshida N., 2001, MNRAS, 321, 372

Jing Y. P., 1998, MNRAS, 503, 9

Jing Y. P., 2002a, ApJ, 535, 30

Jing Y. P., Suto Y., 2000, ApJ, 529, 69

Jing Y. P., Suto Y., 2002, ApJ, 574, 538

Jing Y. P., Suto Y., Mo H. J., 2007, ApJ, 657, 664

Kang X., Jing Y. P., Silk J., 2006, ApJ, 648, 820

Kauffmann G., White S.D.M., 1993, MNRAS, 261, 921

Kauffmann G., White S.D.M., Guiderdoni B., 1993, MNRAS, 264, 201

Keres D., Katz N., Weinberg D.H., Dave R., 2005, MNRAS, 363, 2

Keselman J. A., Nusser A., 2007, MNRAS, 382, 1853

Kim J., Park C., Choi Y., 2008, ApJ, 683, 123

Lacey C., Cole S., 1993, MNRAS, 262, 627

Lanzoni B., Mamon G.A., Guiderdoni B., 2000, MNRAS, 312, 781

Lee J., Shandarin S., 1998, ApJ, 500, 14

Lemson G., Kauffmann G., 1999, MNRAS, 302, 111

Lemson G. & the Virgo Consortium, 2006, preprint (astro-ph/0608019)

Li Y., Mo H. J., van den Bosch F. C., Lin W. P., 2007, MNRAS, 379, 689

Li Y., Mo H. J., Gao L., 2008, MNRAS, 389, 1419

Li Y., Mo H. J., 2009, preprint, (astro-ph/0908.0301)

Lin L., Chiueh T., Lee J., 2002, ApJ, 574, 527

Lin W.P., Jing Y.P., Lin L., 2003, MNRAS, 344, 1327

Lu Y., Mo H.J., Katz N., Weinberg M.D., 2006, MNRAS, 368, 1931

Maller A. H., Katz N., Keres D., Dave R., Weinberg D. H., 2006, ApJ, 647, 763

Mandelbaum R., Tasitsiomi A., Seljak U., Kravtsov A. V., Wechsler R. H., 2005, MNRAS, 362, 1451

Mandelbaum R., Seljak U., Kauffmann G., Hirata C. M., Brinkmann J., 2006, MNRAS, 368, 715

McIntosh D. H., Guo Y., Hertzberg J., Katz N., Mo H. J., van den Bosch F. C., Yang X., 2008, MNRAS, 388, 1537

Mihos J. C., Hernquist L., 1996, ApJ, 464, 641

Mo H. J., Jing, Y. P., White, S. D. M., 1996, MNRAS, 282, 1096

Mo H. J., Mao S. D., 2000, MNRAS, 318, 163

Mo H. J., White S. D. M., 1996, MNRAS, 282, 347

Mo H. J., White S. D. M., 2002, MNRAS, 336, 112

Monaco P., 1995, ApJ, 447, 23

Monaco P., 1998, Fundamentals of Cosmic Physics, Vol. 19, 157

Monaco P., Theuns T., Taffoni G., Governato F., Quinn T., Stadel J., 2002a, ApJ, 564, 8

Monaco P., Theuns T., Taffoni G., 2002b, MNRAS, 331, 587

Moore B., Ghigna S., Governato F., Lake G., Quinn T., Stadel J., Tozzi P., 1999a, ApJ, 524, 19

Moore B., Quinn T., Governato F., Stadel J., Lake G., 1999b, MNRAS, 310, 1147

Naab T., Burkert A., 2003, ApJ, 597, 893

Navarro J. F., Frenk C. S., White S. D. M., 1997, ApJ, 462, 563

Navarro J. F., Frenk C. S., White S. D. M., 1997, ApJ, 490, 493

Neistein E., van den Bosch F. C., Dekel A., 2006, MNRAS, 372, 933

Nelan J. E. et al., 2005, ApJ, 632, 137

Nusser A., Sheth R.K., 1999, MNRAS, 303, 685

Peacock J.A., Heavens A.F., 1990, MNRAS, 243, 133

Peebles P. J. E., 1980, The Large-scale Strucutre of the Universe, Princeton U. Press, Princeton, NJ

Percival W. J., Scott D., Peacock J. A., Dunlop J. S., 2003, ApJ, 338, 31

Perlmutter S. et al., 1999, ApJ, 517, 565

Press W., Schechter P., 1974, ApJ, 187, 425

Rodrigues D.D.C., Thomas P.A., 1996, MNRAS, 282, 631

Sandvik H. B., Moller O., Lee J., White S. D. M., 2007, MNRAS, 377 234

Shaw L. D., Weller J., Ostriker J. P., Bode P., 2–7, ApJ, 659, 1082

Sheth R. K., 1998, MNRAS, 300, 1057

Sheth R. K., Lemson G., 1999, MNRAS, 305, 946

Sheth R. K., Mo H.J., Tormen G., 2001, MNRAS, 323, 1 (SMT01)

Sheth R. K., Tormen G., 1999, MNRAS, 308, 119

Sheth R. K., Tormen G., 2002, MNRAS, 329, 61

Sheth R. K., 2003, MNRAS, 345, 1200

Sheth R. K., Tormen G., 2004, MNRAS, 350, 1385

Somerville R.S., Kolatt T.S., 1999, MNRAS, 305, 1

Somerville R.S., Primack J.R., 1999, MNRAS, 310, 1087

Somerville R.S., Lemson G., Kolatt T.S., Dekel A., 2000, MNRAS, 316, 479

Spergel et al., 2007, ApJS, 170, 337

Springel V. et al., 2005a, Nat., 435, 639

Springel V., Di Matteo T., Hernquist L., 2005b, MNRAS, 361, 776

Springel V., White S. D. M., Tormen G., Kauffmann G., 2001, MNRAS, 328, 726

Stewart K. R., Bullock J. S., Wechsler R. H., Maller A. H., Zentner A. R., 2008, ApJ, 683, 597

Syer D., White S. D. M., 1998, MNRAS, 193, 337

Taffoni G., Monaco P., Theuns T., 2002, MNRAS, 333, 623

Thomas D., Maraston C., Bender R., Mendes de Oliveira C., 2005, ApJ, 621, 637

Tinker J. L., Conroy C., Norberg P., Patiri S. G., Weinberg D. H., Warren M. .S, 2008, ApJ, 686, 53

Tinker J. L., Weinberg D. H., Zheng Z., Zehavi I., ApJ, 2005, 631, 41

Tormen G., 1998, MNRAS, 297, 648

van den Bosch F. C., 2001, MNRAS, 327, 1334

van den Bosch F. C, 2002a, MNRAS, 331, 98

van den Bosch F. C, 2002b, MNRAS, 332, 456

van den Bosch F. C., Yang X., Mo H. J., 2003a, MNRAS, 340, 771

van den Bosch F. C., Mo H. J., Yang X., 2003b, MNRAS, 345, 923

van den Bosch F. C., Tormen G., Ciocoli C., 2005, MNRAS, 359, 1029

van den Bosch et al., 2007, MNRAS, 376, 841

Wang H. Y., Mo H. J., Jing Y. P., MNRAS, 375, 633

Wang L., Li C., Kauffmann G., De Lucia G., 2006, MNRAS, 371, 537

Wang Y., Yang X., Mo H. J., van den Bosch F. C., Weinmann S. M., Chu Y., 2008, ApJ, 687, 919

Warren M. S., Abazajian K., Holz D. E., Teodoro L., 2006, ApJ, 646, 881

Wechsler R. H., Zentner A. R., Bullock J. S., Kravtsov A. V., Allgood B., 2006, ApJ, 652, 71

Wechsler R. H., Bullock J. S., Primack J. R., Kravtsov A. V., Dekel A., 2002, ApJ, 568, 52 (W02)

Wetzel A. R., Cohn J. D., White M., Holz D. E., Warren M. S., 2007, ApJ, 656, 139

Wetzel A. .R., Cohn J. D., White M., 2008, preprint (astro-ph/0810.2537)

White S. D. M., Rees M. J., 1978, MNRAS, 183, 341

Yang X., Mo H. J., van den Bosch F. C., 2003, MNRAS, 339, 1057

Yang X., Mo H. J., van den Bosch F. C., 2006, ApJL, 658, 55

Yang X. H., Mo H. J., van den Bosch F. C., 2009, ApJ, 693, 830

Zapata T., Perez J., Padilla N., Tissera o., 2009, MNRAS, 394, 2229

Zel'Dovich Y. B., 1970, A&A, 5, 84

Zentner A. R., Bullock J. S., 2002, Phys. Rev. D., 66, 043003

Zentner A. R., Bullock J. S., 2003, ApJ, 598, 49

Zentner A. R., Berlind A., Bullock J. S., Kravstov A., Wechsler R. H., 2005, ApJ, 624, 505

Zhao D.H., Mo H.J., Jing Y.P., Börner G., 2003a, MNRAS, 339, 12

Zhao D.H., Jing Y.P., Mo H.J., Börner G., 2003b, ApJ, 597, 9

Zheng Z. et al., 2005, ApJ, 633, 791

Zhu G., Zheng Z., Lin W. P., Jing Y. P., Kang X., Gao L., 2006, ApJL, 639, 5